Building Patient-Specific Models of the Heart to Study Cardiac Growth and Remodeling

by

Yiling Fan

B.Eng, National University of Ireland, Galway (2017)
S.M., Massachusetts Institute of Technology (2019)

Submitted to the Department of Mechanical Engineering
in partial fulfillment of the requirements for the degree of

DOCTOR OF PHILOSOPHY IN MECHANICAL ENGINEERING

at the

MASSACHUSETTS INSTITUTE OF TECHNOLOGY

September 2023

Authored by:	Yiling Fan Department of Mechanical Engineering August 31st, 2023
Certified by:	Ellen T. Roche, PhD Associate Professor of Mechanical Engineering and Institute for Medical Engineering & Science, Thesis Supervisor
Accepted by:	Nicolas Hadjiconstantinou, PhD Professor of Mechanical Engineering Chairman, Department Committee on Graduate Theses

Building Patient-Specific Models of the Heart to Study Cardiac Growth and Remodeling

by

Yiling Fan

Submitted to the Department of Mechanical Engineering
on August 31st, 2023 in partial fulfillment of the requirements for the degree of

DOCTOR OF PHILOSOPHY IN MECHANICAL ENGINEERING

ABSTRACT

Cardiac growth and remodeling (G&R) are intricate processes that occur in response to various physiological and pathological conditions to maintain the optimal function of the heart. These processes involve complex molecular, cellular, and structural alterations that influence the size, shape, and function of the heart. Research efforts, utilizing *in vitro* and *in vivo* models, have shed light on the mechanisms of G&R at the cellular and tissue levels. Clinically, we have access to a wealth of sophisticated information, ranging from 0D (e.g. pressure, heart rate, and ECG) to 4D (e.g. dynamic MRI and CT) data about our cardiovascular system. However, a significant challenge lies in the interpretation of these data, as they provide macroscale information and how this links to microscale mechanisms remains poorly understood. In consequence, a vast amount of clinical data, particularly imaging data, are employed qualitatively rather than quantitatively. Furthermore, many microstructural discoveries have not yet been fully leveraged for the improvement of diagnostic accuracy and therapeutic strategies.

The main goal of this thesis is to develop multiscale patient-specific simulations to connect microscale insights and clinically accessible macroscale information. I propose a growth characterization workflow utilizing *in vivo* cardiac MRI, kinematic growth modeling, and inverse finite element method to quantify tissue level growth. Tested on *in vivo* data of swine models, this approach showcases the potential of non-invasive measurement of microstructural growth properties. It also highlights two potential areas of improvements: a more granular growth analysis currently hindered by the simplified kinematic growth model and a more efficient process of the inverse analysis, catering to the time-sensitive nature of clinical practice. To address this, I create a multiscale model using a microstructurally motivated growth theory . The model enables investigation of changes in different tissue components (e.g. myocytes and collagen) during the process of G&R and its subsequent reversal. In addition, I develop a data-driven surrogate model that can efficiently generate dynamic patient-specific simulations of the left ventricle with mean nodal error below 3 mm. The surrogate model achieves a speed increase of 4 orders of magnitude compared to the traditional finite element model, making it ideal for inverse studies in fast-paced clinical settings.

In summary, this thesis introduces simulation frameworks that effectively quantify G&R properties, bridge the mechanobiological insights of G&R across different scales, and facilitate the generation of personalized models. These advancements represent progress towards the realization of cardiac digital twins in the realm of clinical practice.

Thesis supervisor: Ellen T. Roche, PhD
Title: Associate Professor of Mechanical Engineering and Institute for Medical Engineering & Science

Acknowledgments

I am profoundly grateful to everyone who has provided help and guidance during my PhD journey. First and foremost, I wish to express my deepest appreciation to my thesis advisor, Professor Ellen Roche, who has given me numerous support and is always trying to encourage me while I find my path in field of science and engineering. Her discerning insights into research directions have been truly inspiring, and her readiness to assist others has shaped my perspective on the essence of a researcher. I would like to extend my sincere thanks to my thesis committee members, Professor Christopher Nguyen and Professor Rohan Abeyaratne. Professor Nguyen, a remarkable collaborator, mentor, and friend, has consistently welcomed me into his lab, offering instrumental support that facilitated the research throughout my PhD. With Professor Abeyaratne, I engaged in his insightful Elasticity class and our thought-provoking committee discussions, all of which facilitated a deeper understanding of mechanics and significantly enhanced the quality of my thesis.

This work would not have been possible without additional help. I express my thanks to my collaborator Dr. Jaume Coll-Font for his significant contribution and enlightening discussions on the growth characterization project, my mentee Mr. Igor Heinze for his tremendous efforts in implementing the homogenized constrained mixture model. I also want to thank all my colleagues from the Therapeutic Technology Design & Development (TTDD) lab at MIT and the Nguyen lab at Mass General Hospital. Special thanks to Dr. Caglar Ozturk, who I partnered with to tackle many simulation projects in the lab. I am grateful to my office mates, Dr. Markus Horvath, Dr. Claudia Varela, and Dr. Lucy Hu, who welcomed me to the lab from the first day I joined and made my daily lab encounters enjoyable; to Dr. Keegan Mendez and Dr. Connor Verheyen who rendered much-needed moral support during my thesis writing period. I feel fortunate to have worked alongside such a friendly and supportive group of people.

Lastly, but most importantly, I want to thank my parents in China. Without their constant love and support, especially during the challenging pandemic time, I would not have been able to accomplish all this work. They have been a pillar of strength for me throughout this journey, and I am eternally grateful to them.

Contents

List of Figures

List of Tables

Chapter 1

Introduction

1.1 Motivation

Cardiac growth and remodeling (G&R) refers to the changes that occur in the size, shape, structure, and functionality of the heart in response to various physiological or pathological stimuli. Physiological cardiac growth happens during normal development or in response to regular exercise, leading to a healthy, stronger heart. Pathological remodeling, on the other hand, typically arises in response to chronic diseases such as hypertension, myocardial infarction (heart attack), or heart failure. This can result in alterations in the structure of the heart, such as hypertrophy (increased muscle mass), fibrosis (excess fibrous connective tissue), and chamber dilation, all of which can diminish cardiac function and lead to further cardiovascular complications. The molecular mechanisms underpinning these changes involve complex interactions between cardiomyocytes, fibroblasts, endothelial cells, and various signaling molecules. Understanding these processes can guide the development of therapeutic strategies for progressive heart failure and other chronic heart diseases.

The research on cardiac G&R can be broadly categorized into experimental and computational studies. Experimental studies often rely on *in vivo* models [1, 112, 123, 124], which are animal models designed to replicate the pathophysiology of cardiac diseases. While these models provide valuable insights into the progression of cardiac G&R at various scales, they come with two important limitations. Firstly, the cross-species difference limits animal models in representing human pathophysiology accurately. Secondly, the development and maintenance of these models are costly and time-consuming. More recently, *in vitro* models have emerged as a viable alternative for studying cardiac G&R with relatively lower cost and more precise control of the G&R stimuli [88]. However, these models typically have shorter lifespan, ranging from days to a few weeks, which restricts the investigation of the long-term effects. In addition, they are limited to the cellular and tissue levels and do not always resemble the complexity of the whole organism. Computational studies, on the other hand, can emulate experimental observations across different scales with significantly lower cost and shorter timelines. This offers the potential to enhance our understanding of the complex G&R mechanisms. However, due to computational complexity and lack of patient-specific data, many of the *in silico* studies (conducted via computer modeling) were conducted under generalized and somewhat simplistic models. Moreover, these models usually focus on a specific scale, either at the cellular level or at the organ level without making the connection between them. This motivates the development of computational frameworks that can integrate with experimental approaches to generate multiscale patient-specific simulations. These frameworks can be used to explore the complex mechanobiological theories of G&R which are continuously evolving and remain controversial. In addition, the simulations can quantify patient-specific properties that are difficult, if not impossible, to measure experimentally. Recognizing these unique properties might bolster both diagnosis processes and the formulation of personalized therapeutic strategies. This thesis presents a proof-of-concept example of one such framework, delving into advancements in multiscale G&R modeling and efficient patient-specific simulations, all of which can be further integrated into the framework.

1.2 Cardiac growth and remodeling

Cardiac growth can be categorized into two types at the macroscopic level: eccentric growth – where the ventricular volume increases, and concentric growth – where the ventricular wall thickness increases, as shown in Figure 1.1. At the microscopic level, growth is the result of increased size of cardiomyocytes. Similar to macroscopic observations, *in vitro* studies have shown that cardiomyocytes have two growth phenotypes: longitudinal and transverse sarcomerogenesis [138]. Moreover, it has been hypothesized that longitudinal and transverse growth at the microscopic level, result in eccentric and concentric growth at the macroscopic level, respectively [47]. These distinctions in growth types are important since different types of exercise induce different types of macroscopic growth – anaerobic exercise, where the left ventricular (LV) pressure increases significantly within a short time frame, is typically associated with concentric growth, while aerobic exercise, where LV volume increases gradually to stably achieve higher cardiac output to match the increases of oxygen consumption, leads to eccentric growth [36, 81]. Interestingly, similar hypertrophic phenotypes also appear in pathological conditions. The volume overload condition is usually caused by myocyte loss due to ischemia, myocarditis, or mitral regurgitation, leading to heart failure with reduced ejection fraction (HFrEF), or systolic heart failure. On the other hand, the pressure overload condition is usually related to aortic stenosis and other chronic comorbidities such as hypertension, diabetes, and obesity, resulting in heart failure with preserved ejection fraction (HFpEF), or diastolic heart failure. The etiology of the discrepancy between physiologic and pathologic growth remains to be elucidated, apart from histological studies showing that the latter is also accompanied by microstructural remodeling (e.g. interstitial fibrosis, non-uniform cardiomyocyte alignment, and excessive collagen deposition) [127].

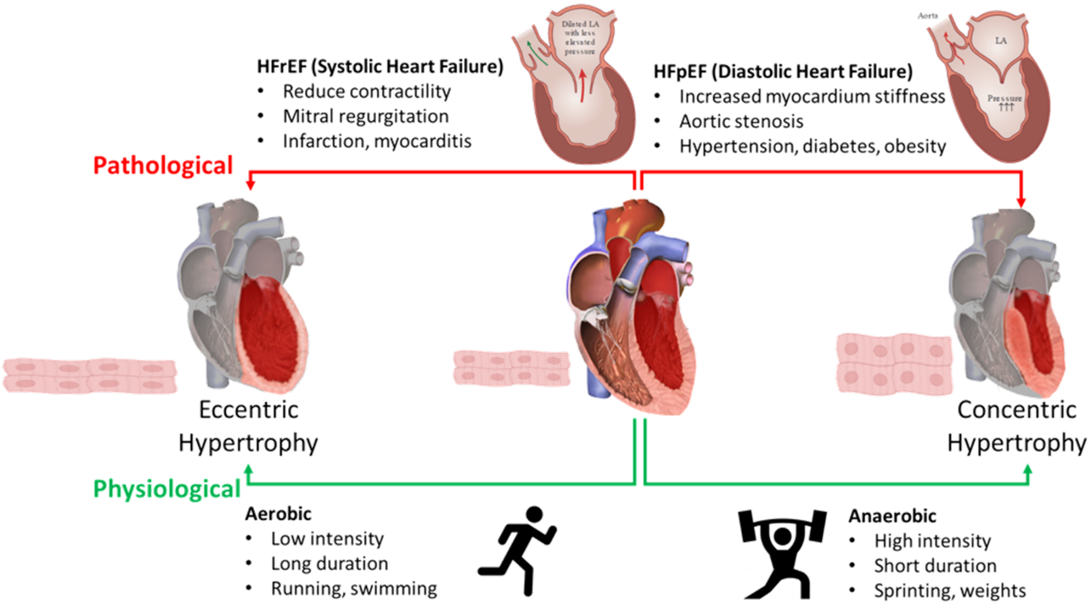

Figure 1.1: An overview of cardiac growth and remodeling.

1.3 Experimental characterization of growth and remodeling

There is a long history of studying myocardial growth experimentally, both *in vitro* and *in vivo* [1, 88]. *In vitro* studies apply static loads on isolated cardiomyocytes in both longitudinal [74] and transverse directions [138] to mimic the conditions of volume overload and pressure overload, respectively. These studies have observed sarcomerogenesis in series or in parallel, and corroborates the current understanding of longitudinal or transverse growth in response to pathological loading. *In vivo* studies on cardiac growth rely on small and large animal models simulating pathological growth resulting from volume or pressure overload [1]. Volume overload models, associated with eccentric hypertrophy, have been generated by either cutting the chordae tendineae to induce mitral regurgitation [72, 112], or by implanting a pacemaker to repeatedly introduce premature ventricular contraction (PVC) [123]. Pressure overload models, typically associated with concentric hypertrophy, have been created by aortic banding [124, 90], dietary modifications [90, 56], or genetic modifications [70, 134].

On the other hand, exercised-induced hypertrophic models have also been established in both small and large animals using swim training, wheel running or treadmill running [130]. Most of these *in vivo* studies evaluate the effects of growth on cardiac function (e.g. ejection fraction, cardiac output, hemodynamics) as well as morphological changes of the LV (e.g relative wall thickness). A few studies have used histology, acquired either *ex vivo* at the end of the study or through invasive biopsy, to quantify the level of cardiomyocyte growth [72, 112, 90] or the changes in collagen fiber orientation [124]. However, due to limitations associated with *ex vivo* analysis and the added complexity and risks of *in vivo* biopsies, there is a profound paucity of data on the microstructural changes of the myocardium during LV growth and remodeling. Thus, the mechanistic link between growth at the organ and tissue-cellular levels remains poorly understood.

1.4 Computational modeling of cardiac growth and remodeling

Computational models that aim to develop quantitative links between growth observations at the organ level and tissue-cellular level are promising tools to give better insights into growth mechanisms [88]. Currently, there are two main frameworks to model cardiac G&R: kinematic growth and constrained mixture growth. The concepts of these two theories are summarized in Figure 1.2.

The kinematic growth model is a phenomenon-based model that introduces inelastic volumetric deformation to represent the change in myocardium volume. The total deformation gradient at time s ($\mathbf{F}(s)$) can be multiplicatively decomposed into an elastic tensor ($\mathbf{F}_e(s)$) and a growth tensor ($\mathbf{F}_g(s)$), such that $\mathbf{F}(s) = \mathbf{F}_e(s)\mathbf{F}_g(s)$. The growth tensor can be set explicitly for longitudinal growth $\mathbf{F}_g = \mathbf{I} + (\vartheta_g - 1)\mathbf{f} \otimes \mathbf{f}$, or for transverse growth $\mathbf{F}_g = \vartheta_g\mathbf{I} + (1 - \vartheta_g)\mathbf{f} \otimes \mathbf{f}$, where $\mathbf{f}$ is the unit direction of the sarcomere and ϑ_g is a parameter representing the level of growth. ϑ_g can be defined as a function of various growth stimuli (e.g. stress and strain). Due to its simplicity, kinematic growth theory has been widely applied in modeling cardiac G&R [88]. For example, Gsöktepe et al. [47] used an idealized bi-ventricular model to simulate both concentric and eccentric hypertrophy. The model was later extended with a stress-driven law to simulate ventricular growth under conditions of systemic and pulmonary hypertension [105]. A strain-driven law was used with a four-chamber human heart model and also demonstrated the capability to simulate both concentric and eccentric hypertrophy [44].

The constrained mixture growth is a microstructure-based model where the tissue (e.g. myocardium) is considered as a mixture of various constituents. Each constituent continuously degrades from and reproduces into the existing tissue. The "constrained" in the name refers to the hypothesis that each individual mass of constituent i added at time τ is subject to a certain pre-stretch $\mathbf{F}^i_{pre}(\tau)$, in order to maintain the structure of the whole organism under external constraints (i.e. forces). The elastic deformation gradient of constituent i from time τ to s can be calculated as $\mathbf{F}^{i(\tau)}_e(s) = \mathbf{F}(s)\mathbf{F}^{-1}(\tau)\mathbf{F}^i_{pre}(\tau)$. The imbalance between degradation and deposition rates in multiple constituents causes volumetric change of the body (growth), while the stress difference between the newly added mass (due to pre-stretch) and the degraded mass results in isochoric deformation of the body (remodeling). The classical constrained mixture growth model, which requires tracking the reference configuration of each individual mass added at different time points, is difficult to implement and computationally expensive. Thereby, the theory has not been used extensively for myocardial growth modeling, but instead has primarily been used in the context of vascular growth, involving simplified geometries (e.g. 2D axisymmetric) with isotropic properties [88]. To overcome this, a homogenized constrained mixture model has been proposed [26] and was recently implemented to investigate the mechanobiological stability in the left ventricle G&R [42]. Another recent study introduced an updated reference configuration approach to simplify the mass tracking process in the classical constrained mixture model [48]. This model was used to simulate different phenotypes of growth in the LV. In this thesis, I will implement the homogenized constrained mixture model to study cardiac G&R and its reversal, with further details to be provided in Chapter 3.

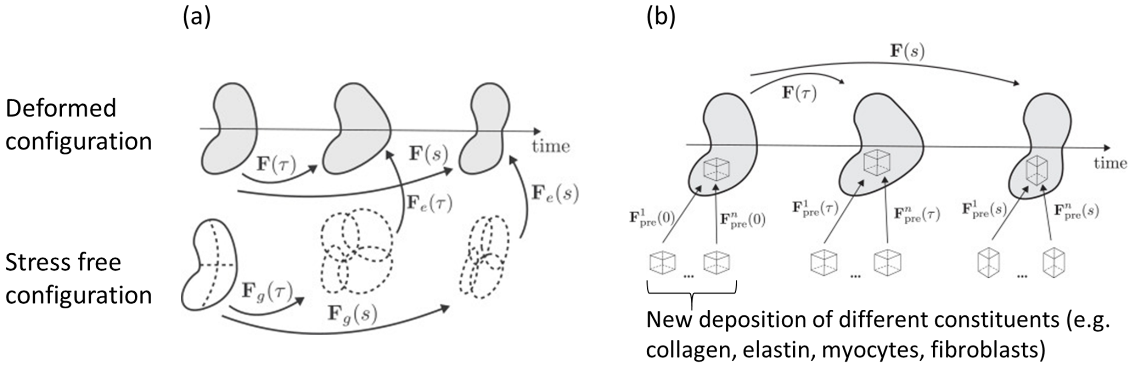

Figure 1.2: Schematic diagram of (a) kinematic growth theory and (b) constrained mixture growth theory where a body is deformed due to growth and external loads from time τ to s. (a) $\mathbf{F}(s)$ can be decomposed into an elastic component $\mathbf{F}_e(s)$ and a growth component $\mathbf{F}_g(s)$. (b) In constrained mixture growth, the growth part is constructed by modeling new components of different constituents continuously being deposited into the current body with a determined pre-stretch $\mathbf{F}^i_{pre}(s)$. (Figure adapted from Niestrawska et al. [88])

1.5 Patient-specific simulations

The concept of digital twins has a long history in many industries, and it is emerging as a promising field in healthcare. The idea encompasses many levels, ranging from 0D to 3D multiphysics simulations, but here, we will focus on 3D physics simulations. Patient-specific simulation involves creating *in silico* models based on the unique anatomical, physiological, or genetic data of a given patient. This approach serves as a cornerstone in personalized medicine, facilitating accurate diagnosis, virtual treatment planning, and precise surgical execution, while also advancing medical education and driving the design and testing of medical devices. As shown in Figure 1.3, the typical workflow to generate patient-specific simulations involves several crucial steps. First, patient-specific information (e.g. anatomy, physiological boundary conditions) is acquired from non-invasive medical imaging (e.g. MRI, CT, and ultrasound) and/or invasive measurement (e.g. angiography and catheterization). This data is then input to a physics simulator (e.g. finite element analysis - FEA, computational fluid dynamics - CFD, or fluid structure interaction FSI) to provide different types of outputs, such as pressure, volume, and flow, that can be compared with clinical measurements. However, the physics simulator often requires more inputs than those available clinically. Therefore, to validate the simulation, an inverse method is needed to tune these uncertain inputs such that its outputs match the clinical measurements. The resultant validated patient-specific model, often referred to as the 'digital twin' of the corresponding medical application, provides a precise and personalized means for extracting clinically useful information.

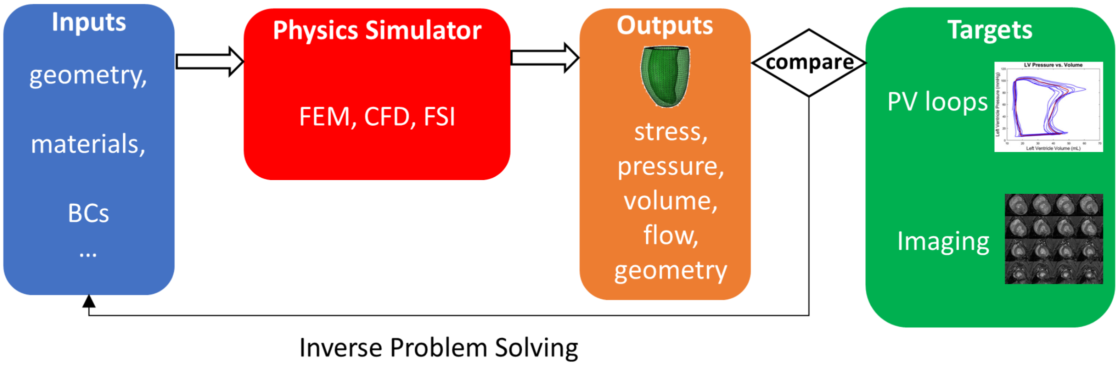

Figure 1.3: The workflow for building patient-specific simulations.

Due to the generality of this process, patient-specific simulations have been built for many systems in the human body. For example, patient-specific lung simulations were developed to track lung tumor motion non-invasively [69]. For surgical planning, Jordal et al. [65] used CFD to build upper airways simulations to assess the effect nasal surgery on patients with obstructive sleep apnea syndrome. In liver surgeries, preoperative 3D simulation is commonly used to improve the efficiency of the surgical procedure [85]. In the field of medical device design, patient-specific head simulations have been used to test a novel insertion device for the external ventricular drain (EVD) procedure [125].

Patient-specific simulations are used even more often in the cardiac and cardiovascular system. Due to the sophisticated nature of the cardiovascular system, there are three main types of simulations: electrical (electrophysiology), fluid (hemodynamics), and structural (anatomy) simulations. Personalized electrophysiology models have been mainly used to simulate ventricular and atrial arrhythmias in order to customize the associated interventional treatments, such as ablation and cardiac resynochronization therapy (CRT). A thorough summary of these models can be found in a previous review [87]. In more recent studies [102, 13], these models were further tested under actual clinical settings to demonstrate the feasibility of changing the paradigm of ablation procedures. Fluid simulations, on the other hand, target the cardiovascular system. Patient-specific CFD models can provide detailed hemodynamic information which is critical in studying vascular diseases (such as atherosclerosis [63], aneurysms [103] and aortic dissection [22, 23]), planning vascular interventions (such as coronary revascularization [54], the Fontan operation [39, 76, 114], and treatments for aortic coarctation [68]), and optimizing cardiovascular devices (such as stents [68, 122], aortic aneurysm endografts [115], and mechanical circulatory support devices [46, 79, 92]). Structural simulations are presented in both the cardiac and cardiovascular systems. Structural simulations of heart can be divided into two categories, static and dynamic models. Static models are usually used to estimate the elastic properties of the myocardium [93, 133, 131] and further investigate the stress and strain distributions in the heart at a specific stage of the cardiac cycle (e.g. end-diastole and end-systole). These properties are challenging or impossible to measure *in vivo*. The static models can be further extended to dynamic models, which aim to recreate the dynamic motions of the heart throughout the cardiac cycle [38, 27]. They can also be coupled with fluid and/or electrophysiology simulations to provide holistic insight into the intricate physiology of the heart [113, 129]. In cardiovascular mechanics, structural models are often used to study the stress distribution in large vessels (e.g. aorta, pulmonary artery). Excessive wall stress is believed to cause remodeling of the vessels, leading to aneurysms and dissections. Therefore, static models [128, 37] that simulate the systolic stage with peak pressure have been generally deemed sufficient for providing clinically relevant information. Nevertheless, a few studies have also ventured into using fluid-structure interaction (FSI) models [71, 8].

1.6 Thesis organization

The objective of this thesis is to create advanced computational frameworks with state-of-the-art simulation techniques, such as multiscale modeling and data-driven modeling, to advance the research in cardiac growth and remodeling.

1.6.1 Specific Aims

There are three specific aims presented in this thesis:

1. To develop a computational framework that can quantify myocardium growth properties from *in vivo* imaging via patient-specific simulations.
2. To advance the G&R simulations in order to explore the complex mechanobiology of cardiac G&R, with a potential to provide clinically useful information.
3. To improve the efficiency of patient-specific simulations through the application of data-driven modeling.

In this thesis, Chapter 2 will focus on Aim 1, demonstrating a workflow that combines *in vivo* cardiac MRI, patient-specific modeling, and optimization to noninvasively quantify growth properties of the myocardium. Chapter 3 will address Aim 2 by using a microstructurally-driven modeling framework to create multiscale simulations and assess different mechanobiological hypotheses related to cardiac G&R. Lastly, Aim 3 will be addressed in Chapter 4 where a data-driven surrogate model of the LV dynamic simulation is introduced. This model demonstrates the potential to expedite the generation of patient-specific simulations using machine learning techniques. As illustrated in Figure 1.4, Aims 2 and 3 enhance two different elements in the growth characterization workflow presented in Chapter 2. Future work, which will be discussed in Chapter 5, envisions that by combining multiscale methods, data-driven modeling, together with *in vivo* imaging, we can create an *in silico* platform to efficiently generate digital twins of the heart. Such a platform will enable exploration of the complex interplay of various G&R stimuli, potentially yielding clinically relevant insights and improving the diagnosis and treatments of chronic heart diseases.

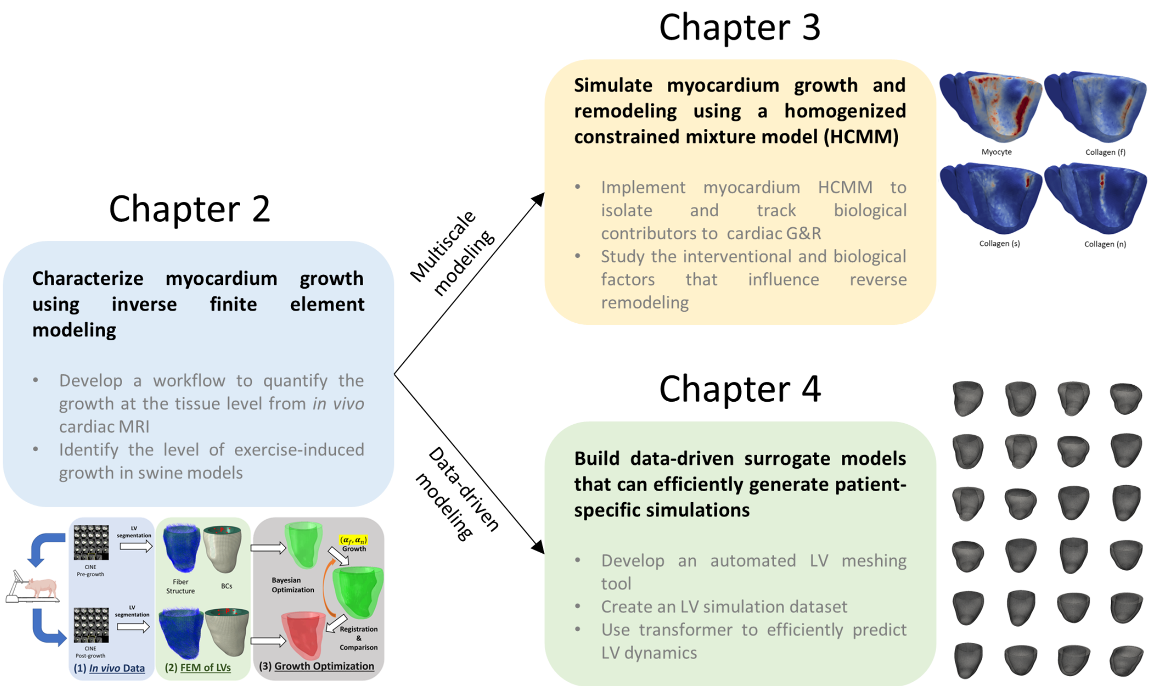

Figure 1.4: An overview of the thesis projects.

Chapter 2

Development of growth characterization workflow

2.1 Introduction

Exercise is known to lead to long-term physiological changes in the cardiovascular system such as an increase in contractility and a decrease in vascular resistance, heart rate and blood pressure as a result of parasympathetic mediation [36]. In addition, it induces morphological changes to the heart, which are typically referred to as cardiac growth or hypertrophy. Cardiac growth can be categorized into two types at the macroscopic level: eccentric growth – where the ventricular volume increases, and concentric growth – where the ventricular wall thickness increases. At the microscopic level, growth is the result of increasing size of cardiomyocytes and, similarly to the macroscopic observations, *in vitro* studies have shown that cardiomyocytes have two growth phenotypes: longitudinal and transverse sarcomerogenesis [138]. Moreover, it has been hypothesized that longitudinal and transverse growth at the microscopic level, result in eccentric and concentric growth at the macroscopic level [47]. These distinctions in growth types are important since different types of exercise produce different types of macroscopic growth – anaerobic exercise is typically associated with concentric growth, while aerobic exercise leads to eccentric growth [36, 81] — and, more importantly, growth can also be triggered by pathologic causes such as pressure-overload, with similar hypertrophic phenotypes, but leading to heart failure instead of improved cardiac function. The root cause of the discrepancy between physiologic and pathologic growth remains unclear except for histology studies showing that the latter is also accompanied by microstructure remodeling (e.g. interstitial fibrosis, non-uniform cardiomyocyte alignment, and excessive collagen deposition) [127].

There is a long history of studying myocardial growth experimentally, both *in vitro* and *in vivo* [1, 88]. *In vitro* studies apply static loads on isolated cardiomyocytes in the longitudinal [74] or transverse direction [138] to mimic the conditions of volume overload or pressure overload, respectively. These studies showed sarcomerogenesis in series or in parallel corroborates the current understanding of longitudinal or transverse growth in response to these pathological loading. *in vivo* studies on cardiac growth rely on small and large animal models of pathological growth resulting from volume overload or pressure overload [1]. Volume overload models, associated with eccentric hypertrophy, have been generated by either cutting the chordae tendineae to induce mitral regurgitation [72, 112] or by implanting a pacemaker to repeatedly introduce premature ventricular contraction (PVC) [123]. Pressure overload models, which are usually linked to concentric hypertrophy, have been created by aortic banding [124, 90], diet modification [90, 56], or genetic modification [70, 134]. On the other hand, exercise-induced hypertrophic models have also been created in both small and large animals by swim training, wheel running or treadmill running [130]. Most of these *in vivo* studies evaluate the effects of growth on the cardiac function (e.g. ejection fraction, cardiac output, hemodynamics) as well as morphological changes of the LV (e.g relative wall thickness). A few studies have used histology, acquired either *ex vivo* at the end of the study or through invasive biopsy, to quantify the level of cardiomyocyte growth [72, 112, 90] or the changes in collagen fiber orientation [124]. Due to the limitations associated with *ex vivo* analysis and the added complexity and risks of *in vivo* biopsies, there is a profound paucity of data on the microstructural changes of the myocardium during LV growth and remodeling. Thus, the mechanistic link of growth between the organ level and tissue-cellular level remains poorly understood.

Computational models that try to develop quantitative links between growth observations at the organ level and tissue-cellular level are promising tools to give better insights into growth mechanisms [88]. Currently, there are two main types of growth constitutive models: kinematic growth and constrained mixture growth. Kinematic growth is a phenomenon-based model which has been used to create FE models for both concentric [47, 44, 105] and eccentric hypertrophy [47, 112, 44]. Both stress-driven and strain-driven growth laws have been tested in these studies. Constrained mixture growth is a microstructure-based model. It has been used mostly in the context of vascular growth which involves simpler geometry and isotropic properties due to the associated complexity of implementation and high computational cost [88].

Although computational models provide a powerful platform to test different hypothetical growth mechanisms, large amounts of experimental data either at the tissue level (for kinematic growth) or at the cellular level (for constrained mixture growth) are required to facilitate the simulations and validate the models. To date, histology is the most commonly used approach that can provide details about the microstructural changes of the myocardium. However, histology is typically limited to *in vitro* or *ex vivo* studies. Moreover, it is typically evaluated in a small number of regions with a reduced field of view. Consequently, it requires researchers to identify which areas are to be sampled beforehand and, more crucially, it is challenging to repeat longitudinally on the same subject without invasive biopsy. On the other hand, non-invasive imaging techniques such as cardiac magnetic resonance (CMR) can provide information about the macrostructural and functional changes of the heart in multiple pathological and physiological states, including cardiac remodeling [119, 3, 4]. Moreover, the non-invasive nature of CMR allows imaging of the same subject at multiple time points, hence, enabling longitudinal studies. The main limitation of CMR compared to histology is its relatively low resolution, on the order of mm, which impedes the direct observation of cellular shape changes in the heart . In order to perform *in vivo* assessments of the microstructural changes occurring during diseases or exercise, it is necessary to bridge the gap between the macrostructural changes observed with CMR and the underlying microstructural changes in the myocardium.

With CMR data, FE can be used as a forward model to build subject-specific growth simulations and predict the LV morphological changes for given growth parameters. Assuming the governing laws of growth are valid, it is possible to estimate a set of growth parameters that predict the LV geometry observed post-growth from CMR using iterative optimization approaches. Such a technique would provide a quantitative link between growth in myocardial microstructure and morphological changes in the LV geometry. However, subject-specific FE models are computationally expensive and consequently running a large number of iterations within an optimization algorithm becomes prohibitive. In this context, Bayesian Optimization (BO) was developed as a gradient-free optimization technique designed to optimize cost functions that are expensive to evaluate. Hence, BO can be used to optimize over parameterized FE models of the heart without evaluating a grid search, which could take weeks or months to compute per subject.

The aim of this work is to propose an optimization framework to estimate the microstructural changes in the myocardial tissue by combining CMR imaging with FE-based computational models and BO. In short, our approach parameterizes the possible myocardial growth mechanisms (e.g. transverse or longitudinal growth) within an FE model and then estimates the growth parameters that best describe the heart geometry observed with CMR after growth. Since the heart is imaged in its entirety and non-invasively, it is also possible to assess whole-heart changes and perform longitudinal studies to assess progression within the same subject. In this study, we illustrated the accuracy of the FE+BO framework by testing it on multiple synthetic and animal growth models. In all cases, initial and final (post-growth) geometries were obtained and the FE+BO algorithm was used to predict which combination of transverse/longitudinal microstructural growth occurred in the myocardium.

2.2 Materials and Methods

We developed an inverse-problem approach to non-invasively characterize cardiomyocyte growth from CMR and FE models, as described in Figure 2.1. Specifically, we acquired two CMR volumes of the LV at two time points – pre-growth (before starting exercise) and post-growth (after the exercise regime). Next, we built FE models of both LV geometries and applied hemodynamic loading and pericardial constraints to each. Finally, we applied cardiac growth to the pre-growth model and used it to estimate the microstructural cardiac growth parameters that best account for the macrostructural cardiac shape observed in the post-growth model. The overall method is composed of three main components, the myocyte growth model, the computational FE model and the estimation of the growth parameters performed with BO.

2.2.1 Myocardium Kinematic Growth Model

Since we used MRI data as the input information, kinematic growth was chosen instead of constrained mixture growth as the resolution of MRI is better suited for imaging at the macrostructural (i.e. tissue) level. Kinematic growth theory introduces volumetric deformation to a continuum formulation with an approach similar to thermal-elastic coupling. In other words, the growth resulting from cardiomyocyte hypertrophy is modeled as volume increase in the myocardium. Within the kinematic growth framework, the total deformation gradient ($\mathbf{F}$) can be multiplicatively decomposed into an elastic response ($\mathbf{F}^e$) and a growth multiplier ($\mathbf{F}^g$) as shown in Equation 2.1. The former is used to determine the stress in the stress-strain constitutive model and the latter defines the growth magnitude in the three local orthogonal directions of the cardiac microstructure (fiber, sheetlet, and sheet-normal).

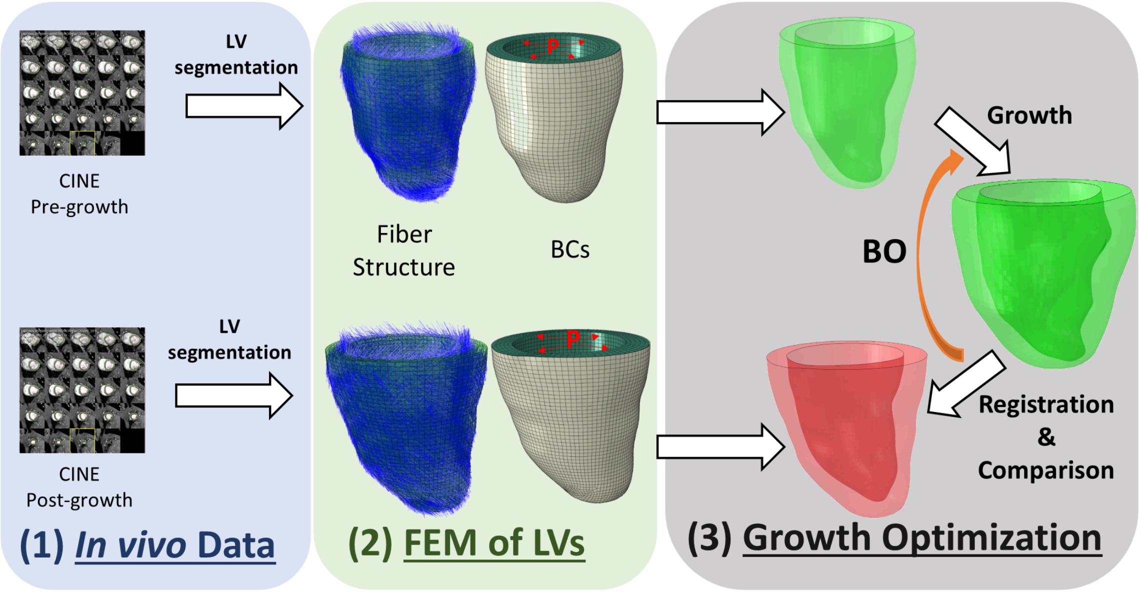

Figure 2.1: Overview of the workflow used to characterize cardiomyocyte growth. The workflow contains three modules: (1) in vivo data collection, (2) building finite element model (FEM) of the pre-growth and post-growth LV geometries with idealized fiber orientation and boundary conditions (BCs) such as end-diastolic pressure and pericardium constraint, and (3) growth optimization. (LV - Left Ventricle, BO - Bayesian Optimization)

$$\mathbf{F} = \mathbf{F}^e \mathbf{F}^g \tag{2.1}$$

As discussed earlier, cardiomyocytes have two main modes of growth, longitudinal and transverse growth, which correspond to series and parallel sarcomerogenesis, respectively. Therefore, we modeled the growth as transversely isotropic, where growth in the fiber direction is associated with longitudinal growth and growth in the sheetlet and sheet-normal directions are associated with transverse growth. The growth multiplier has the form:

$$\mathbf{F}^g = (1 + \alpha_f)\mathbf{f} \otimes \mathbf{f} + (1 + \alpha_n)(\mathbf{n} \otimes \mathbf{n} + \mathbf{s} \otimes \mathbf{s}) \tag{2.2}$$

where f, s, and n are unit vectors corresponding to the fiber, sheetlet and sheet-normal directions that are orthogonal to each other. Similarly, α_f and α_n are the longitudinal and transverse growth coefficients.

For the elastic response of myocardium, the invariant-based hyperelastic model purposed by Holzapfel and Ogden [55] was used. The strain energy density function of the model is shown in Equation 2.3, where I_1^e, I_{4f}^e, I_{4s}^e, and I_{8fs}^e are invariants of the right Cauchy green tensor ($\mathbf{C}^e = \mathbf{F}^{eT}\mathbf{F}^e$) and a, b, a_f, b_f, a_s, b_s, a_{fs} and b_{fs} are material parameters [55]. The 'a' parameters have units of MPa and 'b' parameters correspond to an exponential constant that is dimensionless. The subscripts 'f' and 's' indicate the fiber and sheetlet (normal) directions, respectively. We adopted the material parameters characterized by Sack et al. [110] from swine models, where $a = 1.05$ kPa, $b = 7.542$, $a_f = 3.465$ kPa, $b_f = 14.472$, $a_s = 0.481$ kPa, $b_s = 12.548$, $a_{fs} = 0.283$ kPa, and $b_{fs} = 3.088$.

$$\Psi = \frac{a}{2b} exp(b(I_1^e - 3)) + \sum_{i=f,s} \frac{a_i}{2b_i}\{exp[b_i(I_{4i}^e - 1)^2] - 1\} + \frac{a_f s}{2b_f s}[exp(b_{fs} {I_{8fs}^e}^2) - 1] \tag{2.3}$$

In the FE models that will be described in the next section, the elastic material properties are kept constant while growth parameters α_f and α_n are varied from model to model in the workflow. With the kinematic growth frame work (Equation 2.1), $\mathbf{F}^e$ can be derived from $\mathbf{F}$ and $\mathbf{F}^g$, in which the former is computed as the gradient of the continuous deformation map and the latter is explicitly defined as in Equation 2.2. The second Piola-Kirchhoff stress can then be computed from Fe and strain energy density function (Equation 2.3) as $S = \frac{\partial \Psi}{\partial \mathbf{C}^e}$. More details of the kinematic growth in the continuum mechanics framework are described in [44].

2.2.2 Finite Element Model Analysis

Finite element models apply constitutive models that describe the growth behavior at the tissue level into each element and enable the evaluation of deformation and morphology changes at the organ level. To start building a finite element model of the LV, a 3D volumetric model of its geometry is required. In this study, the LV geometries at end-diastole were generated from *in vivo* CMR imaging using semi-automatic segmentation tool Segment (Medviso) [51]. In order to avoid through-slice discontinuities, the epicardial and endocardial contours from each slice were further smoothed by fitting a smoothing B-spline to the mask control points along the slice direction [101]. The contours were used to create the 3D shape of the LV in finite element software ABAQUS 2018 (Dassault Systèmes, Providence, RI, USA) [31]. The LV was meshed with hexahedron elements (C3D8) with element edge length of approximately 1.5 mm (i.e. a 1.5 x 1.5 x 1.5 mm^3 element), resulting in 4-5 layers of elements across the myocardial wall. An idealized fiber orientation was applied using the Laplace–Dirichlet Rule-Based (LDRB) algorithm [9] with epicardial-endocardial helix angle of -60° to 60°. Standard ABAQUS user subroutines VUHYPER and VUEXPAN [31] were used to implement the Holzapfel-Ogden hyperelastic model and transversely isotropic growth model in ABAQUS. To create pericardial constraints at the epicardium, a 3D shell geometry was obtained from the epicardial surface to model the geometry of the pericardium explicitly. The pericardium was meshed with quadrilateral shell elements (S4) and modelled as a linear elastic material with a Young's modulus of 10 MPa [73]. A frictionless contact interaction was applied between the epicardial surface (Γ_{epi}) and the pericardium surface (Γ_{peri}) using the penalty contact algorithm [31]. A penalty pressure, which is linearly dependent on the overclosure distance (h), was applied on the two surfaces (Equation 2.4). A Dirichlet boundary condition was applied at the basal plane (Γ_{base}) and the basal ring of the pericardium ($C_{base-ring}$) to prevent movement of body in the longitudinal direction (Equation 2.4). A preload step followed by a growth step was implemented into the model. Assuming that the segmented LV geometry is closed to the stress-free configuration, an end-diastolic pressure (p_{ed}) of 10 mmHg was applied on the endocardial surface to obtain the preloaded LV shape in the preload step. The LV pressure was kept constant in the growth step while kinematic growth in the transverse and longitudinal directions were implemented. All the boundary conditions of the model are summarized in Equation 2.4 and are indicated in Figure 2.2.

$$
\begin{aligned}
&\mathbf{FSn} = p_{epi}\mathbf{n} && on \quad \Gamma_{epi} \\
&\mathbf{FSn} = -p_{epi}\mathbf{n} && on \quad \Gamma_{peri} \\
&p_{epi} = 2h && \\
&u_z = 0 && on \quad \Gamma_{base}, C_{base-ring} \\
&\mathbf{FSn} = p_{endo}\mathbf{n} && on \quad \Gamma_{endo} \\
&p_{endo} = \begin{cases} p_{ed}t & t \in [0,1] \text{ (preload step)} \\ p_{ed} & t \in (1,2] \text{ (growth step)} \end{cases} &&
\end{aligned}
\tag{2.4}
$$

(where h is the overclosure distance between the two contacted surfaces)

Due to nonlinearities (large deformation, nonlinear material model, and contact) in the model, the ABAQUS/Explicit solver was used to conduct a quasi-static analysis [31]. The Explicit Dynamic Analysis in ABAQUS is designed to solve the dynamic equilibrium (Equation 2.5). When the inertial force ($\mathbf{M\ddot{u}}$) is small enough, the equation reduces to the static form of equilibrium and therefore leads to a quasi-static problem. The explicit solver uses

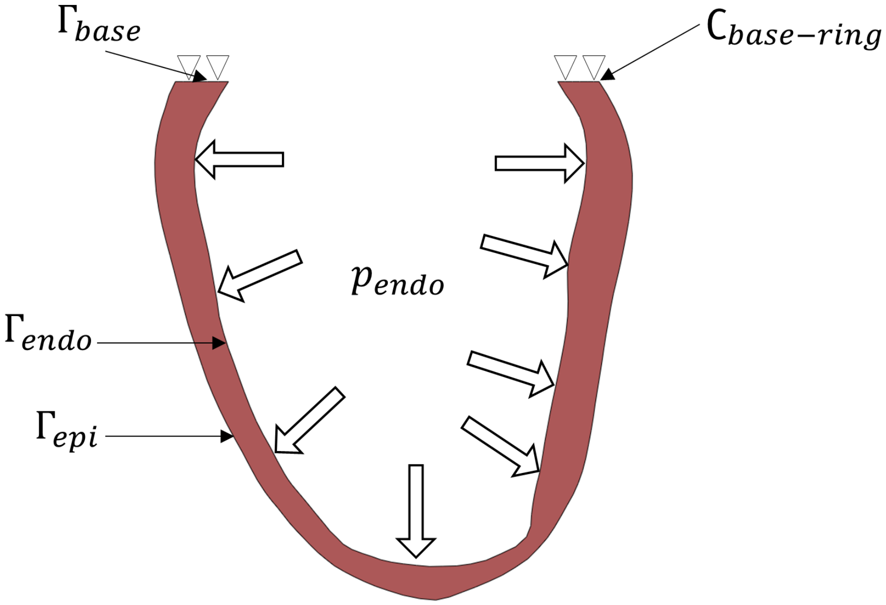

Figure 2.2: An overview of the LV finite element model. (endo - endocardium, epi - epicardium)

the forward Euler method, in which the equations of motion are updated using previous information as shown in Equation 2.6 and 2.7. Preload and growth step time periods were set to 1 using a mass scaling technique and small stable time increments of 5e−6 to ensure that the kinetic energy was negligible ($< 5\%$) compared to the total energy, as suggested in the ABAQUS manual for quasi-static analysis [31]. Hence, the "time" is an arbitrary value that indicates the loading magnitude but does not reflect the actual loading rate. For example, a growth simulation that linearly increases the transverse growth magnitude from 0 to α_0 can provide intermediate outputs at time $t \in [0, 1]$ as the solution of growth with transverse growth magnitude equals $\alpha_0 t$. Figure 2.3 illustrates the macroscopic growth produced by three types of microscopic growth: transverse, longitudinal and isotropic. Transverse growth increased the wall thickness of the LV, longitudinal growth dilated the LV chamber and isotropic growth resulted in both wall-thickening and LV chamber dilation. Both the transverse and longitudinal results agree with clinical observations and histological findings of eccentric and concentric hypertrophy [45].

$$\mathbf{M}\ddot{\mathbf{u}} = \mathbf{P} - \mathbf{I} \tag{2.5}$$

(where $\mathbf{M}$ is the lumped element mass matrix, $\ddot{\mathbf{u}}$ is acceleration, $\mathbf{P}$ is the external force vector, and $\mathbf{I}$ is the internal force vector)

$$\dot{\mathbf{u}}^{i+\frac{1}{2}} = \dot{\mathbf{u}}^{i-\frac{1}{2}} + \frac{\Delta t^{i+1} + \Delta t^{i}}{2}\ddot{\mathbf{u}}^{i} \tag{2.6}$$

$$\mathbf{u}^{i+1} = \mathbf{u}^{i} + \Delta t^{i+1}\dot{\mathbf{u}}^{i+\frac{1}{2}} \tag{2.7}$$

(where $\mathbf{u}$ is displacement and $\dot{\mathbf{u}}$ is velocity, the superscript (i) indicates the increment number and $i - \frac{1}{2}$ and $i + \frac{1}{2}$ refer to mid-increment values)

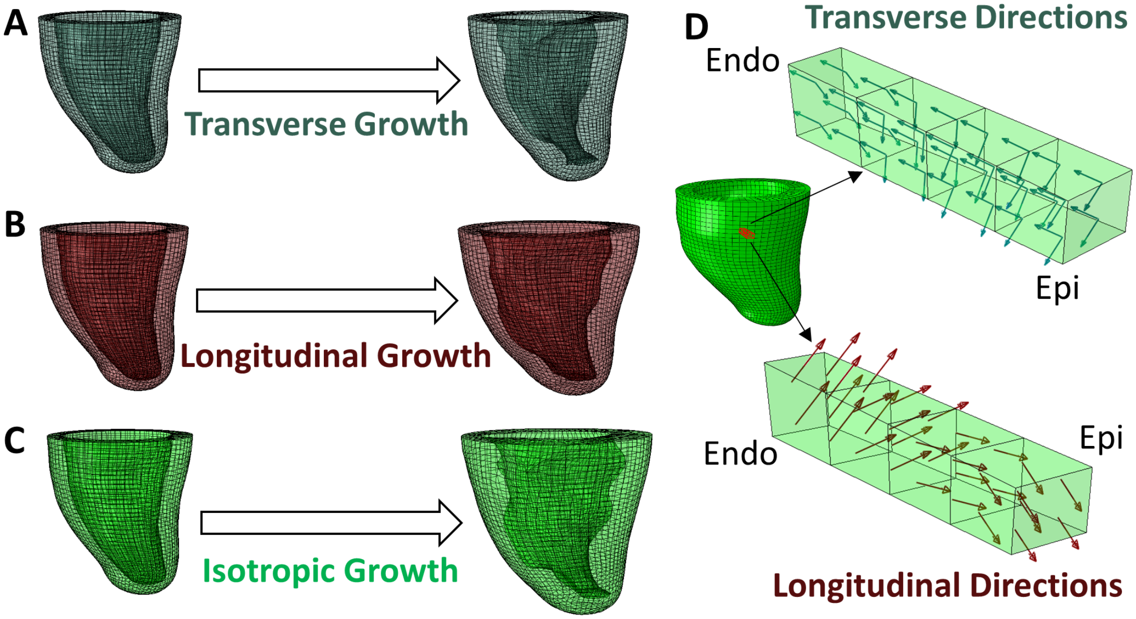

Figure 2.3: Different types of growth evolution predicted by the FE model, (A) transverse growth, (B) longitudinal growth, (C) isotropic growth. (D) Demonstration of transverse and longitudinal growth directions in a block of myocardium from endocardium to epicardium.

2.2.3 Growth Parameter Estimation with Bayesian Optimization

The cardiac growth parameters (α_f,α_n) were estimated by maximizing the similarity between the LV geometries obtained from the growth FE model and from the LV geometry imaged with the second scan. Specifically, we maximized the DICE score [33] between the masks of the FE and CMR geometries ($M_{FE}(\alpha_f, \alpha_n)$ and M_{CMR}, respectively):

$$\max_{\alpha_f,\alpha_n} \frac{2 \mid M_{FE}(\alpha_f, \alpha_n) \cap M_{CMR} \mid}{\mid M_{FE}(\alpha_f, \alpha_n) \mid + \mid M_{CMR} \mid} \tag{2.8}$$

Unfortunately, the cost function in this maximization problem requires solving an FE growth model over the parameters (α_f,α_n) numerically. Hence, it is non-linear, does not have an analytical expression and each iteration is computationally expensive (around 2 hours per iteration). These limitations impede using gradient-descent methods [89, 12] and is computationally infeasible for classical gradient-free methods [86, 100]. Instead, we used Bayesian Optimization (BO), which is a gradient-free optimization method designed for problems whose cost function can only be evaluated at discrete points and which are expensive to compute [64, 91, 60]. At each iteration, BO interpolates the cost function with a Gaussian process [104] using the samples evaluated in previous iterations and then proposes a new point to evaluate within a bounded search space. The optimization is effectively performed in the process of proposing new points to evaluate. These are generated by maximizing an analytical acquisition function that balances the exploration of the search space against the exploitation of current local maxima to further improve the current best result. There have been multiple acquisition functions proposed in the literature, each providing different balances between exploration and exploitation [67, 120, 53, 52], and allowing for the introduction of non-linear constraints to the optimization [52, 5]. In this work, we used the Upper Confidence Bound [120], which maximizes the following trade-off between the mean $\mu(x)$ and variance $\sigma(x)$ of the Gaussian Process, balanced by the scalar parameter β:

$$\max_x \mu(x) + \beta\sigma(x) \tag{2.9}$$

As discussed, the cost function used in BO was the DICE score (DSC) between the masks of the predicted and imaged LV geometries. Evaluation of this cost function requires generating a 3D mask of the LV using the 3D coordinates of the nodes that constitute the FE mesh. In order to generate such mask, we determined which voxels in the 3D volume belong within the LV by interpolating a binary function in each voxel. Specifically, we used kernel density estimation with B-spline interpolation (kernel width of 4 voxels) and interpolated values of '1' at the position of the FE nodes. Finally, we implanted a threshold for the interpolated values at >0.25 and further filtered the resulting binary mask with a morphological closing filter with an element size of 6 voxels to avoid holes in the LV. To ensure that both the FE and CMR masks were aligned, we registered them with a rigid registration algorithm of their nodes in 3D [84].

2.2.4 Experiments

We tested our method with a series of synthetic experiments and further illustrated its application in a real scenario with animal models of exercise-induced cardiac growth. All experiments were done under IACUC-approved protocols at the Massachusetts General Hospital. Four Yucatan swine (2 months old) underwent treadmill exercise training for 12 weeks and were imaged *in vivo* at weeks 0, 6 and 12 after onset of exercise (one swine could not finish exercise before the submission). Cardiac imaging was performed on a 3T clinical MRI system (MAGNETOM Prisma or a Connectome, Siemens Healthineers, Erlangen, Germany) set at max 80mT/m gradient strength and a standard 32-channel antero-posterior surface coil. The animals were anesthetized, placed on a ventilator, and then imaged with a retrospectively ECG gated CINE MRI flow compensated gradient echo sequence (repetition time = 5.8ms, echo time = 3.2ms, flip angle = 20°, 4 averages, 1.4x1.4x2.5mm3, 25 cardiac phases). After imaging, the LV at end-diastole was segmented to generate an FE model as described in the previous section. The FE model and the LV masks at weeks 6 and 12 were then introduced into the optimization framework to estimate the transverse (α_n) and longitudinal (α_f) growth of the myocardium. The optimization was performed in python using the BO implementation in the BoTorch package [6] with Upper Confidence Bound (UCB) as the acquisition function. The parameter β, which balances exploration and exploitation in UCB, was somewhat arbitrarily set to 10 since it provided balance between the mean and variance of the Gaussian Process estimate after initialization. The maximum growth was set to 1 (equivalent to doubling of size), resulting into a search space bounded between 0 and 1 for both growth parameters. The optimization was initialized with 3 samples of growth parameters set to [0, 1], [1, 0], and [1, 1] and BO was run for 10 iterations. Given the numerical nature of the quasi-static FE model, it provided intermediate outputs of growth that could be used as additional samples within the Gaussian Process fitting in BO. Consequently, each growth simulation provided 5 valid cost-function evaluations between zero-growth and the selected combination of transverse and longitudinal growth parameters, and these were introduced into each iteration of the BO algorithm to improve the estimate of the Gaussian Process. In order to evaluate the results, synthetic growth was applied to 3 LV geometries from the previously described swine models. For each LV geometry, the ventricle was modified with 6 randomly prescribed transverse and longitudinal growth parameters. The growth parameters were set to be equal across geometries to reliably compare the results across subjects. Hence, the resulting synthetic dataset consisted of a total of 18 simulations (3 geometries x 6 growth realizations), each with known ground truth for their respective growth parameters. In order to avoid committing an inverse crime "noise" was added in the form of forward model differences between the generation of the synthetic data and the model used within the optimization. Specifically, the synthetic data were generated with increased spatial resolution in the FE meshes (element size reduced to 1 mm from 1.5 mm) and smaller increment step size in the quasi-static growth model (reduced from 5E-6 to 1E-6) in the ABAQUS/Explicit solver. We evaluated the parameter estimation error in the synthetic experiments with the normalized prediction error between the ground truth (α_f^{GT},α_s^{GT}) and predicted (α_s^p, α_f^p) growth parameters:

$$Error = \sqrt{\frac{(\alpha_f^{GT} - \alpha_f^p)^2 + (\alpha_s^{GT} - \alpha_s^p)^2}{\alpha_f^{GT^2} + \alpha_s^{GT^2}}} \tag{2.10}$$

For all experiments, including the real-case examples, we report the final DSC between the predicted growth model and the true LV geometry, and illustrate the similarity between LV geometries with 3D plots, as well as contour plots of the LV masks in short and long axis views.

2.3 Results

An overview of the outputs generated with the FE+BO framework is shown in Figure 2.4. The heatmap in Figure 2.4(A) shows the DSC distribution across two axes of transverse and longitudinal growth parameters. Regions with high DSC were indicative of good alignment between the predicted and true geometries and the parameters with the highest DSC (typically >90%) were identified as the final prediction (indicated with a blue star). The LV geometries that correspond to several iterations in the BO optimization are shown in Figure 2.4 B and C. The 3D views (B) provide clear morphology of the predicted and imaged LVs and the yellow intersection illustrates the volume overlap between them after registration. Similarly, the 2D contours (C), provide a more detailed comparison between target and prediction in two planes. Figure 2.4 illustrates three samples obtained along the optimization and sorted from low to high DSCs . The first example (top row) with parameters α_f=0.1 and α_n=1 showed a thickened LV wall and an elongated chamber, compared to the target LV. The second example (middle row) presented lower transverse growth but higher longitudinal growth (α_f=0.4 and α_n=0.4). In this case, the geometry was more similar to the target one and was characterized by smaller wall thickness and smaller apex-to-base distance. Due to larger longitudinal growth, the chamber was more dilated in the radial direction, compared to the targeted LV. The best example (bottom row) was found for parameters α_f=0.17 and α_n=0.33. Both the 2D contours and the 3D plots are closer to the target LV than that obtained with the previous examples, albeit the LV size was slightly under-predicted.

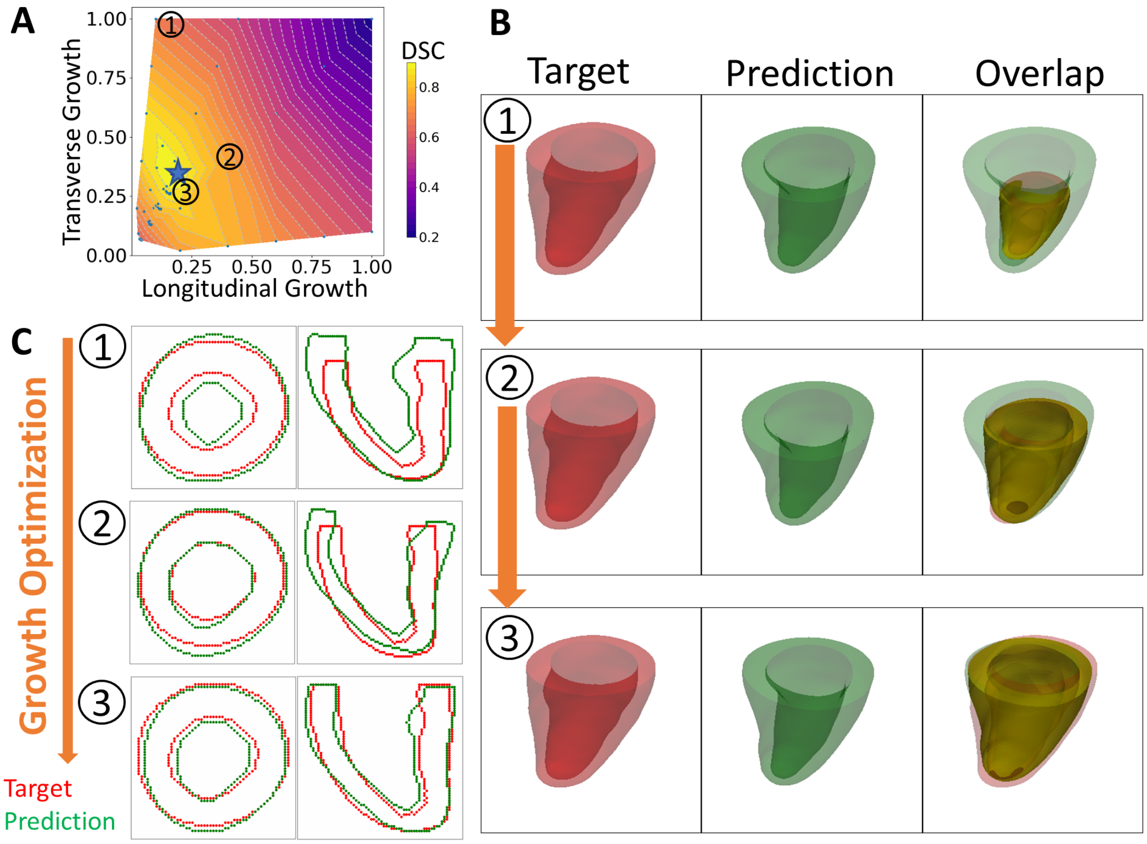

Figure 2.4: An overview of the results. (A) Heatmap of DICE scores (DSC) for different sets of growth parameters. (B) 3D views comparing predicted and targeted geometries at three different scenarios indicated on the heatmap. (C) 2D contour comparison of predicted and targeted geometries from the long and short axis views. (1)-(3) indicate three different sets of growth parameters that were tested during the optimization process. From (1) to (3), the BO method increasingly finds solutions that improve the DICE score.

The DSC heatmaps of the synthetic experiments are shown in Figure 2.4. These illustrate how the FE+BO framework was capable of estimating growth parameters in the synthetic models. In all cases, the DICE score heatmaps resulted in a single local maximum with a peak in the vicinity of the true parameters. Consequently, the estimated growth parameters were similar to those of the ground truths across different LV geometries and growth scenarios. Figure 2.6 (B and C) shows a scatter plot with the estimated and true growth parameters. Both the estimated transverse and longitudinal growth resulted in good alignment with the ground truth (points are near the identity line), although these were respectively underestimated and overestimated (below and above the identity line). Quantitatively, the normalized error of the growth parameters, shown in Figure 2.6 A, was 5.5±5.8% and there was no significant difference in error across different LV geometries. The 2D contours of the predicted and true masks are shown in Figure 2.7. These resulted in good subjective alignment of the predicted LV geometry and that of the ground truth.

An example of the true end-diastolic LV geometries segmented from MRI along different time points during the exercise training (week 0, 6, and 12) is shown in Figure 2.8. From Figure 2.8 D and E, the long-axis view comparisons after rigid registration between the two geometries show LV chamber elongation and dilation is relatively minimum at week 6 but substantial at week 12. Similarly, the short-axis views (Figure 2.8 F and G) show that wall thickening effect is more evident in week 12 than week 6. Quantitative evaluation of LV shape changes during exercise training are shown in Figure 2.9. The LV (n=4) shows an increased end-diastolic (ED) volume (Figure 2.9A), and a significant increase in myocardial volume (Figure 2.9B) as the exercise program progresses. These results are consistent with eccentric hypertrophy. The results of growth characterization on these four exercised animals are shown in Figure 2.10. As reported in the synthetic experiments, all DICE score heatmaps resulted in a single local maximum within the search space. Since this data was obtained *in vivo*, there is no ground truth for the growth parameters. However, the estimated parameters consistently resulted in larger longitudinal growth than transverse growth. In fact, transverse growth values were almost negligible for most of the cases while a continuous increase in longitudinal growth was observed between weeks 6 and 12, except for Swine 1. On average, all animals (n=4) that underwent exercise training resulted in growth parameters (α_f=0.580±0.196 and α_n=0.040±0.080) at week 6 and (α_f=0.793±0.156 and α_n=0.078±0.094) at week 12. The estimated growth parameters for each swine and session

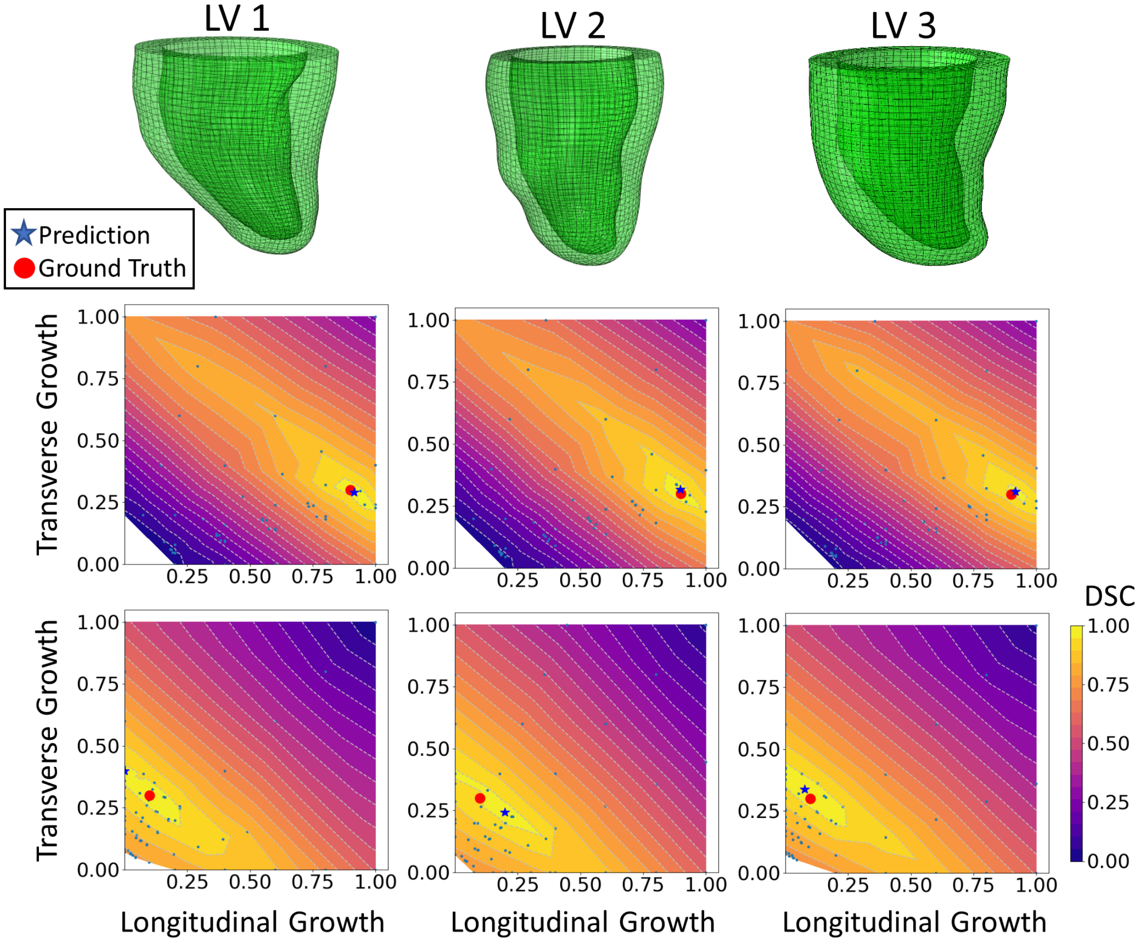

Figure 2.5: DICE score heatmap results of the synthetic experiments. The top row shows the three LV geometries that were used in the synthetic experiments. The final prediction and ground truth are indicated in each heatmap as a blue star and red dot respectively. For each LV geometry, two out of all six cases are shown. The middle row includes examples of growth that is largely dominated by longitudinal growth (α_f=0.9, α_n=0.3) and the bottom shows examples of growth that is largely dominated by transverse growth (α_f=0.1, α_n=0.3).

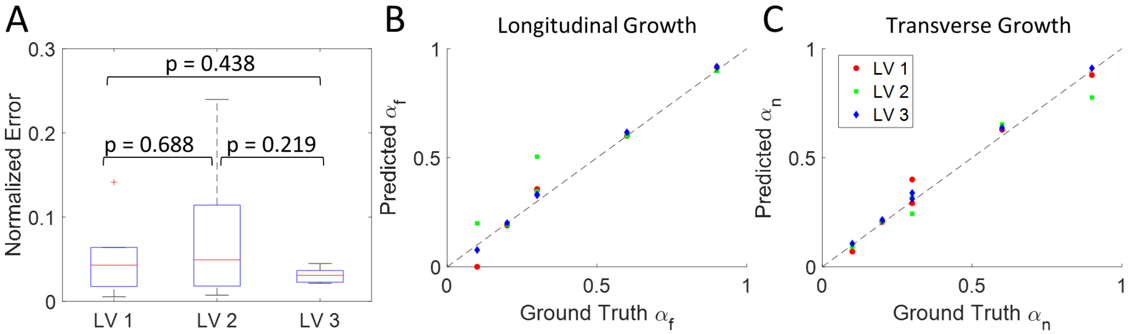

Figure 2.6: Quantitative analysis of the results from 18 synthetic experiments. (A) Boxplot of normalized error across different subjects. (Boxplots show median, interquartile ranges and whiskers show range. P values were calculated using standard t-test.) (B) Scatter plot of predicted longitudinal growth vs ground truth longitudinal growth. (C) Scatter plot of predicted transverse growth vs ground truth longitudinal growth. Dash lines in (B) and (C) indicate the identity line where predictions with zero error should locate on.

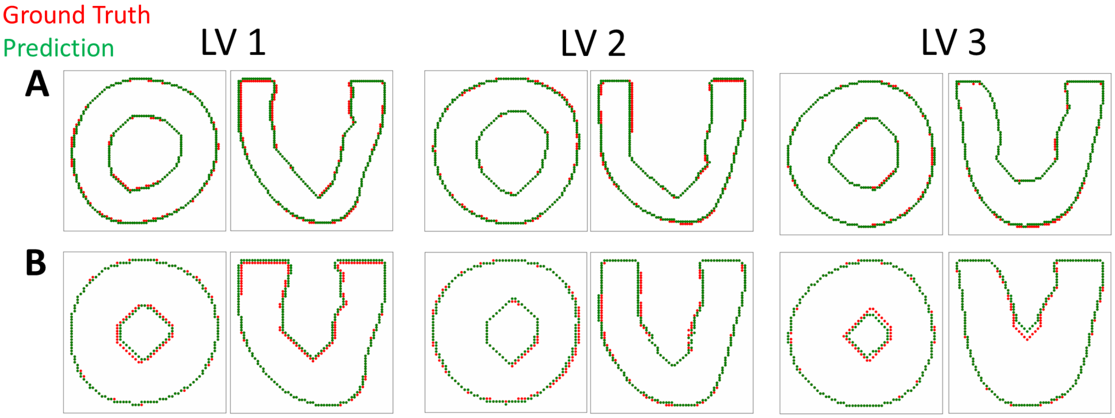

Figure 2.7: Contour plots comparing the predicted and target LV geometry from the short axis and long axis views. The top row (A) includes the longitudinal growth examples (α_f=0.9, α_n=0.3) and the bottom row (B) includes the transverse growth examples (α_f=0.1, α_n=0.3).

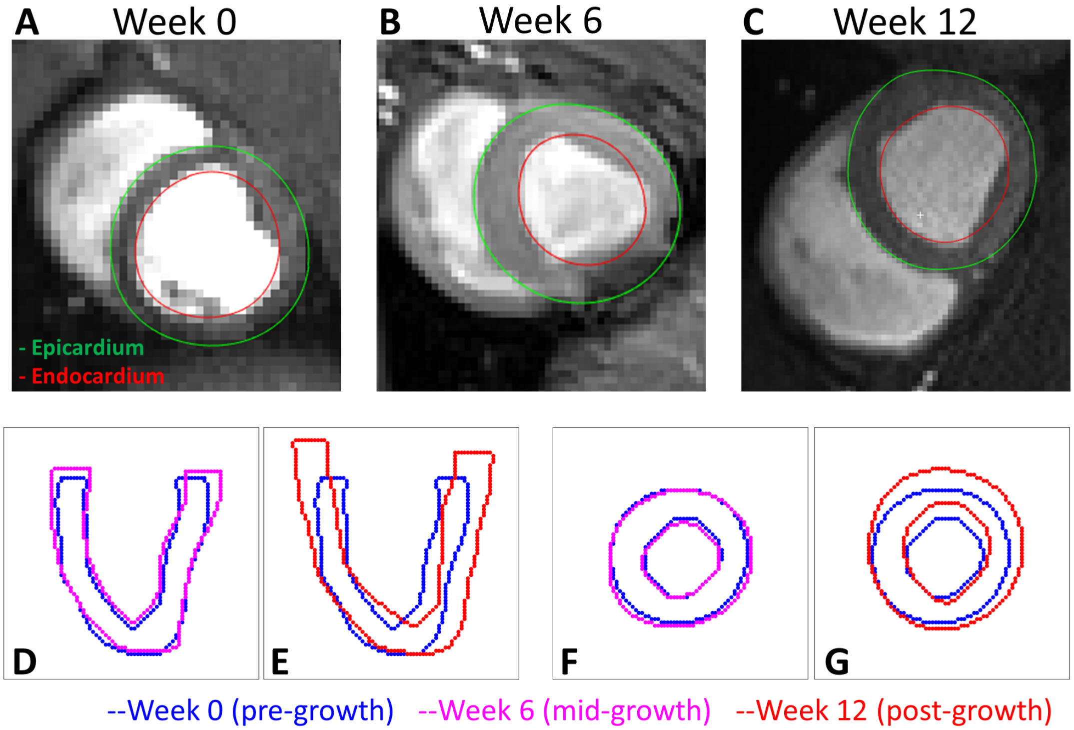

Figure 2.8: A comparison of the LV geometries before and after exercise-induced growth. (A-C) MRI short-axis views of the LVs at week 0, 6 and 12 during exercise training. (D, E) Long-axis views comparing week 0 to week 6 and 12 LV geometries. (F, G) Short-axis views comparing week 0 to week 12 LV geometries. Rigid registrations were performed between the two geometries in D-G.

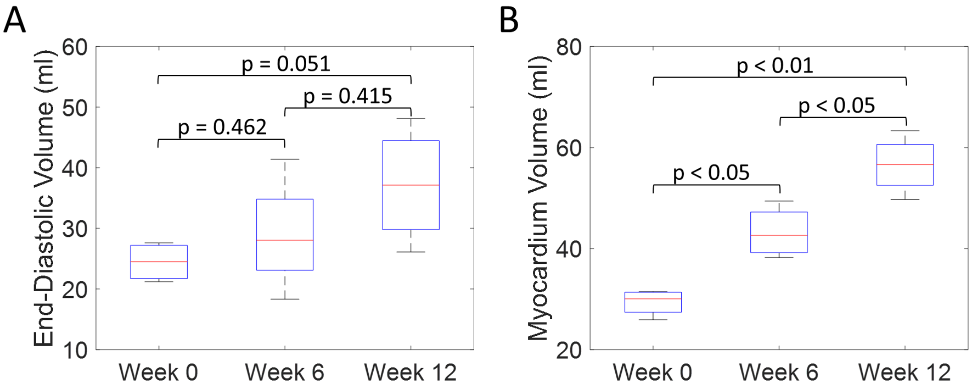

Figure 2.9: Quantitative comparisons of LV end-diastolic volume (A) and myocardium volume (B) between week 0, 6 and 12 during exercise training. (Boxplots show median, interquartile ranges and whiskers show range. P values were calculated using standard t-test.)

are reported in Table 2.1.

	Swine 1		Swine 2		Swine 3		Swine 4	
	α_f	α_n	α_f	α_n	α_f	α_n	α_f	α_n
Week 6	0.86	0.16	0.54	0.00	0.40	0.00	0.52	0.00
Week 12	0.65	0.19	0.70	0.00	0.82	0.12	1.00	0.00

Table 2.1: Predictions of growth parameters in four exercised animals at two time points (week 6 and week 12).

Both the 3D plots and 2D contours of the predicted and target LV geometries are compared in Figure 2.11 for all four animals at week 12. Both visualizations of the LV geometries show that the FE+BO framework was able to find growth parameters that resulted in similar predicted LV geometries to those observed in the in-vivo data. The 2D long-axis views show that the method tends to underpredict chamber elongation, except for Swine 2. On the contrary, overprediction on wall thickening is shown in the short-axis views. From the 3D overlapping views, it is clear that rigid registration realigned the two geometries before calculating the DSC. ED volume and myocardial volume of the preloaded LVs and growth model predicted LVs at week 6 and 12 are shown in Figure 2.12. The optimized growth simulations predicted a continuous increase of myocardium volume at week 6 and week 12 similar to experimental measurements in Figure 2.9B. However, the trend for ED volume elevation, which is shown in the experimental data, was not reproduced in the growth simulations. This indicates that the pericardium constraint may have been over-estimated in the FE model such that longitudinal growth did not provide a sufficient level of LV chamber dilation. Overall, the method shows that exercise growth is more prone to longitudinal growth than transverse growth.

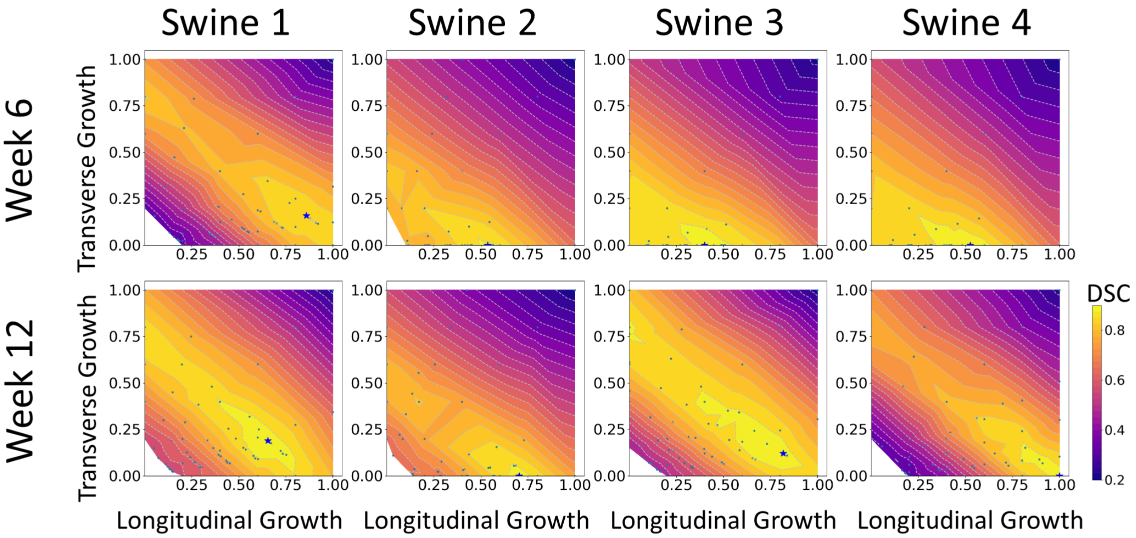

Figure 2.10: DICE score heatmaps of growth parameter prediction for four exercised animals at two different time points (week 6 and week 12).

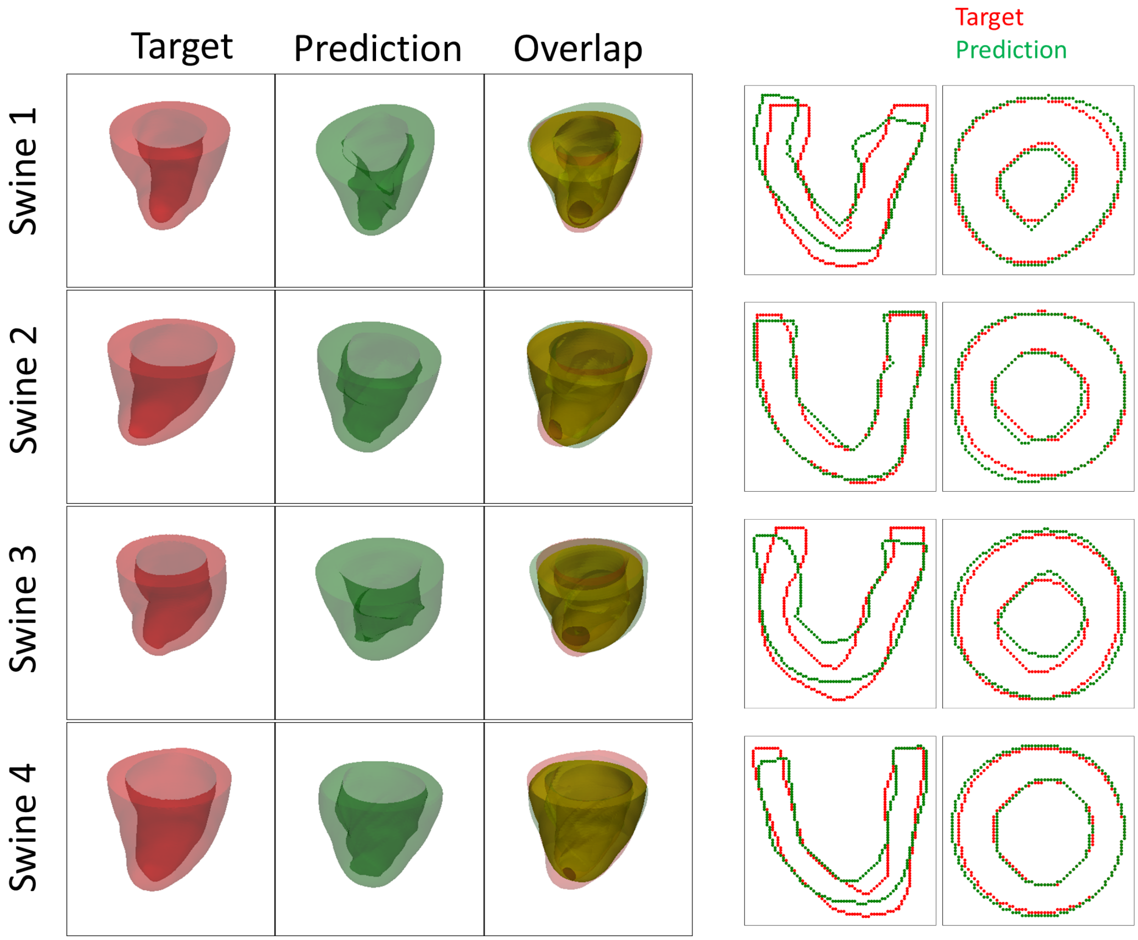

Figure 2.11: Plots of 3D geometries and 2D LV contours to compare the predicted and targeted LV geometries of exercised animals at week 12.

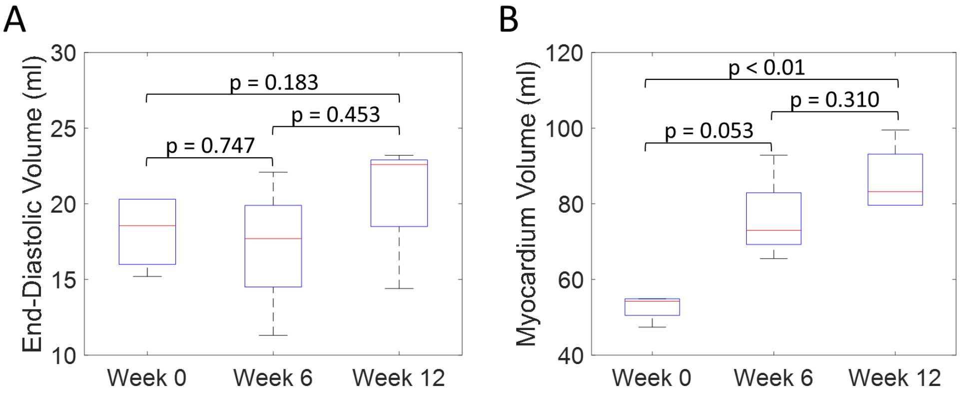

Figure 2.12: Quantitative comparison of end-diastolic volume (A) and myocardium volume (B) between the preloaded LVs at week 0 and the predicted growth LVs at week 6 and week 12. (Boxplots show median, interquartile ranges and whiskers show range. P values were calculated using standard t-test.)

2.4 Discussion and Conclusion

The results of synthetic experiments suggest that the proposed FE+BO framework is capable of estimating the growth parameters of the myocardium with inputs of pre- and post- growth LV geometries. The overall normalized error was 5.5±5.8% and there were no significant differences across heart geometries. In the cases with lower level of growth, especially in the longitudinal direction, the predictions have higher errors. This indicates that the DSC score is more sensitive to transverse growth than longitudinal growth. All DICE scores at the optimal parameters were higher than 90%, presented a single global maxima and the optimized LV geometries were similar to their corresponding ground truths (Figure 2.6), providing confidence on the stability of the estimated parameters. Moreover, the results from the animal model predicted significantly higher levels of longitudinal growth (58% for week 6 and 79.3% for week 12) than transverse growth (4% for week 6 and 7.8% for week 12). Longitudinally, all animals show an increase of growth level in the longitudinal direction from week 6 to week 12, expect for Swine 1 in which the predicted level of longitudinal growth reduces from 86% at week 6 to 65% at week 12. Although minimal, the transverse growth level predicted in Swine 1 and 3 also increases over time during the exercise training process. Performing such longitudinal analysis without the FE+BO framework would only be possible with invasive and potentially hazardous biopsies of the heart. Overall, the growth characterization results suggest that exercise-induced myocardial growth is more prone to longitudinal growth. This is not only consistent with the qualitative LV imaging comparisons showing LV elongation and dilation (Figure 2.8 and 2.9), but also agrees with the literature where running – categorized as aerobic exercise – has been reported to lead to eccentric hypertrophy with longitudinal growth at the cardiomyocyte level in different species [36, 81]. However, the predicted level of growth in the longitudinal direction is much higher than reported cardiomyocyte dimensional increase (15-35%) from literature [130]. This discrepancy is likely due to the over-simplified FE model with generalized material properties, fiber orientation and hemodynamic boundary conditions such that it cannot simultaneously represent concentric and eccentric hypertrophy. In order to refine the subject-specific model, myocardium properties can be characterized using CINE data and dynamic LV models and more realistic fiber orientation can be assigned using cardiac structural information from diffusion tensor imaging data [111]. While LV pressure is difficult to assess non-invasively, the preload step could be improved by using the early-diastolic filling geometry [141] instead of the end-diastolic geometry as the reference configuration such that the preloaded LV configuration is more representative of the ED state. Despite its computational cost, an even more rigorous approach would be to use inverse methods to identify the stress-free LV configuration so that the subsequent preloaded LV geometry should be equivalent to the true ED geometry [131, 106]. Moreover, the cardiac growth process in the swine models was monitored from 2 months old to 6 months old during which time the animals also grow in size. Thus, the results we are seeing may not only contain exercise-induced growth but also physical growth where the LV mass increases as the body weight increases. Further validation of our results with histology is warranted.

The current growth model was designed to characterize growth with two unique parameters for the entire geometry. However, spatially heterogeneous growth is prevalent in patients with hypertrophic cardiomyopathy [75]. To address spatially dependent characterizations, the current model could be extended to include a parameterized spatial distribution of growth and optimize those parameters. Moreover, this framework can be further extended to more sophisticated growth laws (e.g. stretch-driven growth and strain-driven growth). An example of such a model is the work by Costabal et al. [112], who introduced a probabilistic model to connect sub-cellular remodeling to strain-driven myocardium growth. Combination of this method with our current FE+BO framework and optimization of biologically significant parameters such as magnitude, rate, and biomechanical driving factors of growth could yield interesting mechanistic findings. To further improve the capability of our framework to investigate growth at the cellular level, a constrained mixture model can be incorporated.

Despite its complexity and high computational cost, this model can provide a more powerful framework to reveal the mechanistic link between biomechanics at the organ level and biological factors at the tissue-cellular level [88]. Implementing these growth models into our framework would enable efficient *in silico* testing of different growth hypotheses with multi-scale models.

Furthermore, this framework is not limited to growth parameter characterization. Ideally, it can be used as a generic method to characterize material parameters as long as the undeformed and deformed geometries of the object are given in the application. Theoretically, it would be possible to run a grid search parametric study to determine the optimal parameters in these models. However, grid search quickly becomes computationally intractable in the context of FE models due to their expensive computationally costs (around 2 hours with 10 CPUs for each evaluation). For example, for an accuracy of 90% in the growth model presented, it would be needed to compute a grid search with spacing of 0.05. This search would require computing 400 simulations, resulting in 800h (33.3 days) of computation. Instead, the FE+BO approach resolved the maxima within 10 iterations, corresponding to about 20h of computation. Similarly, classical optimization methods (e.g. Simplex, Monte-Carlo) would not be feasible due to the high computational costs of each FE model evaluation. These limitations are set to increase with more complex growth models (longer compute time) or increased dimension of the parameterization (exponentially larger search space). Moreover, the current FE+BO method could be further modified to improve its accuracy and speed-to-convergence. One immediate source of improvement is to modify the acquisition function to incorporate knowledge of the multiple samples generated during the quasi-static FE model evaluations. Currently, we incorporate these samples in the Gaussian process estimation, but the optimization of the acquisition function is done with off-the-shelf UCB, which assumes a single evaluation of the cost function will be provided. This modification would facilitate more efficient sampling of the search space in each BO iteration. Similarly, the selection of the trade-off β parameter in UCB should be done more systematically before the first iteration to balance the mean and variance of the Gaussian Process estimated during initialization.

2.4.1 Limitations

The experimental limitations arise from two aspects: (1) acquisition of the MRI data and (2) segmentation of the LV geometry. The MRI data was acquired with two different scanners with different resolutions (mostly 1.4x1.4x2.5 mm with two exceptions of 1.3x1.3x2.5 mm and 1.8x1.8x6 mm). Lower resolution could reduce the accuracy of segmented LV geometry. The data was acquired along the short axis of the LV, and the actual positions of where the first and last slices reach the base and apex of the LV affect the length of the reconstructed LV geometry. Slice thickness of 2.5 mm is large enough to compare the growth magnitude, especially in the longitudinal direction. Therefore, one or two long axis views of MRI should be acquired and used in future segmentations. A semi-automatic segmentation approach was used in this study and then manually corrected to identify the LV contours in Segment (Medviso)[51]. Further, there are motion artifacts and distortion around the free wall due to field homogeneity caused by the liver. The automatic segmentation method underperforms in these regions and manual corrections are subjective. A more robust automatic segmentation method should be used with minimal manual correction in order to increase reproducibility and reduce human bias.

Another limitation of this framework is introduced by the selection of boundary conditions and tissue properties in the FE model. Model mis-specification can lead to errors in the optimization and result in unrealistic growth parameters. Identifying which models and parameters are most important for an accurate growth selection will be essential in future work. During the development of this study, we found that pericardial constraints are critical for creating realistic concentric hypertrophy in the transverse growth model. In this context, constraints from the pericardium and surrounding tissue at the epicardial surface is even more difficult since there is no clear consensus in the literature about what model to use for dynamic heart modeling. Some studies propose explicitly creating surrounding structures [40], while others propose using "spring-dashpot" surrogates [98] to apply the constraints in dynamic heart modeling. Both models demonstrated the importance of including pericardial constraints on dynamic heart modeling. However, these models might not be applicable in the context of cardiac growth modeling since the heart undergoes gradual deformation at a much longer time scale. Within these time periods, the pericardium and surrounding tissue are likely to undergo their own remodeling, hence changing the constraints to the LV growth. Applying a constant linear elastic material models on the pericardium is likely to over-constrain the epicardium resulting in severe wall-thickening and chamber volume reduction which is shown in Figure 2.12. For future work, it will be important to consider the remodeling of pericardium and surrounding tissue so that more realistic boundary conditions can be applied to the FE model. In addition to the pericardial constraints, sensitivity studies on the LV pressure boundary condition and the initial configuration should be conducted. In this study, the ED state was used for the initial configuration since it is the state that can be consistently identified with CINE MRI and is a geometry that is relatively unaffected by external forces compared to the end-systolic state. For future studies, the growth simulation could be initiated from alternative configurations in the diastolic part of the cardiac cycle (e.g. early-diastolic filling, or diastasis) with different diastolic pressure boundary conditions to check whether the growth optimization results are sensitive to any of these variations.

A limitation of the synthetic experiments is the simplistic source of "noise" added to the generated data which could lead to an overestimation of the accuracy of the synthetic results. In future work more representative noise could include segmentation variability [121], and the post-growth geometry could be generated with a more biologically relevant growth model (e.g. stress/strain-driven growth or constrained mixture growth) to further evaluate the framework performance. However, with our current implementation, such growth models are computationally impractical for whole LV geometries. Further validation is warranted for the animal experiments by comparing histological imaging results to the growth parameters estimated by the model [112].

2.4.2 Conclusion

In summary, this study introduces a Bayesian optimized framework that can be used to non-invasively characterize growth at the tissue level at multiple time points. The FE modeling in this framework enables discernment of mechanistic links between macrostructural imaging and microstructural changes at the tissue level. As such, we believe that the framework can be a powerful tool to reveal fundamental insights into myocardial growth and remodeling mechanisms. In the future, this framework could facilitate the longitudinal study of multiple physiological and pathological conditions and may have practical utility in assessing cardiac disease progression or response to therapy.

Chapter 3

Using constrained mixture growth theory to simulate cardiac growth and remodeling

3.1 Introduction

Growth in biological tissue is a broad-ranging process, impacting all organs and stages of life, from the subcellular to the organ level. It begins with the turnover of biological materials within cells, leading to cell division and differentiation, and culminates in significant morphological changes in every organ. This omnipresent process spans from the rapid physiological growth seen in newborns to the cell proliferation in disease states during adulthood. Given its pervasiveness, studying growth becomes essential. Understanding these growth dynamics can provide crucial insights, contributing to therapeutic advancements, improved disease management, and the overall progress of biomedical science.

By considering the way growth alters a body, it can be broken down into three distinct processes: growth, remodeling, and morphegenesis. 'Growth' indicates the change of mass and volume. 'Remodeling' represents the evolution of material properties (e.g. stiffness, fiber structure). 'Morphogenesis' refers to formation of new tissues and organs achieved through reorganization and differentiation of cells. From a spatial perspective, growth can happen at a tip (e.g. growth of neurons), on a surface (e.g. formation of teeth, skin regeneration and healing), or in a within a volume (e.g. any organ development, solid tumor formation). In adult hearts, the growing process is considered volumetric and has both the growth and remodeling aspects.

Cardiac growth and remodeling (G&R), especially within the left ventricle (LV), can be broadly categorized based on both the anatomical changes and the underlying physiological or pathological triggers responsible for those changes. Physiological hypertrophy, often induced by exercise, is marked by an increase in both chamber size and wall thickness without the presence of fibrosis or fetal gene expression. In contrast, pathological G&R, commonly provoked by pressure or volume overload, are frequently linked with upregulation of fetal gene, fibrosis, and dysfunctional myocyte [80]. Specifically, pressure overload usually leads to concentric hypertrophy, manifesting macroscopically as increased wall thickness and microscopically through parallel sarcomerogenesis with substantial fibrosis. Volume overload typically results in eccentric hypertrophy, expressing macroscopically as wall thinning and ventricular chamber dilation, and microscopically characterized by sarcomerogenesis in series with minimal fibrosis [66]. Interestingly, both physiological and pathological growth exhibit some degrees of reversibility, often in response to the removal of the growth stimuli. For example, in exercise-induced growth, the reverse remodeling occurs once training is ceased or reduced [94]. Conversely, pathological growth may be reversed through the implantation of the left ventricular assist device (LVAD), which is a pump designed to redirect blood flow from the LV to the aorta for heart failure patients. It has been shown that in patients, when the failing heart is unloaded by the LVAD, the native heart is also under-going reverse remodeling [17]. Therefore, understanding the underlying mechanisms and reversibility of cardiac G&R holds significant clinical interest.

In silico models of cardiac biomechanics play an important role in the pursuit of understanding cardiac G&R as previously reviewed by others [140, 88, 118]. Predominantly, these efforts have utilized the kinematic growth theory [108], multiplicatively decomposing deformation into elastic and growth-related components. Within this framework, various growth constitutive laws, either strain-driven or stress-driven, have been purposed to modeling concentric and/or eccentric hypertrophy [136]. More recent studies, including ours shown in Chapter 2, incorporated imaging data and machine learning to identify different growth characteristics [95, 112, 35]. Although these studies demonstrated the efficacy of the kinematic growth framework, they also highlight a critical limitation: the inability to capture remodeling and changes in tissue properties resulting from microstructure variations.

The constrained mixture growth theory [59], which describes the turnover of each tissue component separately, has emerged as an ideal alternative for modeling such microstructural adaptations. Historically, this modeling framework has been applied primarily to vascular G&R due to its computational complexity and challenges in generalizing to 3D. However, the recent introduction of a simplified model known as the homogenized constrained mixture model [26] has significantly reduced computational demands and has been successfully extended to 3D [15]. These advancements open up exciting possibilities for employing this microstructurally motivated theory to recreate the complex processes that occur during cardiac G&R.

The main goal of this study is to leverage the homogenized constrained mixture model (HCMM) to develop multiscale simulations of cardiac growth and remodeling (G&R), thus connecting experimental findings from cellular to organ levels. In particular, we implement the HCMM to simulate cardiac G&R triggered by an increase in left ventricular (LV) end-diastolic pressure, also known as the LV pre-load. Moreover, the model is extended to simulate reverse remodeling (RR) brought about by LVAD intervention. We demonstrate the capability of using the model to tack the changes of various tissue components throughout the G&R process and its reversal. By employing the RR model, we conduct *in silico* studies to investigate the effects of LVAD implantation time on RR, as well as the influence of intrinsic growth parameters on this process. These studies substantiate the potential of such a multiscale model to serve as a platform to explore therapeutic interventions for heart failure patients and provide clinically useful information, thereby enhancing patient-specific care.

3.2 Materials and Methods

In this section, we first provide a brief overview of the fundamental frameworks of continuum mechanics, within which the constrained mixture growth theory is established. Following this, we delve into the homogenized constrained mixture theory (Section 3.2.2) and its realization in modeling myocardium G&R (Sections 3.2.3 to 3.2.7). Finally, we describe the bi-ventricular finite element model following with a demonstration of its application in simulating the reverse remodeling process.

3.2.1 Basics of Continuum Mechanics: Kinematics and Equations of Motions

Let a continuous body with reference configuration $\mathscr{B}_0 \subset \mathbb{R}^3$ undergo a deformation to the current configuration $\mathscr{B}_t$ at time $t \geq 0$. The deformation gradient $\mathbf{F} = \frac{\partial \mathbf{x}}{\partial \mathbf{X}}$ describes a mapping from the reference material point $\mathbf{X} \in \mathscr{B}_0$ to its current position $\mathbf{x}(t, \mathbf{X}) \in \mathscr{B}_t$. The determinant, also known as the Jacobian ($J = |\mathbf{F}|$), therefore maps the reference volume elements dV to the deformed volume elements $dv = JdV$. For incompressible materials, the Jacobian is equal to 1.

For hyperelastic material models, a constitutive equation for the strain energy density $\Psi(\mathbf{F})$ defines the material behavior with the first Piola-Kirchhoff stress:

$$\mathbf{P} = \frac{\partial \Psi}{\partial \mathbf{F}} \tag{3.1}$$

By definition, the Cauchy stress ($\boldsymbol{\sigma}$) and the second Piola-Kirchhoff stress ($\mathbf{S}$) can be written as the following:

$$\boldsymbol{\sigma} = \frac{1}{J}\mathbf{P}\mathbf{F}^T \tag{3.2}$$

$$\mathbf{S} = \mathbf{F}^{-1}\mathbf{P} = \frac{\partial \Psi}{\partial \mathbf{E}} \tag{3.3}$$

where $\mathbf{E} = \frac{1}{2}(\mathbf{C} - \mathbf{I}) = \frac{1}{2}(\mathbf{F}^T\mathbf{F} - \mathbf{I})$ is the Green-Lagrange strain tensor, $\mathbf{C}$ is the right Cauchy-Green tensor, and $\mathbf{I}$ is the identity tensor.

Since the G&R happens under very long time scales (days to weeks), the process is modeled under a quasi-static assumption where the balance of linear momentum can be written as

$$\nabla \cdot \mathbf{P} + \varrho_0 \mathbf{b}_0 = \mathbf{0} \tag{3.4}$$

where ϱ_0 is the mass density per unit reference volume, and $\mathbf{b}_0$ is the body force per unit mass. Unlike in the classical continuum mechanics, mass density in the constrained mixture model is changing over time and can be computed from the mass density in the reference configuration as:

$$\varrho = \frac{\varrho_0}{|\mathbf{F}|} \tag{3.5}$$

3.2.2 Homogenized Constrained Mixture Model of Myocardium

In HCMM, the total deformation gradient is decomposed into the elastic part ($\mathbf{F}_e^i$) and the in-elastic part ($\mathbf{F}_{gr}^i$) for each individual constituent i (Equation 3.6). The latter is also known as the growth and remodeling part which can be further decomposed into $\mathbf{F}_g^i$ and $\mathbf{F}_r^i$ (Equation 3.7).

$$\mathbf{F} = \mathbf{F}_e^i \mathbf{F}_{gr}^i \tag{3.6}$$

$$\mathbf{F}_{gr}^i = \mathbf{F}_r^i \mathbf{F}_g^i \tag{3.7}$$

$\mathbf{F}_e$ describes the elastic deformation of the body due to external forces and therefore is the only deformation gradient the strain energy density function depends on. On the other hand, $\mathbf{F}_r^i$ captures changes in microstructure due to stress imbalance and $\mathbf{F}_g^i$ is associated with the change of mass per unit reference volume due to mass imbalance during the turnover process. Under this framework, three types of constitutive relations are needed, in addition to the proper initial and boundary conditions, to close the system of equations and enable computation of the mechanical equilibrium configuration of the body at each time instance. (1) The mechanical constitutive equations that define the strain energies W_i for the Cauchy stress to compute the elastic material behavior. (2) The mechanobiological constitutive equations that define the evolution of the remodeling deformation gradient. (3) The changes in mass densities depending on mechanical stimuli that determine the evolution of the growth deformation gradient. (2) and (3) are also known as the growth laws.

Mechanical constitutive laws: The myocardium is considered to have three types of constituents, elastin (el), collagen (co), and myocyte (my). The total mass density per unit reference volume is therefore:

$$\varrho_0 = \sum \varrho_0^i \qquad (i = el, co, my) \tag{3.8}$$

Similarly, the total strain energy function per unit reference volume is:

$$\Psi = \sum \Psi^i = \sum \varrho_0^i W^i \tag{3.9}$$

where Ψ^i and W^i are the strain energies per unit reference volume and mass of each constituent, respectively. For all constituents, hyperelastic material models, which are widely used for modeling biological tissues, are chosen as their strain energy density equations. In particular, the elastin matrix is modeled with a 3D Neo-Hookean model as:

$$W_{3D}^{el} = \frac{\mu}{2}(tr(\bar{\mathbf{C}}_e^{el}) - 3) \tag{3.10}$$

Both collagen and myocyte are considered as quasi-1D materials aligning with the unit direction vector $\mathbf{a}_0^i$ in the reference configuration. And their inelastically deformed intermediate configuration can be represented as:

$$\mathbf{a}_{gr}^i = \frac{\mathbf{F}_{gr}^i \mathbf{a}_0^i}{|\mathbf{F}_{gr}^i \mathbf{a}_0^i|} \qquad (i = co, my) \tag{3.11}$$

Under this assumption, both collagen and myocyte are modeled using a quasi-1D Fung-type constitutive law as:

$$W_{1D}^i = \frac{k_1^i}{2k_2^i}(e^{k_2^i (I_a^i - 1)^2} - 1) \qquad (i = co, my) \tag{3.12}$$

where $I_a^i = \mathbf{C}_e^i : (\mathbf{a}_{gr}^i \otimes \mathbf{a}_{gr}^i) = \mathbf{C}_e^i : \mathbf{A}_{gr}^i = {\lambda_e^i}^2$ is the pseudo-invariant. (Note that an arbitrary direction tensor $\mathbf{a}_m \otimes \mathbf{a}_m$ is abbreviated as $\mathbf{A}_m$ and we will use these expression interchangeably henceforward.) The quasi-1D material implies incompressibile behavior. In order to enforce the incompressibility of the myocardium as a whole, an additional volumetric penalty term is included for the elastin extracellular matrix as:

$$W_{vol} = \varepsilon(|\mathbf{F}_e^{el}| - 1)^2 \tag{3.13}$$

Therefore, Equation 3.9 becomes:

$$\Psi = \sum \varrho_0^i W^i + W_{vol} \tag{3.14}$$

Growth and remodeling constitutive laws: In the constrained mixture theory, different constituents are assumed to undergo continuous deposition and degradation at different rates, where new mass deposits with pre-stress $\boldsymbol{\sigma}_{pre}^i$ at a rate $\dot{\varrho}_{0+}^i \geq 0$ while extant mass degrades at rate $\dot{\varrho}_{0-}^i \geq 0$. This results in a net rate of mass production $\dot{\varrho}_0^i = \dot{\varrho}_{0+}^i - \dot{\varrho}_{0-}^i$, which is also known as mass turnover. Growth and remodeling are the results of mass turnover. Therefore, in order to model the mechanobiological behaviors of growth and remodeling, we first need to construct a mass production law. Here, we assume the mass production is driven by the difference between the stress in the current state and in the homeostatic state, resulting in the following constitutive relation:

$$\dot{\varrho}_o^i(t) = \varrho_0^i(t) k_\sigma^i \frac{\sigma^i - \sigma_h^i}{\sigma_h^i} \tag{3.15}$$

where k_σ^i is the growth rate, $\sigma_h^i = \boldsymbol{\sigma}_h^i : \mathbf{A}_0^i$ is the homeostatic stress at the fiber direction $\mathbf{a}_0^i$, and $\sigma^i = \boldsymbol{\sigma}_R^i : \mathbf{A}_0^i$ is the current corotated stress ($\boldsymbol{\sigma}_R^i = \mathbf{R}^T \boldsymbol{\sigma}^i \mathbf{R}$) at the fiber direction $\mathbf{a}_0^i$.

Growth is a result of imbalanced mass turnover (i.e. $\dot{\varrho}_o^i(t) = 0$) which is in general associated with volume changes in the current body. Therefore, it has to happen in the mixed material level. In other words, all constituents are experiencing the same growth deformation gradient (i.e. $\mathbf{F}_g = \mathbf{F}_g^i$). Here, we implemented anisotropic growth in direction $\mathbf{a}_g$ which results in the following form of growth deformation gradient:

$$\mathbf{F}_g = \frac{\varrho_0(t)}{\varrho_0(0)} (\mathbf{a}_g \otimes \mathbf{a}_g) + (\mathbf{I} - \mathbf{a}_g \otimes \mathbf{a}_g) \tag{3.16}$$

Remodeling, which describes the change of microstructure in the tissue, is the result of mass turnover in general. It is assumed to only happen in collagen and myocyte as the elastin turnover rate is small enough to be neglected. The remodeling deformation gradient in quasi-1D materials can be written as:

$$\mathbf{F}_r^i = \lambda_r^i \mathbf{A}_0^i + \frac{1}{\lambda_r^i} (\mathbf{I} - \mathbf{A}_0^i) \tag{3.17}$$

where λ_r^i is the remodeling stretch. It is worth pointing out that, unlike growth, remodeling exists even under balanced mass turnover (i.e. $\dot{\varrho}_o^i(t) = 0$). This is due to the fact that newly added mass has a pre-stress ($\boldsymbol{\sigma}_{pre}^i$) which is different from the current Cauchy stress ($\boldsymbol{\sigma}^i$) of the extant mass that is being degraded. This will therefore change the traction-free state leading to microstructural adaption in the tissue. According to Cyron et al. [26], the evolution equation of $\mathbf{F}_r^i$ can be derived into:

$$\left[\frac{\dot{\varrho}_0^i(t)}{\varrho_0^i(t)} + \frac{1}{T^i}\right]\left[\mathbf{S}^i - \mathbf{S}_e^i\right] = 2\frac{\partial \mathbf{S}^i}{\partial \mathbf{C}_e^i} : \mathbf{C}_e^i \mathbf{L}_r^i \tag{3.18}$$

The remodeling velocity gradient ($\mathbf{L}_r^i$) is defined as:

$$\mathbf{L}_r^i = \dot{\mathbf{F}}_r^i (\mathbf{F}_r^i)^{-1} \tag{3.19}$$

and can be further simplified under the quasi-1D assumption as:

$$\mathbf{L}_r^i = \dot{\lambda}_r^i \left[\frac{1}{\lambda_r^i}(\frac{3}{2}\mathbf{A}_{gr} - \frac{1}{2}\mathbf{I})\right] \tag{3.20}$$

with the initial pre-stretch $\lambda_r^{i(0)} = 1/\lambda_{pre}^i$.

3.2.3 Pre-stress

The *in vivo* configuration of biological tissue is in general not a stress-free configuration. According to the constrained mixture theory, each constituent has its own stress-free configuration and is under stress in the *in vivo* configuration. At a healthy (preferable) *in vivo* configuration, this stress is defined as the homeostatic stress (σ_h^i) and the associate stretch is the homeostatic stretch (λ_h^i). Homeostatic stretches for both collagen and myocyte are explicitly defined to yield specific homeostatic stress according to Braeu et al. [15]. On the other hand, the 3D elastin matrix, which has a low turnover rate [24] and therefore is not subject to G&R, does not have a homeostatic configuration to be maintained. This provides an opportunity to implicitly define the elastin pre-stretch deformation gradient locally such that it can counter the deformation due to external loads and internal stresses applied from collagen and myocyte. In other words, the elastin pre-stretch can recover the *in vivo* configuration under physiological external loads and internal pre-stress. Here, we use a pre-stress algorithm [83] to iteratively calculate the elastin pre-stretch deformation gradient such that it can yield a pre-stressed configuration that is similar, if not identical, to the *in vivo* configuration. This pre-stress procedure starts from applying external loads and pre-stretches ($\mathbf{F}^i_{pre} = \lambda^i_h \mathbf{A}^i_0 + 1/\sqrt{\lambda^i_h}(\mathbf{I} - \mathbf{A}^i_0)$) of collagen and myocyte which result in global deformation ($\mathbf{F} \neq 1$). The elastin pre-stretch deformation gradient is then iteratively updated as:

$$\mathbf{F}^{el}_{k+1,pre} = \mathbf{F}\mathbf{F}^{el}_{k,pre} \tag{3.21}$$

where $\mathbf{F}^{el}_{0,pre} = \mathbf{I}$. This process is repeated until the maximum nodal displacements between the *in vivo* reference configuration and the pre-stressed configuration falls below a prescribed tolerance, $\xi = 0.01$.

3.2.4 Model Implementation and Material Parameters

The HCMM of myocardium was implemented as a user material subroutine (UMAT) in Abaqus/Implicit [31] via Fortran. The UMAT requires five steps of simulation which is demonstrated schematically in Figure 3.1. First, the nodal coordinates at the reference configuration are saved. Second, external loads and pre-stretch of the collagen and myocyte are applied resulting in a global deformation. Third, the pre-stress algorithm is applied to calculate the pre-stretch deformation gradient of the elastin as well as the homeostatic stresses of the collagen and myocyte. Forth, a growth stimuli (e.g. a variation in external loads) is applied to shift the stress deviate from its homeostatic condition. Finally, the growth and remodeling is initiated, aiming to bring the entire body back to mechanobiological homeostasis. Material parameters for myocardium are summarized in Table 3.1. Both the G&R parameters and elastic parameters of the collagen were adapted from Braeu et al. [15] while the elastic parameters of the elastin and myocyte were adapted from Xi et al. [137].

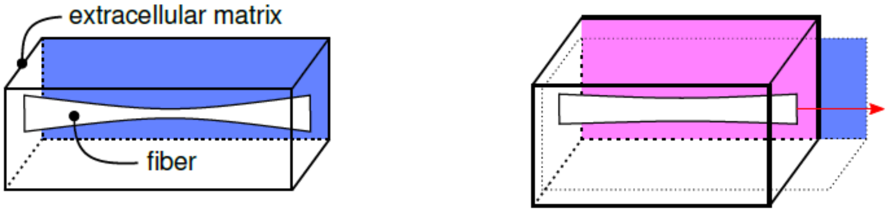

Step 1: Save the initial coordinates and calculate the homeostatic stress

Step 2: Compute the deformed geometry under prestress and homeostatic loading

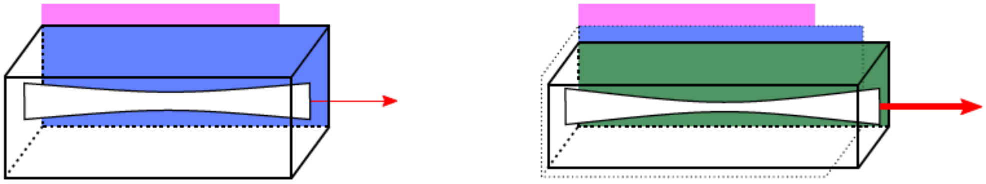

Step 3: Employ an inverse analysis to obtain the initial geometry

Step 4: Initiate a disturbance from the homeostatic state by increasing the load

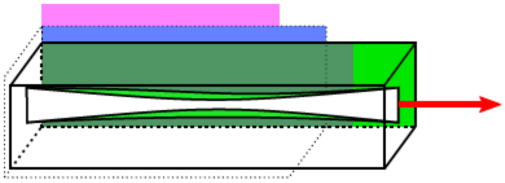

Step 5: Initiate the G&R

Figure 3.1: Five simulation steps in the HCMM UMAT.

Name	Parameter	Value
Collagen elastic parameters	k_1^{co}	568.0E6 $[mJ/kg]$
	k_2^{co}	11.2 [ ]
Myocyte elastic parameters	k_1^{my}	6.74E6 $[mJ/kg]$
	k_2^{my}	9.147 [ ]
Elastin elastic parameters	μ	6.0 $[MPa]$
	ε	6.0E3 [ ]
pre-stretch	λ_{pre}^{co}	1.062 [ ]
	λ_{pre}^{my}	1.1 [ ]
Density	ϱ_0	1.1E-9 $[t/mm^3]$
Volume fraction	φ_0^{co}	0.026 [ ]
	φ_0^{my}	0.7 [ ]
	φ_0^{el}	0.274 [ ]
Turnover time	T^{co}	101 [days]
	T^{my}	101 [days]
Growth gain	k_σ^{co}	$0.2/T^{co}$
	k_σ^{my}	$0.2/T^{my}$

Table 3.1: Summary of material parameters

3.2.5 Collagen fiber families

While the myocyte are oriented only in the global fiber direction $\mathbf{x}_0$, the collagen fibers point in several directions, surrounding the myocyte. To simulate remodeling in the blood vessel plane [15], four directions of the collagen were used, the reason being that the G&R is realized by a change in the density ϱ_0^i w.r.t the volume in the reference configuration. This means that for remodeling from the 0° to the 90° fiber to occur, there must be comparable to the ansatz-functions within a finite element, an additional diagonal fiber that allows the interchange between the two orthogonal directions. We extend this to a 3D case where 13 fiber directions are considered, as shown in Figure 3.2, with three fibers parallel to the axes, two fibers between each axis pair, and four fibers in the diagonal directions that allow remodeling between the orthogonal planes.

Having different groups of collagen fibers arranged in various directions provides extra flexibility to adjust the elastic material behavior at the mixed level. Even the elastic parameters of each constituent are fixed, we can tune the elastic response of the entire myocardium

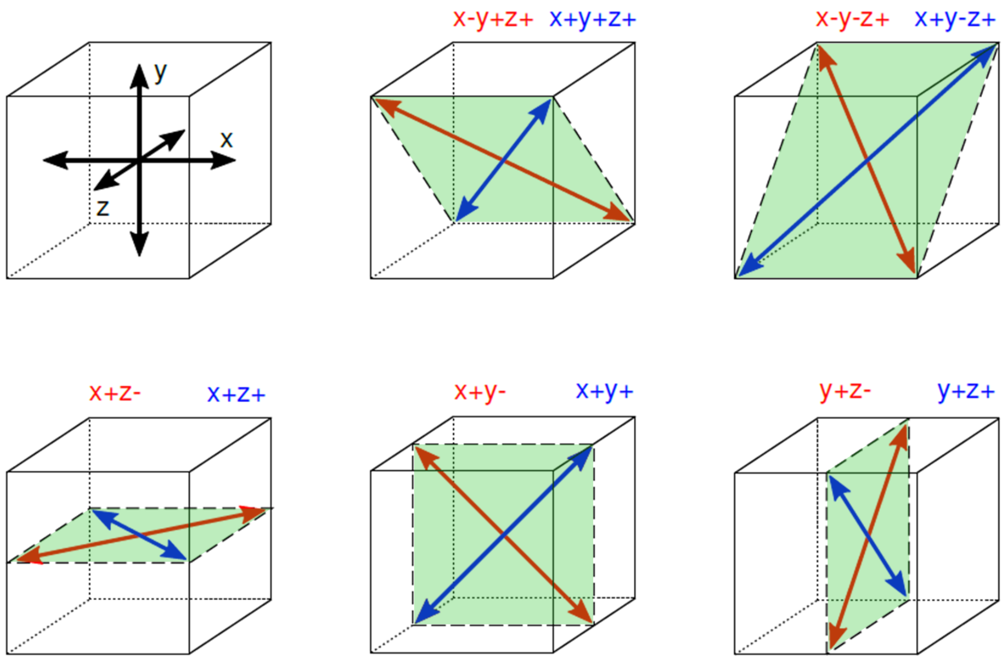

Figure 3.2: Fiber directions of the collagen in the myocardium.

model by adjusting the volume fractions of each group of collagen fibers. The volumes of 13 collagen families are set with five volume fraction parameters:

$$
\begin{aligned}
&\tilde{\varphi}_{x} \\
&\tilde{\varphi}_{y} = \tilde{\varphi}_{z} \\
&\tilde{\varphi}_{xy+} = \tilde{\varphi}_{xy-} = \tilde{\varphi}_{xz+} = \tilde{\varphi}_{xz-} \\
&\tilde{\varphi}_{yz+} = \tilde{\varphi}_{yz-} \\
&\tilde{\varphi}_{x+y+z+} = \tilde{\varphi}_{x+y+-z+} = \tilde{\varphi}_{x-y+z+} = \tilde{\varphi}_{x-y-z+}
\end{aligned}
\tag{3.22}
$$

where the volume fraction of each fiber family is $\varphi_i^{col} = \varphi^{col}\tilde{\varphi}_i$ with $\sum \varphi_i^{col} = \varphi^{col}$. We tuned the parameters to match the elastic response of the Holzapfel-Ogden model [55] (same as Equation 2.3) in a single cube element under the biaxial test. The Isight engine (*Simulia*, Providence,RI) was used coupling with Abaqus [31] for this parameter optimization task

Parameter	$\tilde{\varphi}_x$	$\tilde{\varphi}_y$	$\tilde{\varphi}_{xy+}$	$\tilde{\varphi}_{yz+}$	$\tilde{\varphi}_{x+y+z+}$
Value	0.1008	0.1178	0.0001	0.2091	0.0612

Table 3.2: Volume fraction parameters of collagen fiber families

where the objective function was defined as:

$$\sum_i (\sigma_{i,HCMM} - \sigma_{i,HO})^2 \qquad i \in \{x, y\} \tag{3.23}$$

with the constraint

$$\sum_i \tilde{\varphi}_i = \tilde{\varphi}_x + 2\tilde{\varphi}_y + 4\tilde{\varphi}_{xy+} + 2\tilde{\varphi}_{yz+} + 2\tilde{\varphi}_{x+y+z+} = 1 \tag{3.24}$$

The NLPQLP algorithm was used for the optimization with default settings. The optimal volume fraction parameters are summarized in Table 3.2 with the stress-strain curves comparison shown in Figure 3.3.

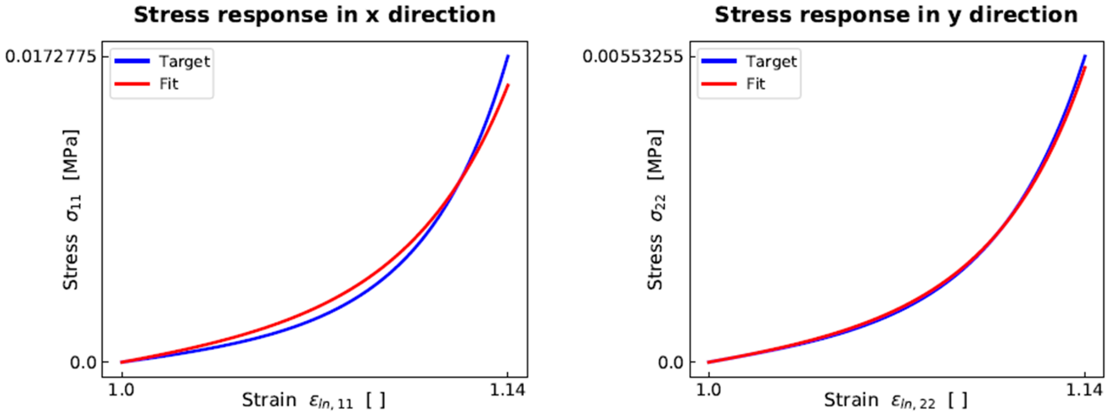

(a) Stress in x direction (11 entry)

(b) Stress in y direction (22 entry)

Figure 3.3: Stress-strain curve fitting results with optimized collagen volume fraction parameters from Table 3.1.

3.2.6 FE Model Setup

The bi-ventricular geometry was reconstructed from an in-house *ex vivo* cardiac MRI dataset. The geometry was mesh with 235625 tetrahedron elements. Idealized fiber orientation with helix angle varying transmurally from -60° at the epicardium to 60° at the endocardium was applied using a rule-based algorithm [9]. To account for the expansion constraint imposed by the surrounding tissues, the epicardium was subjected to a spring-like boundary condition with stiffness of 0.1 kPa/mm [98]. In the healthy condition, end-diastolic pressure of 4 $mmHg$ and 5 $mmHg$ were applied on to the endocardial surfaces of the RV and LV respectively. The basal nodes were fixed in the longitudinal direction and their radial and circumferential displacements are coupled to the two basal centroids of the left and right ventricular rings. To induce growth and remodeling, the LV pressure was further increase to 15 $mmHg$ to mimic the pressure overloaded condition.

3.2.7 Reverse Remodeling Simulation

To model reverse modeling induced by LVAD intervention, the overloaded LV pressure was simply reduced back to normal after certain time of growth. This mimics the pressure relief due to LVAD intervention. Using the same method, we created two *in silico* studies trying to answer two hypothetical questions: 1) Does implantation of the LVAD timing affect reverse remodeling? and 2) How do intrinsic growth parameters affect reverse remodeling? To look at LVAD implantation time effects, three cases (early, mid, and late LVAD implantation) were created by simply reducing the LV pressure at different time point of growth. To explore the second question, we investigate the effects on changing two parameters, myocyte growth rate and collagen growth rate, both of which were increased 25% from the baseline values.

3.3 Results

3.3.1 G&R under an increase of LV pre-load

The HCMM model was used to model myocardium G&R induced by increase of LV end-diastolic pressure (pre-load) in a bi-ventricular model (Figure 3.4 (a)). The changes of stresses in different constituents and wall thicknesses in different regions of the LV during the G&R process are shown in 3.4 (b) and (c), respectively. Stresses in both the myocyte and fiber direction (f) collagen successfully return to their homeostatic states after growth. Stresses of collagen in the sheetlet (s) and sheetlet-normal (n) directions significantly increase at the beginning of growth but eventually return below the homeostatic stress. Wall thickening is more significant at the apex than the free wall. In contrast, the septal wall thickness decreases at the end of growth. Figure 3.4 (d) shows the contour plots of normalized density change of different constituents after growth being stabilized. Locally, the growth of all constituents is localized around the endocardium. Density change profile of the myocyte has a similar pattern but higher magnitude than collagen (f). The collagen families in the orthogonal directions (s and n) have lower level of density change mainly concentrated at the septum and free-wall of the endocardium. Quantitatively, Figure 3.5 shows the changes of densities (growth) and remodeling stretches over time in the entire LV field. Both myocyte and collagen (f) average densities are increased by over 30%. The average densities of collagen (s) and (n) are slightly reduced by 16% and 8%, respectively. Remodeling stretches of myocyte and collagen (f) are both increased by around 5% while decreasing by around 1.5% for collagen (s) and (n). For all metrics, the standard deviation increase during the process of growth, indicating that the field becomes more inhomogeneous as G&R proceeds.

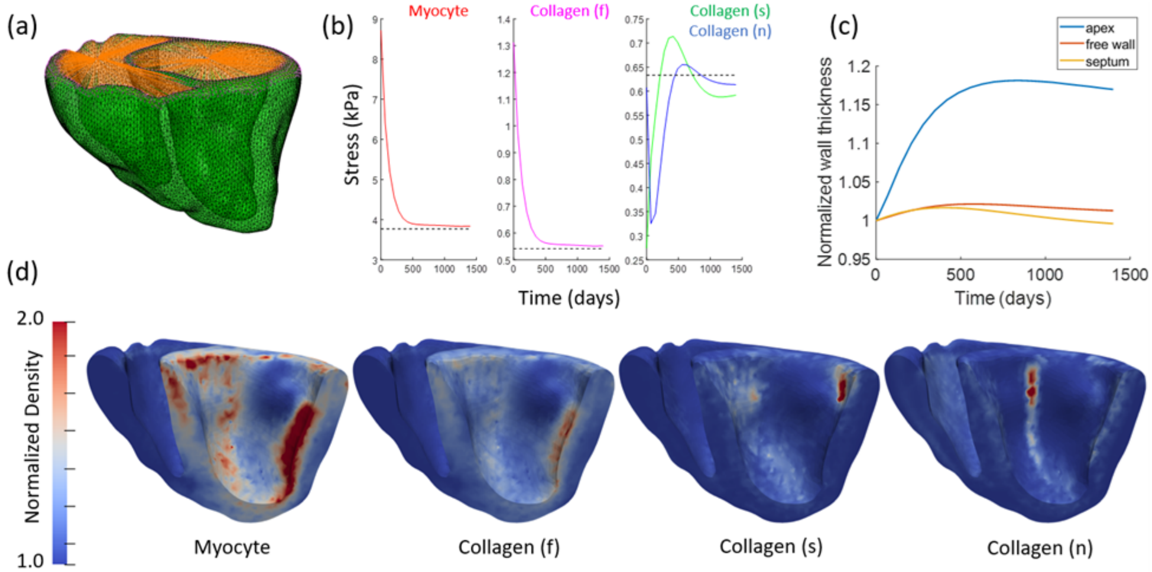

Figure 3.4: Simulation results of growth under increase of left ventricular (LV) pre-load. (a) A bi-ventricle finite element model; (b) plots of myocyte and different directional collagen stresses change during the process of G&R, dashed lines indicate the associated homeostatic stresses; (c) changes in wall thickness over time; (d) changes of densities in different constituents after growth.

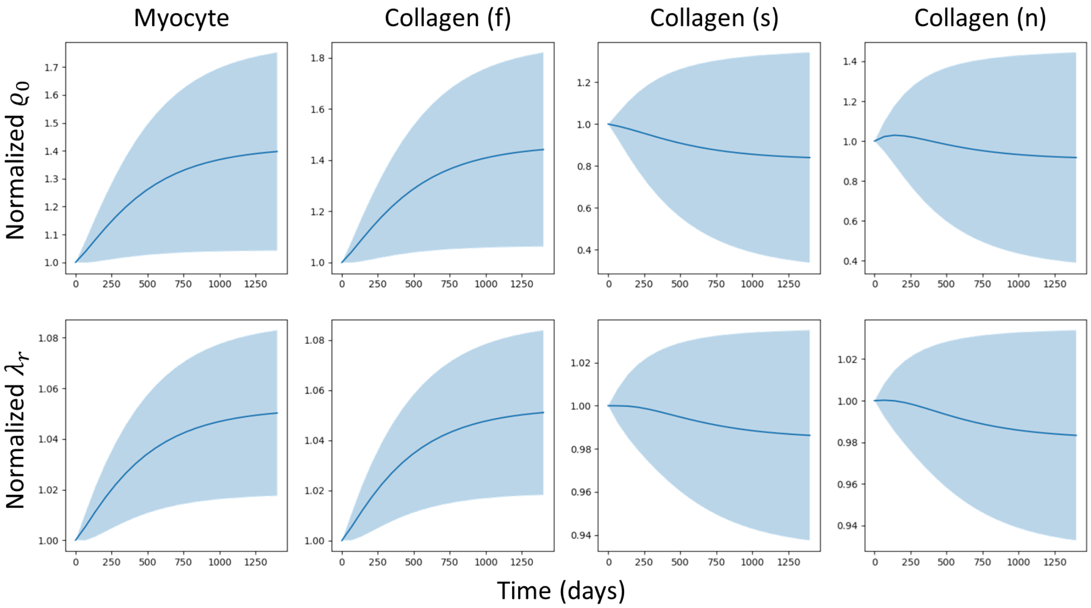

Figure 3.5: Quantitative results of growth and remodeling in different constituents under LV pressure overload. Each solid line represents the change of average density or stretch over the entire left ventricle during G&R. One standard deviation within the LV myocardium is shown as the shaded area indicating the variability of the field.

3.3.2 Parametric study

A parametric study was conducted to explore the effects of LV pre-load, myocyte growth rate, and collagen growth rate on the G&R behaviors of different constituents. By further increasing the LV pre-load from 15 $mmHg$ to 25 $mmHg$, the growth effects of most constituents are amplified as shown in Figure 3.6. All these metrics in the LV field become more inhomogeneous which led to a divergence of the simulation. Before the simulation reaches numerical issues, the average densities of myocyte and collagen (f) increase up to 75% while the atrophy of collagen (s) and (n) decrease. In fact, collagen (n) change from atrophy (reduce by 8%) to growth (increase by 3%). In terms of remodeling, myocyte and collagen (f) are further stretched by over 6% while collagen (s) and (n) shrink by over 3%.

By increasing the myocyte growth rate from 0.2 to 0.25 (Figure 3.7), the growth of average myocyte density increases from 40% to 47% while all collagen densities are slightly reduced (less than 5%). Myocyte and collagen (f) remodeling stretches are decreased while remodeling shrinking gets more severe in collagen (s) and (n). As shown in Figure 3.8, increasing the collagen growth rate from 0.2 to 0.25 manly increases the average density of collagen (f). Although average densities of collagen (s) and (n) remain the same, their field inhomogeneity increase. Remodeling across all four constituents remain similar comparing to the baseline.

3.3.3 Simulations of reverse remodeling

Reverse remodeling (RR) was simulated by remove the excessive LV pre-load which can be clinically achieved by implanting LVAD. As shown in Figure 3.9, myocyte density is reduced close to the healthy condition, with small growth effect remains at the endocardium, at the end of RR. Quantitatively, the average myocyte density remains 12% higher than the healthy condition.

Using this RR simulation, two hypothetical questions were explored. 1) How does LVAD

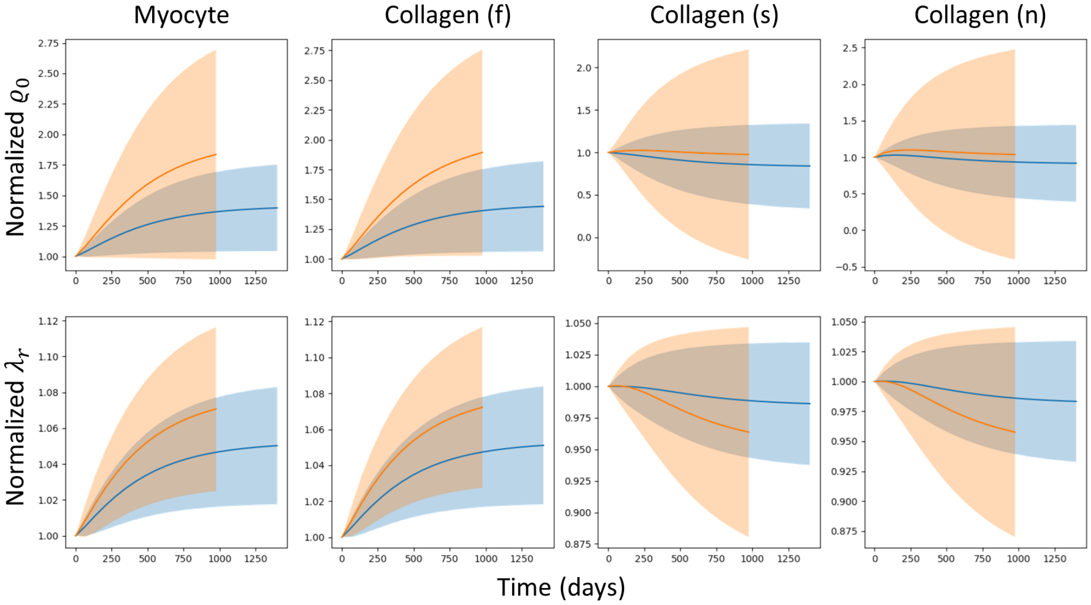

Figure 3.6: Effect of increasing LV overloaded pressure on growth and remodeling of different constituents. Blue curves represent the baseline case (15 $mmHg$) and orange curves represent the severe case (25 $mmHg$).

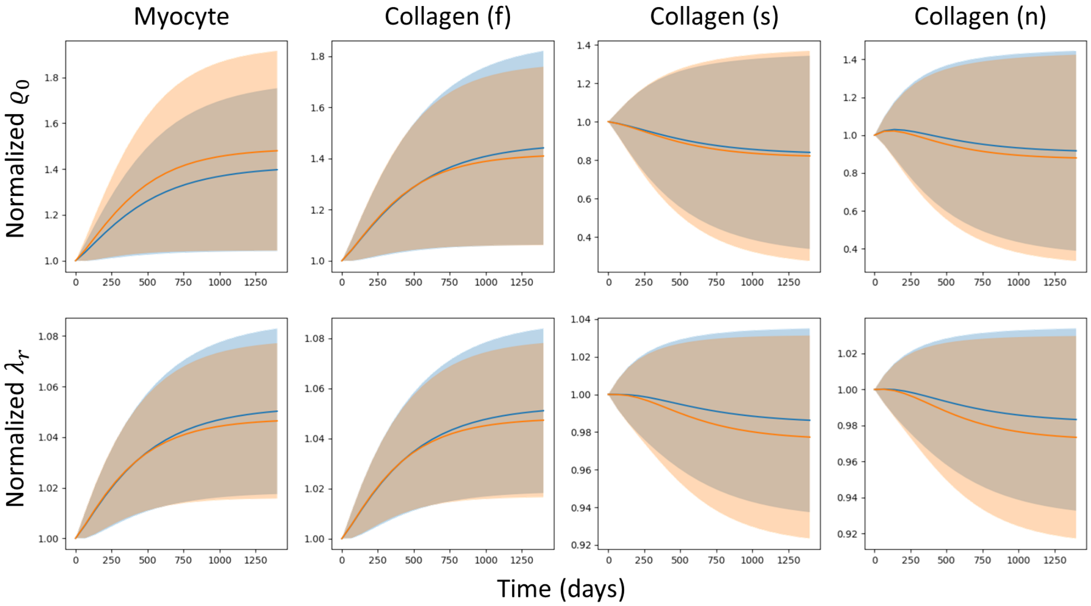

Figure 3.7: Effect of increasing the myocyte growth rate on growth and remodeling of different constituents. Myocyte growth rate is increased from 0.2 (blue) to 0.25 (orange).

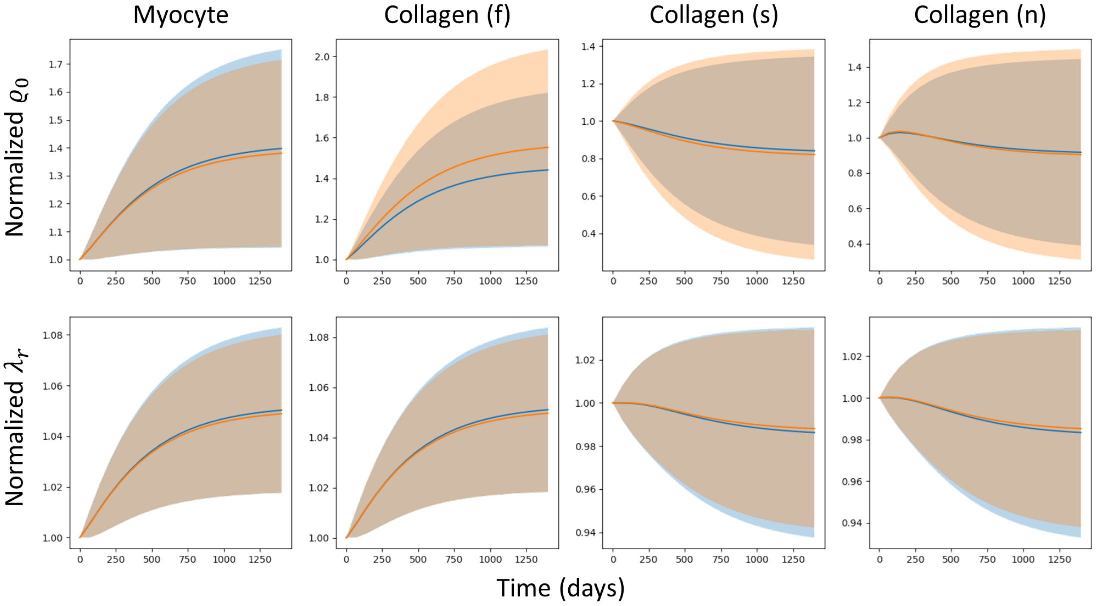

Figure 3.8: Effect of increasing the collagen growth rate on growth and remodeling of different constituents. Collagen growth rate is increased from 0.2 (blue) to 0.25 (orange).

implantation time effect RR? 2) How does the intrinsic growth rates effect RR? The result of LVAD implantation time effect is shown in Figure 3.10. Excessive pre-load was removed at three different time points, representing scenarios of early, mid, and late LVAD implantation. In general, the further we let growth continue without LVAD intervention the more inhomogeneous the fields of these constituents will become. Although all densities are decreasing during RR, they do not return back to normal. The level of inhomogeneity at the end of RR is directly related to how long this uncontrolled growth last. To look at G&R of each constituents, myocyte and collagen densities stay higher when uncontrolled growth last longer. RR changes the collagen (s) and collagen (n) from atrophy to growth but the densities are converged to similar level regardless of LVAD intervention time. Similarly, the remodeling stretch levels in myocyte and collagen (f) also reverse back to normal in all cases. In collagen (s) and (n) the remodeling stretch cannot fully recover back to normal. The later the LVAD intervention is introduced, the less recovery happens. Effects of increasing myocyte growth rate and collagen growth rate were investigated. According to Figure 3.11, with higher myocyte growth rate, all average densities remain similar to the baseline while the field inhomogeneity get severer in myocyte and collagen (s) at the end of RR. Remodeling stretches are also similar to baseline except of collagen (s) and (n) whose stretches are slightly reduced. With higher collagen growth rate (Figure 3.12), density field inhomogeneity of all families of collagen increase while the average values remain close to the baseline. There is no significant change of remodeling stretch in all constituents.

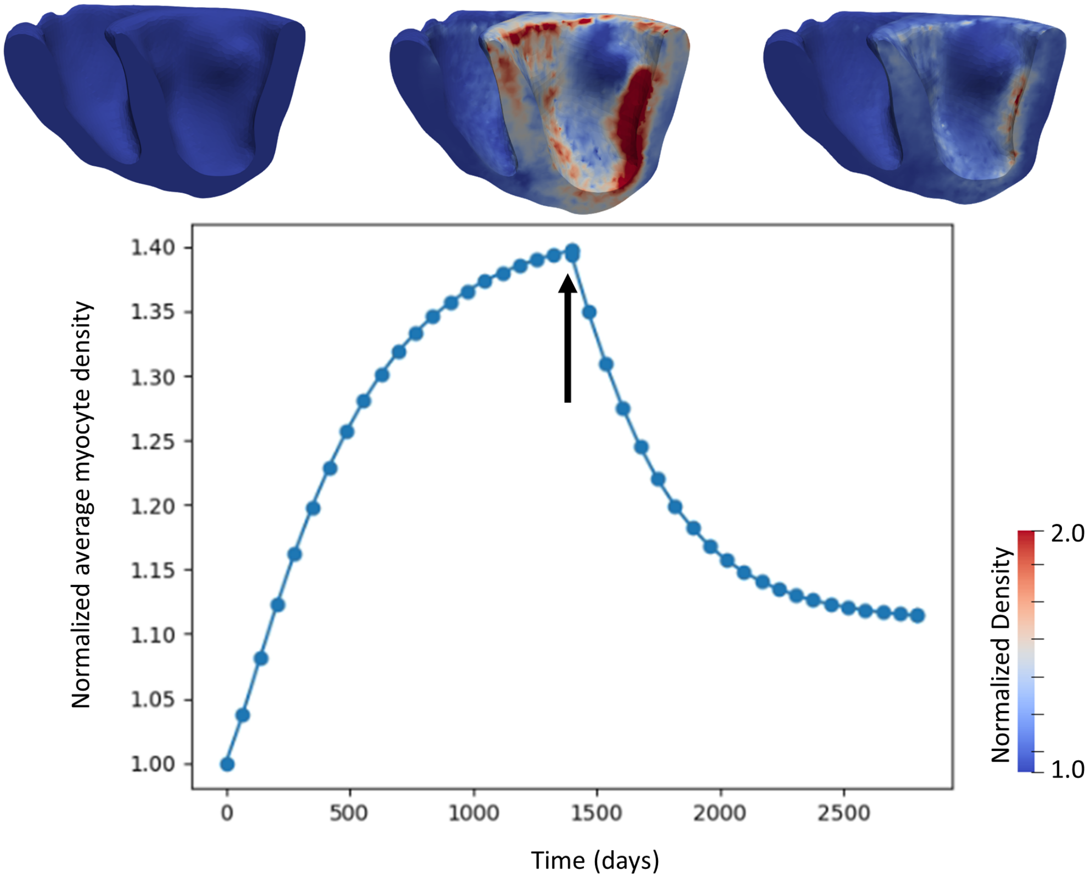

Figure 3.9: Results of reverse remodeling. The top contour plots represent normalized myocyte density before growth (left), after growth (middle), and after reverse remodeling (right). The black arrow in the average myocyte density graph indicates where LV pressure is reduced back to normal to trigger reverse remodeling.

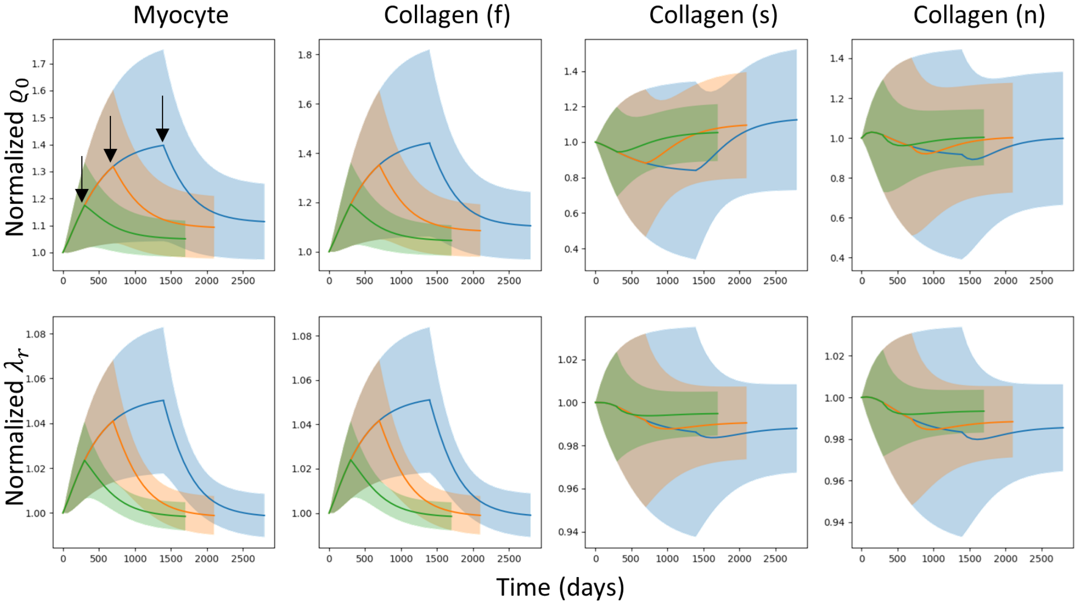

Figure 3.10: The effects of LVAD implantation time on reverse remodeling. Three cases, early (green), mid (orange), and late (blue) LVAD implantation, are compared. The black arrows in the top left figure indicates when the implantation is triggered.

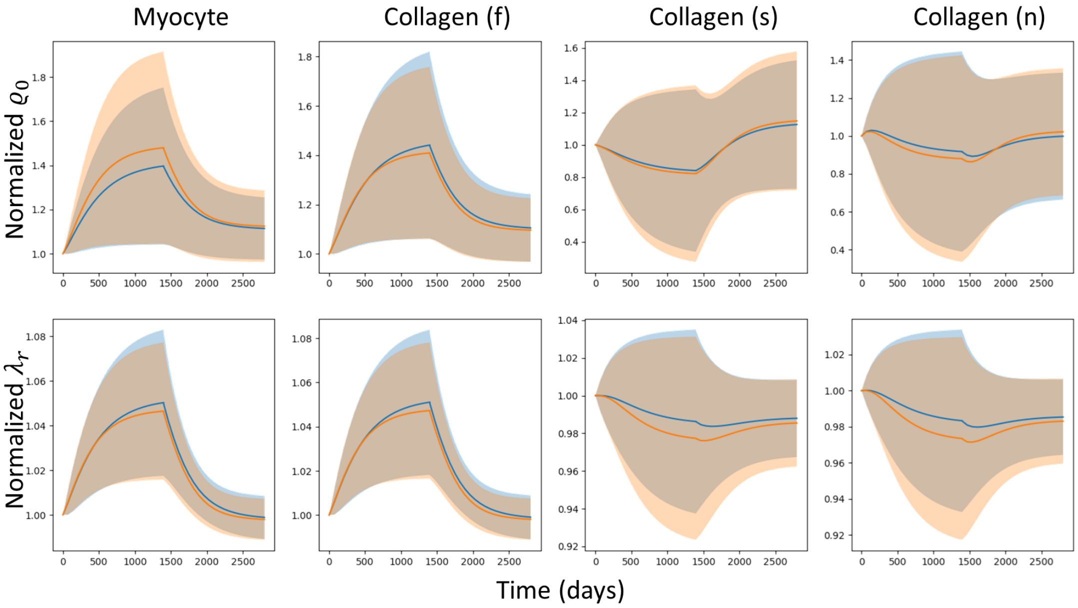

Figure 3.11: The effects of large myocyte growth rate on on reverse remodeling. Myocyte growth rate is increased from 0.2 (blue) to 0.25 (orange).

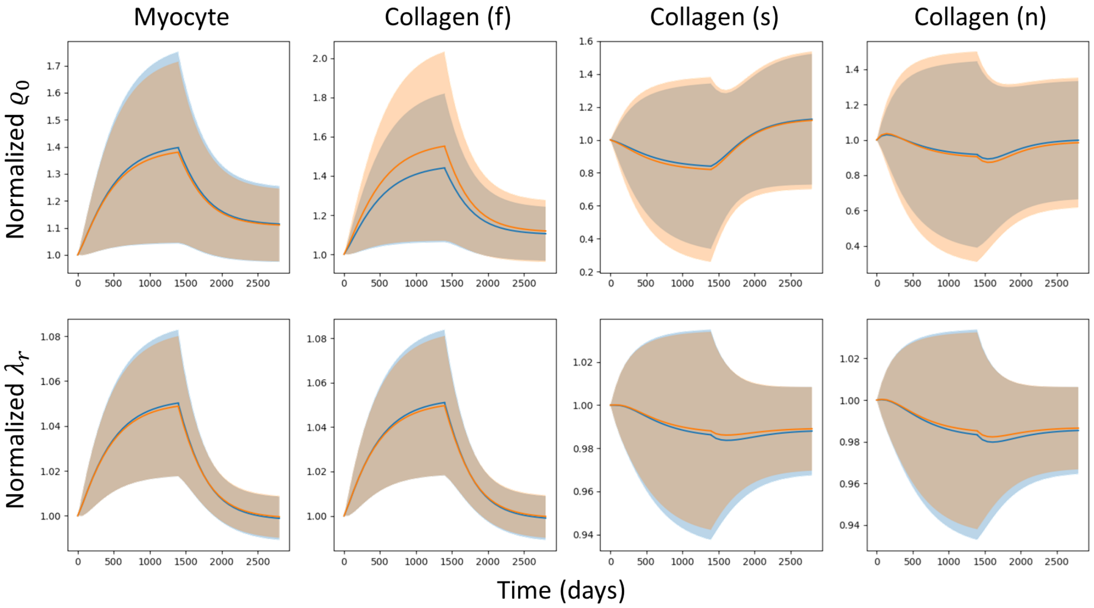

Figure 3.12: The effects of large collagen growth rate on on reverse remodeling. Collagen growth rate is increased from 0.2 (blue) to 0.25 (orange).

3.4 Discussion and Conclusion

In this work, we successfully used the homogenized constrained mixture model [15] to simulate cardiac G&R under increased LV pre-load. Through this multiscale approach, we were able to track the change of individual components of the myocardium (i.e. myocyte, collagen, and elastin) throughout the G&R process. The model was further extended to study reverse remodeling (RR) induced by LVAD intervention. The study showed that both the timing of LVAD intervention as well as innate growth properties significantly affect the RR outcomes of different constituents.

3.4.1 G&R under increase of pre-load

The bi-ventricular model successfully simulated G&R under an increase of pre-load. At the organ level, the simulation shows an increase in wall thickness which agrees with the pathophysiology of concentric hypertrophy under the pressure-overloaded condition [66].

Although the simulation provides the details of evolution of each constituent during G&R, the lack of experimental studies, especially in the context of myocardium G&R, limits our ability to validate the behavior at such a granular level. Through the parametric study, it becomes evident that increasing the level of growth triggers (e.g. pre-load) augments not only the level of G&R but also the field inhomogeneity, which could potentially lead to instability. In general, increasing the growth rate of one constituent reduces the level of G&R of the other constituents. The growth rate of myocyte has a stronger effect than that of collagen on G&R. An increase in the growth rate of myocyte significantly amplifies myocyte G&R and reduces G&R across all collagen families. Conversely, an increase in the growth rate of collagen primarily boosts the growth of collagen in the fiber direction.

3.4.2 Reverse Remodeling

There is emerging interest in studying reverse remodeling (RR) since it can provide guidance on therapeutic strategies. As a proof-of-concept study, we chose to simulate RR under LVAD implantation. Our *in silico* study reveals that prolonged uncontrolled growth diminishes the level of RR following LVAD intervention, a finding supported by a retrospective clinical study [117] that observed benefits from early LVAD intervention. The same study noted better RR responses in women, hinting at innate biological factors impacting RR. Although the current model cannot simulate the effects of gender differences, we explored the effects of innate growth properties on RR responses. Interestingly, our results show that the effects of increasing myocyte or collagen growth rate on G&R are counterbalanced during RR. Consequently, the final RR states remain similar compared to the baseline, regardless of these changes. Similar to how these two parameters affecting G&R, the myocyte growth rate exerts noticeable RR effects on myocyte and collagen (s) and (n), while the collagen growth rate mainly impacts the density of collagen (f).

3.4.3 Limitations and future work

The limitations of this work fall into three different areas: HCMM implementation, FE simulation, and model validation. It is crucial to discuss these limitations as they offer insights into potential avenues for future research.

HCMM implementation: In this study, the implementation of the HCMM closely followed the aortic G&R example [15], incorporating necessary modifications to the mechanical constitutive equations, collagen fiber orientations, and pre-stress algorithm to suit cardiac G&R specifics. While we adopted the stress-driven growth law following the example, the question of whether cell growth is indeed stress or strain-driven is a topic of ongoing debate [58], warranting the exploration of alternative growth laws in future studies. In addition, the direction of growth is currently defined explicitly in the transverse direction of the myocyte (Equation 3.16), assuming the volumetric growth happens as parallel sarcomerogenesis. Further implementation should include a general growth direction tensor to enable multidirectional growth as purpose in the aortic example [15]. Although the HCMM is much more efficient compared to the classical constrained mixture model, the simulations remain computationally intensive. For instance, the bi-ventricular model with 235k of tetrahedron elements requires 14.5 hours to run on a single CPU. Some aspects of the UMAT subroutine implementation can be further optimized to improve the computational efficiency. First, separating the pre-stress steps from the growth steps would allow for multiple growth scenarios to be tested without repeating pre-stress steps. This could be achieved by using two UMAT subroutines: a pre-stress UMAT and a growth UMAT. The pre-stress UMAT would calculate and output a file to record element-wise pre-stretch values, which the growth UMAT could then read for initialization. Second, the UMAT subroutine could benefit from utilizing predefined functions from the GNU Fortran compiler to avoid redundant computation. Third, enabling parallel execution of the HCMM UMAT using the Intel Fortran Math Kernel Library (MKL) would leverage the multiprocessing capabilities of Abaqus, potentially speeding up the process.

FE simulation: For the purpose of demonstrating the HCMM modeling capability, a number of simplifications were made in both the pressure overload simulation and the following RR simulation. For example, the pericardium spring-like boundary condition is defined with a constant stiffness. However, recent research, include our own study shown in Chapter 2, has shown that the pericardium boundary condition substantially influences both the phenotype and the level of growth [97, 35, 42]. Additionally, to avoid having extra active stress parameters, the end diastolic phase is chosen to define the homeostatic state, while the precise definition and understanding of this homeostatic state remains somewhat elusive. Similarly, RR simulations only modeled pressure unloading at the end-diastolic state, while in reality, patients with LVADs can experience reductions in both systolic and diastolic pressures and develop unique hemodynamic profiles [21, 62]. Therefore, dynamic simulations that model a full cardiac cycle should be used to account for these hemodynamic changes. In general, these FE simulation setups should be rigorously tested and defined to better represent and study the specific pathophysiology of G&R.

Model validation: We quantitatively show that both the pressure overloaded model and the RR model align with current understanding of cardiac G&R at the macroscale level. However, the evolution of microscale changes has not been validated due to the lack of experimental data on myocardium microstructure. To validate the model rigorously, it is essential to have experimental data at multiple levels, encompassing everything from the elastic and G&R properties of each constituent to the evolution of the microstructure. Significant efforts have been made to characterize constrained mixture growth parameters of the aorta [135], utilizing tension-controlled biaxial testing data [126]. A similar method could be employed to determine the parameters for the myocardium. However, challenges arise due to the more complex microstructure and three-dimensional geometry of the myocardium, compared to the planar geometry typically found in vessel walls. Consequently, multi-directional mechanical tests [55] are essential to properly determine the extensive set of material parameters specific to the myocardium. Turnover parameters, such as growth rate, will need to be ascertained based on longitudinal studies with animal models. Although many *in vivo* models have been developed to study chronic heart diseases [72, 112, 123, 90, 56], longitudinal information regarding different myocardium constituents is notably lacking, and the information varies widely between studies, as summarized in [88]. The collagen microstructure variations are even less reported [124]. Nevertheless, the advent of newer, more controllable animal models [99, 82], together with advanced microstructural imaging [96], holds promise for gathering more comprehensive and consistent G&R data, which will be critical for the development and validation of the myocardium HCMM.

In conclusion, we have demonstrated that the HCMM model can be used to simulate cardiac growth and remodeling as well as the reversal process. This type of *in silico* model can be used to rapidly test hypothetical G&R mechanisms as well as explore potential therapies for reversing G&R in chronic cardiac diseases. Validation of the model would require further experimental data to characterize the microstructural properties and the evolutionary behavior of the myocardium. Finally, this multiscale model can be further integrated with the inverse workflow described in Chapter 2 to achieve a more comprehensive quantification of patient-specific growth properties.

Chapter 4

Efficient patient-specific cardiac simulations using data-driven surrogate models

4.1 Introduction

Patient-specific models of biomechanics in cardiovascular medicine typically comprise computational models tailored to the unique anatomical and physiological characteristics of individual patients. Constructed through high-resolution medical imaging techniques such as Magnetic Resonance Imaging (MRI) or Computed Tomography (CT), these models employ computational methods and inverse analysis to accurately capture cardiovascular tissue properties and mechanical loads, enabling a comprehensive exploration of the intricate interactions between tissue mechanics, hemodynamics, and electrophysiology within the cardiovascular system [14]. The essence of inverse analysis lies in its ability to extract hidden information from observed data, such as determining the mechanical properties of tissues from their deformation and stress patterns [93, 133], making it a key component in the development of patient-specific models. Once generated, these patient-specific models can play a critical role in numerous medical applications, including improving the accuracy of diagnosis [132], facilitating the planning of treatments [20, 116], and potentially predicting the progression of cardiovascular diseases [34]. The ultimate goal of this approach is to inform and personalize treatment, further emphasizing the importance of patient specificity in cardiovascular medicine.

Developing patient-specific simulations for the cardiovascular systems presents significant computational challenges. The reliance on comprehensive physics simulations, such as finite element (FE) models, necessitates numerous iterative runs through inverse analysis to accurately determine personalized system parameters. This requirement for extensive computational resources forms a significant barrier to translating these promising technologies into routine clinical practice.

Several strategies have been explored to mitigate the extensive computational costs associated with patient-specific cardiovascular simulations. Notable strides have been made due to advancements in computing technology. A recent study successfully reduced the simulation time of a whole-heart model from days to a few hours using GPU acceleration [129]. Despite these impressive advancements, such a timeline remains prohibitive for routine applications in fast-paced clinical settings. Alternatively, other methodologies focus on augmenting the modeling framework itself to enhance computational efficiency. For instance, lumped parameter models (LPM) simplify the cardiovascular system into 0D models, significantly reducing the computational burden [41]. However, this approach risks sacrificing much of the individualized information that lends value to patient-specific simulations. Reduced-order modeling offers another route towards reduced computational load. This strategy employs a set of radial basis functions to project the full-dimensional model onto a lower-dimensional space, thus simplifying the computational task [11, 16]. More recently, data-driven modeling has emerged as a promising solution [29, 16, 78, 7]. This approach utilizes neural network-based surrogate models to learn and exploit the correlation between system parameters and output predictions, thereby bypassing the need for computationally expensive simulations.

In this work, we explore the potential of accelerating patient-specific cardiac simulation through the data-driven approach, harnessing the power of current deep learning techniques. Specifically, we develop a surrogate model utilizing a transformer-based architecture to predict left ventricle (LV) dynamics and global hemodynamics. We take a holistic approach, combining a customized automatic meshing tool with a robust FE model to generate a diverse dataset of dynamic LV simulations. The LV anatomies and dynamics in the dataset are further transformed into low-order representations via principal component analysis (PCA). The transformer-based model is then trained to predict dynamics within this reduced-dimensional space.

The surrogate model achieves improvement in speed of 4 orders of magnitude compared to the FE model, while maintaining an acceptable degree of accuracy. Given its efficiency, this surrogate model is ideally suited for carrying out inverse analyses, where it can replace the computationally demanding FE simulator as the forward model to expedite the identification of patient-specific parameters and the generation of patient-specific simulations.

I present the key methodologies in Section 4.2 including the creation of the LV simulation dataset as well as the details of the surrogate model. In Section 4.3, we compare the predictions of the surrogate model with the FE solutions in terms of 3D cardiac motion as well as clinically relevant metrics such as ejection fraction, systolic pressure, and diastolic pressure.

4.2 Materials and Methods

The proposed LV surrogate model uses transformer-based architecture to predict LV motion in a reduced order space, as illustrated in Figure 4.1. The success of this model hinges on the use of personalized LV meshes with consistent topology in building the FE simulation dataset. As detailed in Section 4.2.1, we developed a workflow to automatically

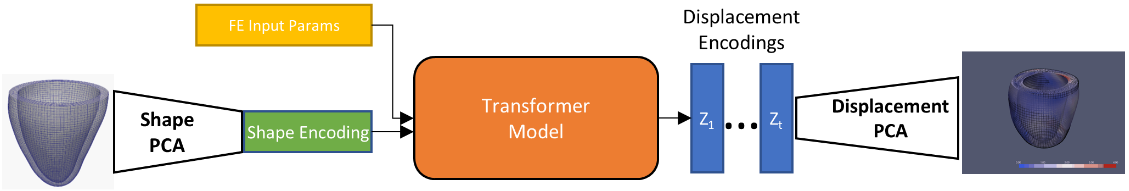

Figure 4.1: An overview of the LV surrogate model.

generate these meshes from segmented cardiac MRI data using elastic morphing. The FE model and the simulation dataset built upon this set of topologically consistent meshes are described in Section 4.2.2. We used principal component analysis (PCA) to create two reduced order models, a shape model and a displacement model, from the dataset. A LV reference (i.e. end-diastolic) geometry can be reconstructed from a shape latent vector using the shape model. Similar, a displacement filed can be recovered from a displacement latent vector using the displacement model. These two reduced order models are elaborated upon in Section 4.2.3. Lastly, the transformer-based model, which takes a shape latent vector and FE model parameters as inputs and autoregressively predicts a sequence of displacement latent vectors, is described in Section 4.2.4.

4.2.1 Automatic LV mesh reconstruction

The automated LV meshing workflow, depicted in Figure 4.2, includes two key steps. The first step extracts segmented cardiac MRI data to form the epicardial and endocardial surfaces of the LV. In particular, the epicardial and endocardial rings along with a LV centroid are extracted from each slice. One inherent characteristic of cine cardiac MRI is the misalignment between slices posing a challenge to 3D reconstruction [30]. To overcome this, multislice alignment is performed by shifting slices following a centroid-based cubic smoothing spline. This process allows the shifted epicardial and endocardial rings to form more realistic epicardial and endocardial surfaces, respectively, The same cubic spline approximation algorithm is used to further smooth the surfaces and reconstruct a realistic apex. The

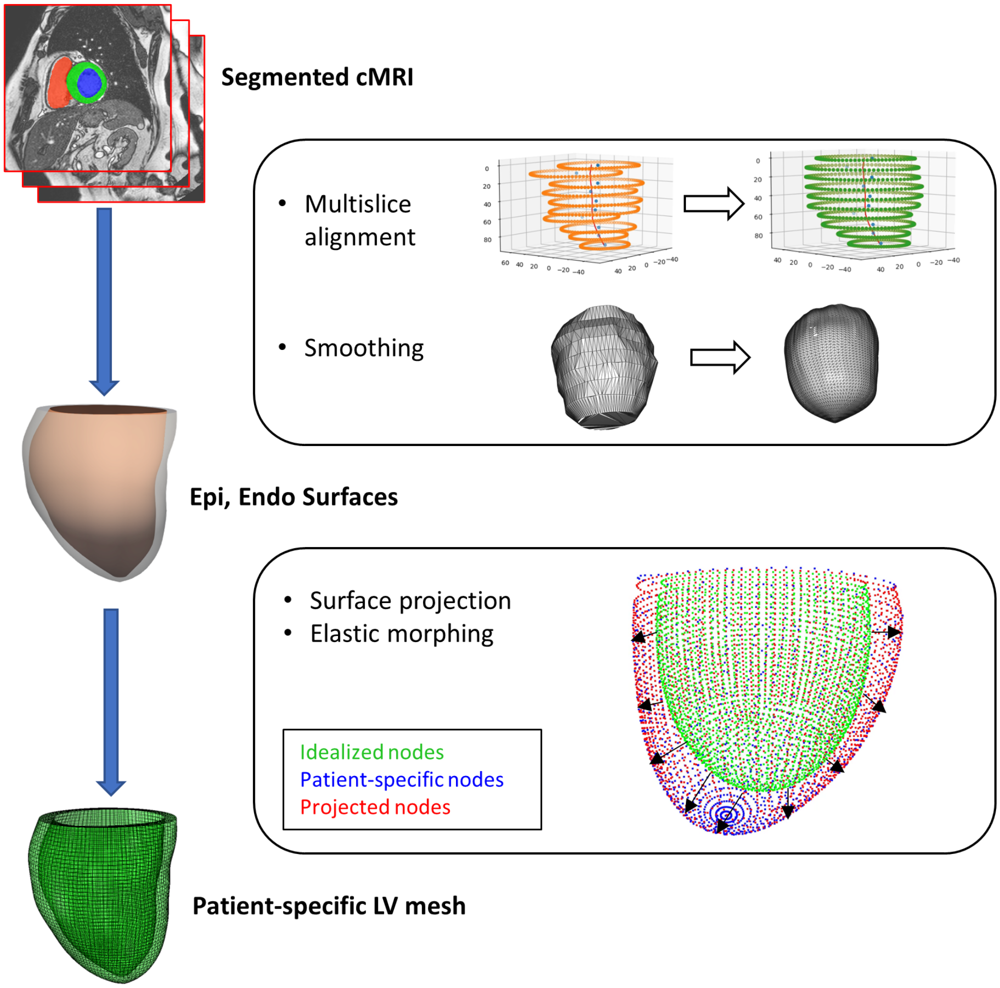

Figure 4.2: The workflow of automatic LV meshing. (Epi - epicardial, Endo - endocardial, cMRI - cardiac MRI.)

second step converts the epicardial and endocardial surfaces into a patient-specific LV mesh using an elastic morphing technique. Specifically, an idealized LV mesh (a truncated ellipsoid) with 23069 hexahedral elements is used. Nodes from the epicardial and endocardial surfaces are projected onto their corresponding patient-specific surfaces. These projection vectors are subsequently used as surface nodal displacements driving the idealized LV to elastically morph to the patient-specific geometry. The workflow was used to generate LV meshes from the M&Ms open dataset [19], which contains 290 sets of cine cardiac MRI with both left and right ventricles labeled at the end-diastolic phase.

4.2.2 Dynamic FE model

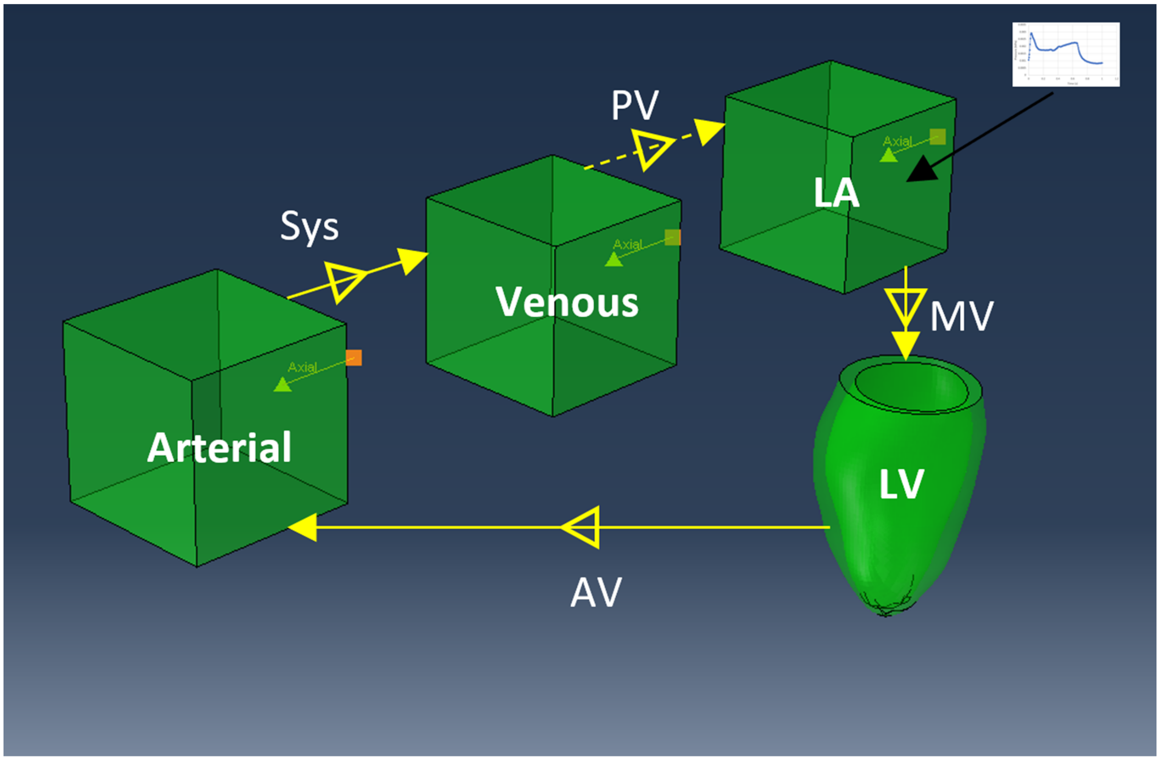

Figure 4.3: An overview of the dynamic LV model. (LV - left ventricle, LA - left atrium, AV - aortic vale, Sys - systemic resistance, PV - pulmonary valve, MV - mitral valve.)

The dynamic FE model was developed in Abaqus/Explicit [31]. It contains a high fidelity FE model of the LV coupled with an open-loop lumped parameter model (LPM) representing the circulatory system as shown in Figure 4.3. The LV model uses the patient-specific LV mesh assigned with an idealized fiber orientation (epicardial to endocardial helix angle varying from -60° to 60°) following our previous approach [35]. Similarly, the LV basal nodes are fixed in the long-axis while the radial and circumferential displacements are coupled to the basal centroid. The myocardium material model is adapted from the Dassault Systèmes Living Heart Human Model [139] where an incompressible Holzapfel-Ogden hyperelastic model (Equation 4.1) [55] is used for the passive behavior coupling with an active stress model (Equation 4.2) [49] for contraction during systole. The active stresses are added in both the fiber ($\mathbf{f}$) and normal ($\mathbf{s}$ and $\mathbf{n}$) directions as shown in Equation 4.4. The baseline material parameters inherent from [139] are summarized in Table 4.1. Prior to simulating the cardiac dynamics, a two-step pre-load procedure is conducted, where the end-diastolic pressure of 8 $mmHg$ is applied to the endocardial surface followed by a pre-stress process [43] to recover the MRI-reconstructed LV geometry under diastolic pressure loads. The LPM contains three compliance chambers and four unidirectional valves which are represented by the "fluid cavity" and "fluid exchange" modules in Abaqus, respectively. The pressure (P) and volume (V) relationship inside a Fluid Cavity chamber is governed by Equation 4.5 with a compliance property (κ). The flow (Q) between two chambers is governed by Equation 4.6 with a valve resistance (R). The total of 7 LPM parameters are summarized in Table 4.2. To couple the LV and the LPM models, the LV chamber is also defined as a fluid cavity chamber connecting with the atrium and arterial chambers through the mitral valve and aortic valve, respectively. The pressure in the LV fluid cavity chamber is applied to the endocardial surface of the LV model after the pre-load procedure. The time-varying pressure in the LA chamber is explicitly defined in order to mimic realistic atrial contraction during end-diastole. As shown in Figure 4.4, the model outputs motion, stress and strain fields of the LV as well as pressure and volume tracings of different chambers. In order to reduce the number of input variables in the LV model, the linear (a_i) and exponential (b_i) terms in Equation 4.1 are subject to uniform scaling by scalar multipliers c_a and c_b, respectively. In addition, all active parameters except for T_{max} are assumed to be constant across different patients. This results in a total of 10 input variables in the dynamic FE model. To further reduce the parameter space, a sensitivity analysis was conducted to investigate the impact of each variable on the pressure-volume loop of the LV. Each parameter was varied in increments between 0.25 to 2.5 times of its baseline value and the associated pressure-volume loop was evaluated. The sensitivity analysis further reduced the number of input variables into 6, which are c_a, c_b, T_{max}, κ_{AO}, R_{MV}, and R_{sys}.

This dynamic LV model with 6 input variables was employed to obtain a dataset of LV simulations. 275 patient-specific LV meshes were created from the M&M dataset [19] using the automated meshing workflow. 270 meshes were used twice to generate 540 patient-specific LV simulations where the input parameters were sampled via a Sobol sequence. Additionally, a test dataset (n=50) was created by using the surplus 5 LV meshes - each was applied with 10 extra sets of input variables produced by the Sobol sequence. To ensure convergence, the model was run for 4 cardiac cycles providing a total of 80 frames for each simulation.

$$\begin{aligned}\Psi = {} & \frac{a}{2b}exp(b(I_1^e - 3)) + \sum_{i=f,s} \frac{a_i}{2b_i}\{exp[b_i(I_{4i}^e - 1)^2] - 1\} + \frac{a_fs}{2b_fs}[exp(b_{fs}{I_{8fs}^e}^2) - 1] \\ & + \frac{1}{D}(\frac{J^2 - 1}{2} - ln(J))\end{aligned} \tag{4.1}$$

$$\sigma_a = \frac{T_{max}}{2}\frac{ca_0^2}{ca_0^2 + Eca_{50}^2}(1 - cos(\omega(t,l))) \tag{4.2}$$

where

$$
\begin{aligned}
&ECa_{50}(l) = \frac{(Ca_0)_{max}}{\sqrt{e^{B(l-l_0)}-1}} \\
&\omega(t,l) = \begin{cases} \pi\frac{t}{t_0} & t \in [0, t_0) \\ \pi\frac{t-t_0+t_r(l)}{t_r(l)} & t \in [t_0, t_0+t_r(l)) \\ 0 & t \in [t_0+t_r(l), \infty) \end{cases} \\
&t_r(l) = ml + b \\
&l(E_{ff}) = l_r\sqrt{2E_{ff}+1}
\end{aligned}
\tag{4.3}
$$

$$
\boldsymbol{\sigma} = \boldsymbol{\sigma}_p + \sigma_a \mathbf{f}\otimes\mathbf{f} + n_s\sigma_a(\mathbf{s}\otimes\mathbf{s}+\mathbf{n}\otimes\mathbf{n}) \tag{4.4}
$$

where $\boldsymbol{\sigma}_p = \frac{1}{J}\frac{\partial\Psi}{\partial\mathbf{F}}\mathbf{F}^T$ is the passive stress tensor.

passive	a [MPa]	b [ ]	a_f [MPa]	b_f [ ]	a_s [MPa]	b_s [ ]	a_fs [MPa]	b_fs [ ]	D [ ]
	3.94e-4	3.67	1.85e-3	14.38	1.05e-3	10.56	3.56e-7	7.82e-4	0.1
active	t_0 [s]	m [s/mm]	b [s]	l_0 [mm]	B [1/mm]	$(Ca_0)_{max}$ [$\mu mol/L$]	Ca_0 [$\mu mol/L$]	T_{max} [MPa]	n [ ]
	0.35	950	-1.5	1.58e-3	4750	4.35	4.35	0.2	0.35

Table 4.1: Baseline myocardium material parameters.

$$
V(t) = V(0) + \kappa P(t) \tag{4.5}
$$

$$
Q(t) = \dot{V} = \frac{1}{R}\dot{P} \tag{4.6}
$$

$1/\kappa_{AO}$	$1/\kappa_{LA}$	$1/\kappa_{VE}$	$1/R_{MV}$	$1/R_{AV}$	$1/R_{sys}$	$1/R_{PV}$
12.86	0.13	3.78	2.27	1.0	135.93	1.0

Table 4.2: Baseline LPM parameters. (In the Abaqus environment, $1/\kappa$ is the elasticity of a spring element that is attached to the fluid cavity chamber and it has the unit of ml/kPa. $1/R$ is the viscous coefficient of a fluid exchange element and it has the unit of $kPa\cdot ms/ml$)

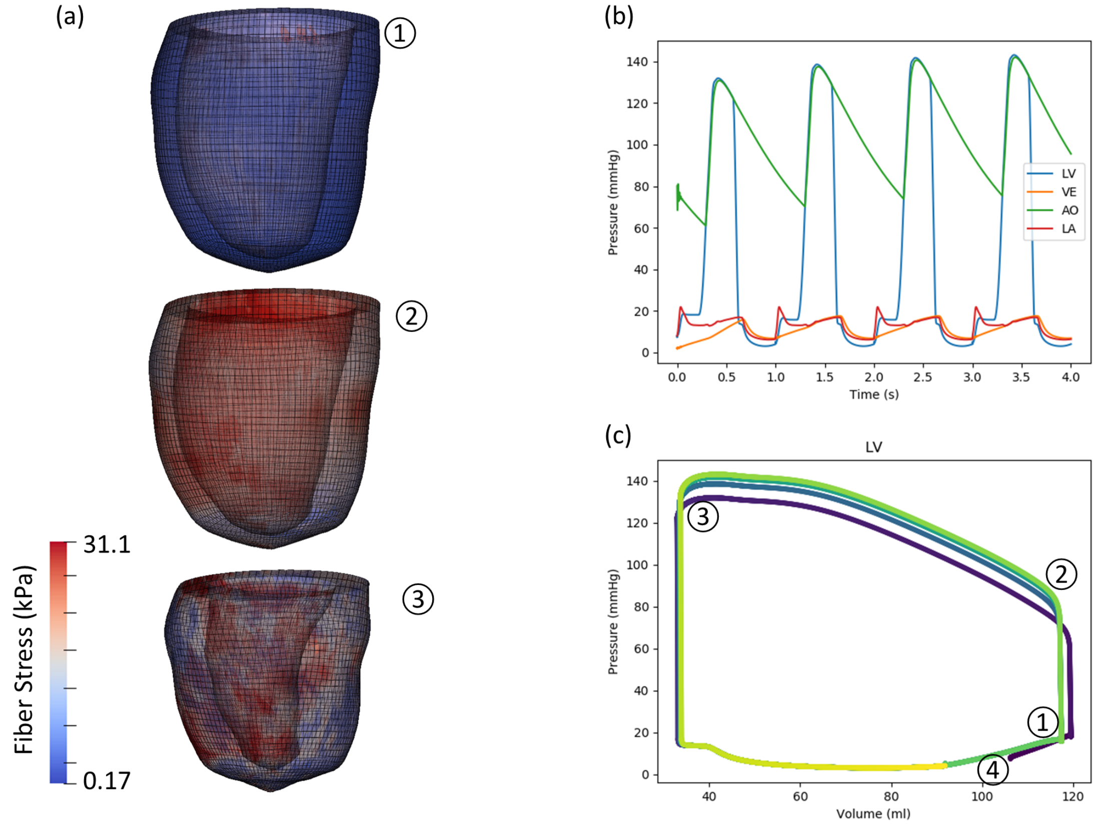

Figure 4.4: Outputs of the dynamic LV model. (a) Contour plots of LV fiber stress field at the ① end-diastolic, ② early-systolic, and ③ end-systolic stages. (b) Pressure tracings of the left ventricle (LV), aorta (AO), venous bed (VE), and left atrium (LA) over 4 cardiac cycles. (c) Pressure-volume (PV) loops of the LV over 4 cardiac cycles. The different cardiac phases associated with the contour plots in (a) are annotated. ④ indicates the start of the simulation which is the beginning of the end-diastolic stage before atrial kick.

4.2.3 Reduced order models of LV shape and displacement

Principal component analysis (PCA) was used to project the shape and displacement information onto lower dimensional spaces (also known as the latent space). In particular, the shape of an LV mesh, with 27161 nodes in 3 dimensions, can be represented by a row vector $\mathbf{y}_i \in \mathbb{R}^d$ where ($d = 27161 \times 3 = 81483$) and ($i = 1, 2, 3..., n$). Each shape vector was centered by the mean shape vector $\bar{\mathbf{y}}$ evaluated over all LV samples ($n = 270$), Equation 4.7. PCA [77] was used to find an orthogonal matrix $\mathbf{U} \in \mathbb{R}^{d \times m}$ such that the centered shape vector ($\hat{\mathbf{y}}_i$) can be projected to a lower dimensional latent vector ($\mathbf{s}_i \in \mathbb{R}^m$) as shown in Equation 4.8. The latent vector can be re-projected back to the full dimensional shape vector as shown in Equation 4.9. The same process was employed to the displacement fields where $\mathbf{y}_i$ is the flattened displacement vector and n is the number of simulations times the number of output frames per simulation ($n = 540 \times 80 = 43200$). For convenience, we denote the shape latent vector as $\mathbf{s}$ and displacement latent vector as $\mathbf{z}$.

$$\hat{\mathbf{y}}_i = \mathbf{y}_i - \bar{\mathbf{y}} \tag{4.7}$$

$$\mathbf{s}_i = \mathbf{U}^T \hat{\mathbf{y}}_i \tag{4.8}$$

$$\hat{\mathbf{y}}_i^* = \mathbf{U}\mathbf{s}_i \approx \hat{\mathbf{y}}_i \tag{4.9}$$

4.2.4 Transformer-based surrogate model

Inspired by a temporal attention architecture [50], this surrogate model is designed to take a conditional vector $\mathbf{I}$ (i.e. a set of LV model input variables) and a shape latent vector $\mathbf{s}$ as inputs and predict a sequence of displacement latent vectors ($\mathbf{z}_1$, ..., $\mathbf{z}_t$) autoregressively as depicted in Figure 4.5. Specifically, a Multi-Layer Perceptron (MLP) is used to encode the conditional vector into a state representation vector $\mathbf{c}$ that has the same length as $\mathbf{s}$ and $\mathbf{z}$. The three vectors $\mathbf{c}$, $\mathbf{s}$ and $\mathbf{z}$ are concatenated and linearly projected to an embedding dimension $d_m = 512$:

$$\mathbf{X} = concat(\mathbf{c}, \mathbf{s}, \mathbf{z}_1, ..., \mathbf{z}_{t-1})\mathbf{W}_1 + \mathbf{W}_1^b \tag{4.10}$$

A single layer transformer decoder [2], including a multi-head attention layer ($K = 4$ heads) and a feed forward layer, is applied to have output:

$$\mathbf{H} = transformer\_block(\mathbf{X}) \tag{4.11}$$

The last column of the output ($\mathbf{h}_{t-1}$) is linearly projected to become the following predicted displacement latent vector.

$$\mathbf{z}_t = \mathbf{h}_{t-1}\mathbf{W}_2 + \mathbf{W}_2^b \tag{4.12}$$

To enable predictions of LV pressure simultaneously, the scalar value is concatenated to both the shape and displacement latent vectors. The two latent vectors are selected to have the same size of 16 which results in a total of 3.2 M trainable parameters in this transformer-based model.

To train the model, the LV simulation dataset (n=540) was divided into 90% for training and 10% for validation. An extracted dataset (n=50) was used for testing. The model was trained incrementally [32], with a constant learning rate of 1e-6, and dropout rate of 0.1 in both the multi-head attention layer and the feed forward layer, to minimize the prediction loss as Equation 4.13. The model was evaluated on both the 3D LV dynamics as well as global LV pressure predictions.

$$Loss = \sum_{t=1}^{T} ||\tilde{\mathbf{z}}_t - \mathbf{z}_t||^2 \tag{4.13}$$

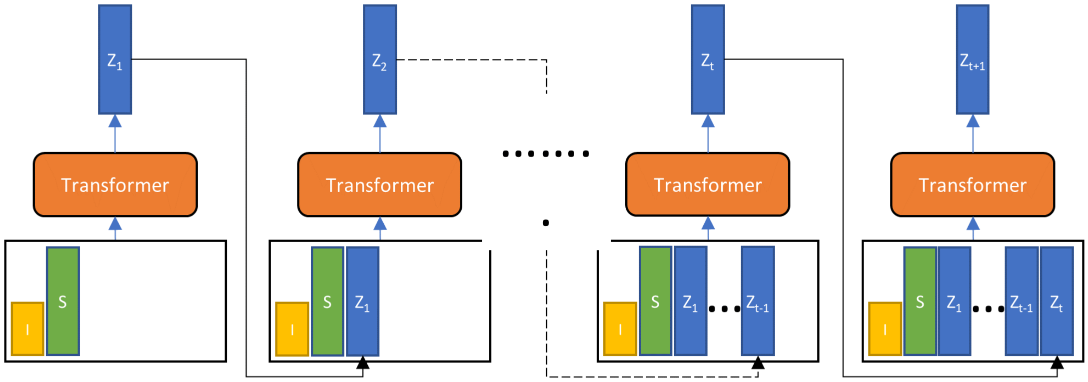

Figure 4.5: The autoregressive transformer model. I - FE parameter vector, S - shape latent vector, Z - displacement latent vector.

4.3 Results

4.3.1 LV simulation dataset

LV meshes: The automatic meshing tool successfully generated 286 out of 290 LV meshes from the M&M dataset [19] with averaged disc coefficient (DSC) of 89%. 11 meshes were further discarded due to thin wall or highly distorted apex. A subset of the LV meshes are shown in Figure 4.6, illustrating the diversity of the LV anatomies including healthy subjects and patients with hypertrophic and dilated cardiomyopathies.

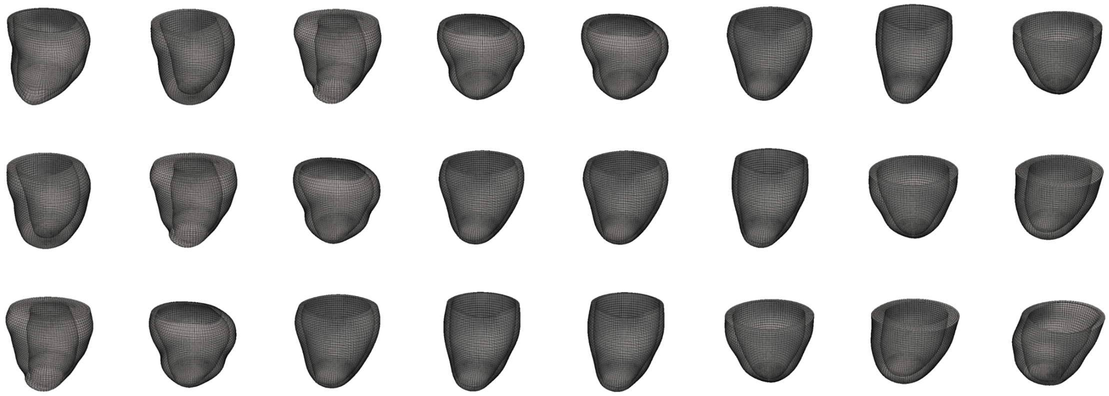

Figure 4.6: LV meshes with consistent topology.

Sensitivity analysis: The impacts of each of the 10 FE input parameters on the left ventricular PV loop are shown in Figure 4.7. We identified 6 out 10 influential parameters. They are stiffness (c_a, c_b) and contractility (T_{max}) of the LV as well as mitral valve resistance (R_{MV}), systemic resistance (R_{sys}) and aortic compliance (κ_{AO}). All the non-influential parameters are LPM variables that are peripheral to the LV.

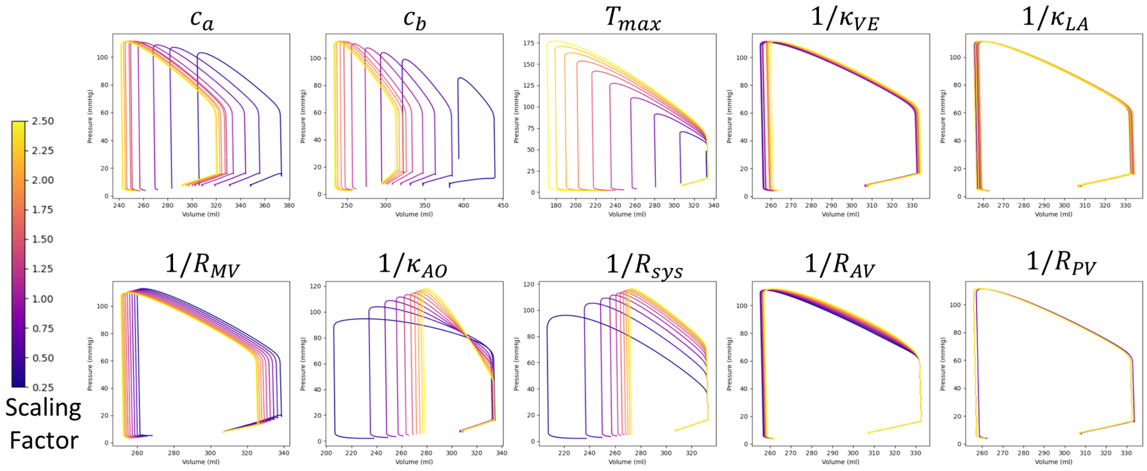

Figure 4.7: Results of a sensitivity analysis illustrating the impact of 10 different parameters on the LV pressure-volume loop. The left 3 columns represent the 6 influential parameters and the right 2 columns represent the 4 non-influential parameters.

4.3.2 LV surrogate model

Reduced order models: The shape model with 16 principal components (PCs) captures over 95% of variation within the 270 LV meshes. The average nodal displacement error is around 1.2 mm as shown Figure 4.8. Qualitative comparisons between the original LV meshes and the PCA reconstructed LV meshes are shown in Figure 4.9. Similarly, the displacement model also uses 16 PCs capturing well over 95% of variation within the 43,200 displacement frames with around 0.5 mm of average nodal displacement error, Figure 4.10. Based on the average nodal error, the 540 dynamic LV simulations are divided into three subsets, typical, intermediate, and atypical subsets, with error range of [0.22, 0.59], [0.59, 0.95], and [0.95, 1.32], respectively. The distribution of the three subsets are shown in Figure 4.11. The qualitative performance of the displacement PCA model is illustrated in Figure

4.12 where the median case in each subset is selected as the representation of the subset.

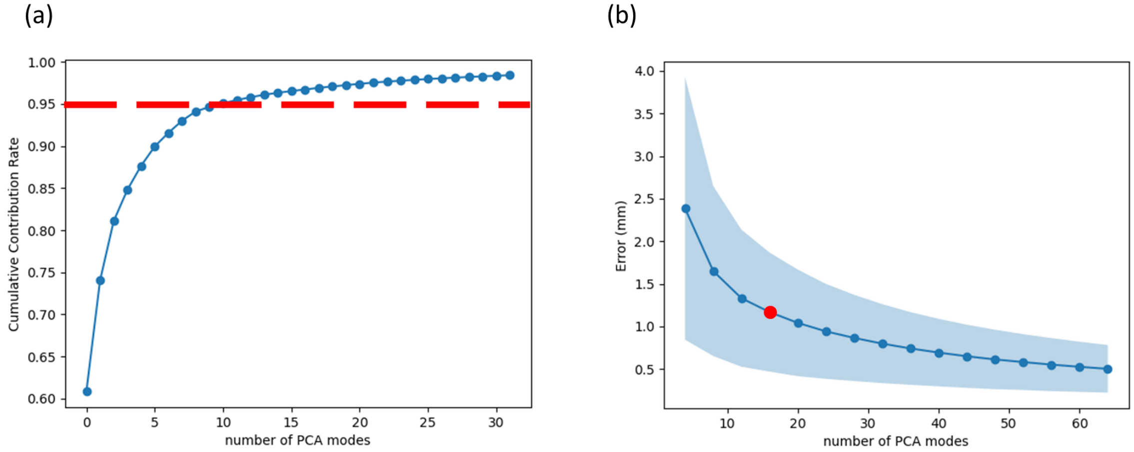

Figure 4.8: Quantitative evaluation of the shape PCA model with different number of principal components (PCs). (a) The cumulative contribution rate of 32 PCs. (b) The average nodal errors using 4 - 64 PCs. The red dot indicates the 16 PCs model which is selected in this study.

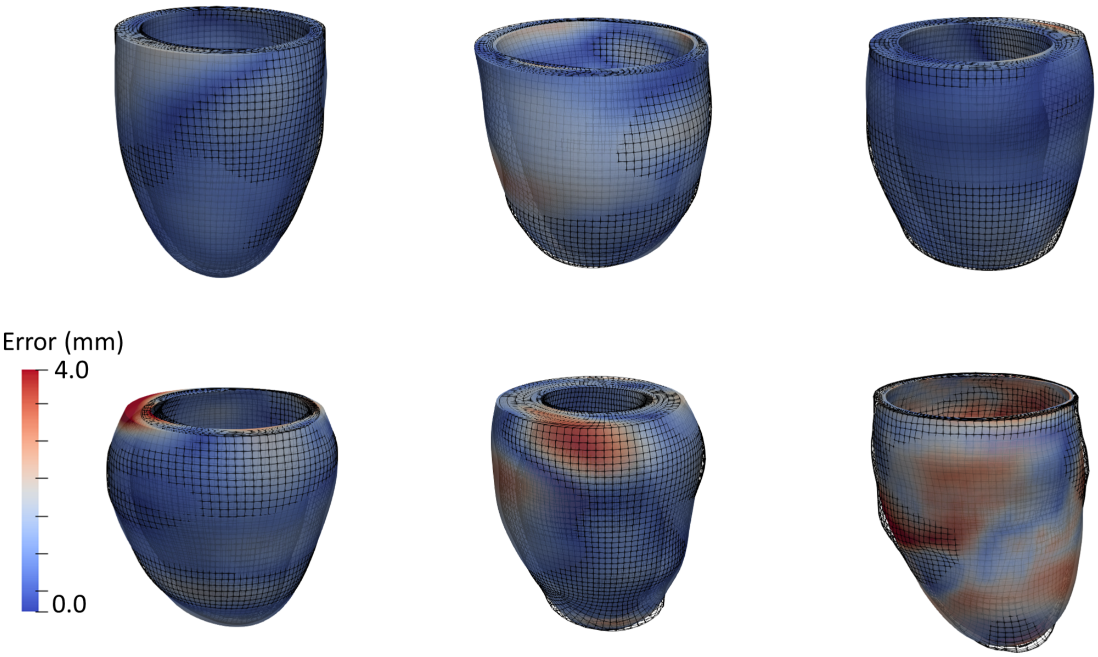

Figure 4.9: Qualitative comparison between the original LV meshes (wire-frames) and the PCA (PCs=16) reconstructed LV meshes (color contours). The color contour indicates the nodal error.

Transformer model: Figure 4.13 illustrates the error statistics associated with the

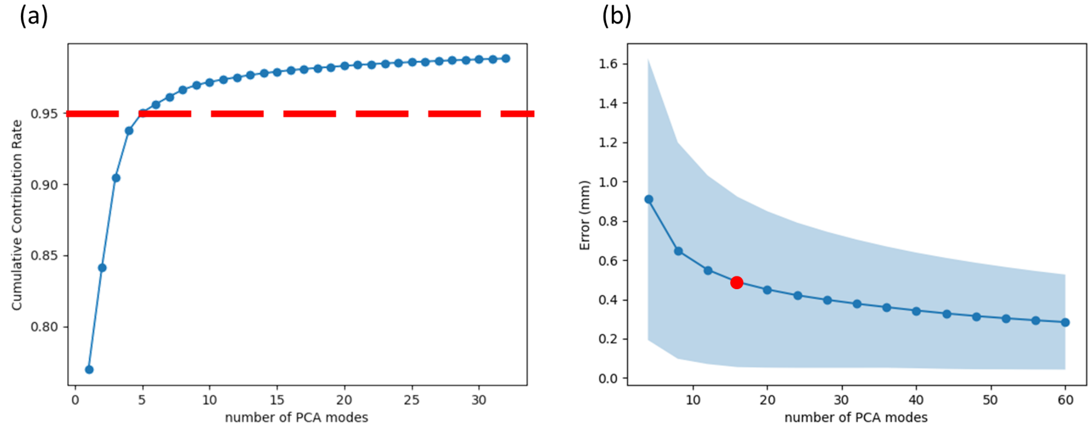

Figure 4.10: Quantitative evaluation of the displacement PCA model with different number of principal components (PCs). (a) The cumulative contribution rate of 32 PCs. (b) The average nodal errors using 4 - 64 PCs. The red dot indicates the 16 PCs model which is selected in this study.

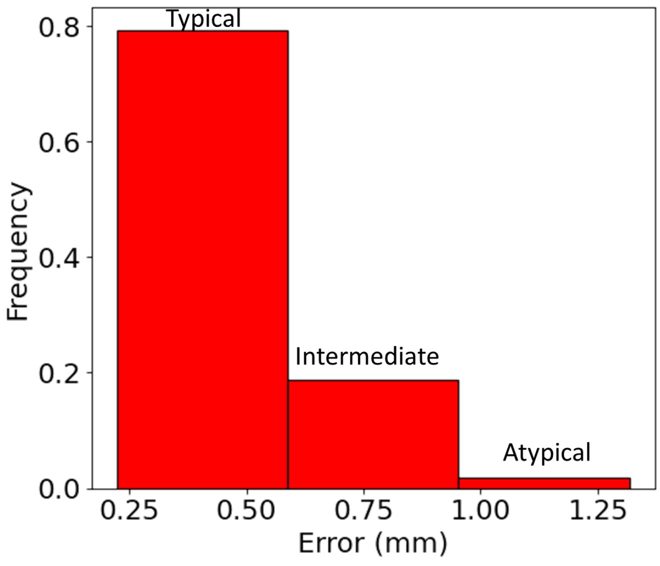

Figure 4.11: The average error distribution of PCA reconstructed LV displacements in the LV simulation dataset (n=540).

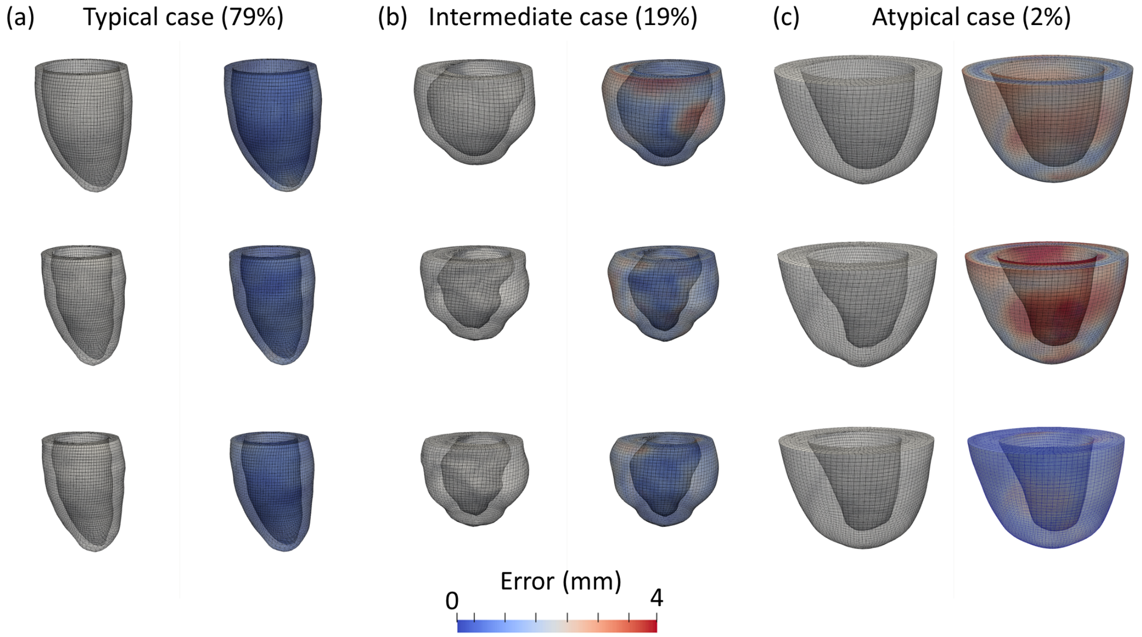

Figure 4.12: Qualitative comparison between the ground truth LV motion (white) and the PCA (PCs=16) reconstructed (color contour) LV motions within a cardiac cycle. The color contour indicates the nodal error. (a), (b) and (c) are the typical, intermediate and atypical cases, representing 79%, 19% and 2% of the cases in the LV simulation dataset (n=540), respectively.

3D dynamic predictions of the surrogate model with regard to the training, validation, and testing datasets. For each simulation, the average nodal error was calculated across the entire sequence. The mean and standard deviation of the average error for each dataset are shown. The model was trained to have prediction error of $0.81 \pm 0.20\,mm$ on the training dataset. When applied to the validation and testing sets, these error margins expanded to $1.3 \pm 0.53\,mm$ and $1.44 \pm 0.48\,mm$, respectively. Despite the increase, it is worth noting that the maximum average errors recorded in both the validation and testing sets remain below $3.5\,mm$, indicating reasonable predictive performance by the surrogate model. Considering the performance of the surrogate model is intrinsically constrained by the accuracy of the PCA model, as it predicts the 16 PCs of displacement instead of the actual displacement, reference error statistics derived from the displacement PCA model are also provided. PCA was conducted using the training and validation datasets; hence, the reprojection errors in the two datasets are similar, $(0.49 \pm 0.17\,mm)$ and $(0.48 \pm 0.16\,mm)$, respectively. This is also consistent with Figure 4.8 (b). The testing dataset, featuring previously unseen LV anatomies and dynamics, registered a slightly elevated error rate of $(0.58 \pm 0.2\,mm)$.

The error statistics of the global hemodynamics and cardiac function predictions on the validation and testing sets are shown in Figure 4.14, where the normalized errors of ejection fraction (EF), end-diastolic pressure (EDP), and peak systolic pressure (PSP) are calculated. In particular, the EF errors are 0.16 ± 0.23 (validation) and 0.12 ± 0.14 (testing), the EDP errors are 0.07 ± 0.56 and -0.13 ± 0.28 (testing), and the PSP errors are 0.05 ± 0.22 (validation) and 0.07 ± 0.21 (testing).

To further demonstrate the performance of the surrogate model, the test set is divided into three subset, typical, intermediate, and atypical subsets according to the average nodal error. The typical subset has an error range of [0.92, 1.68] mm including 74% of all test cases; the intermediate subset has an error range [1.68, 2.43] mm including 20% of all test cases; and the atypical subset has an error range of [2.43, 13.17] mm including 6% of all test cases. The predictions of the median case in each subset are analyzed in details. The nodal errors in the typical, intermediate, and atypical cases are $1.33 \pm 0.82\,mm$, $2.17 \pm 1.62\,mm$, and $2.88 \pm 2.10\,mm$, respectively. Figure 4.15 provides 3D visual representations of the ground truth (GT) and predicted (PD) LV shapes at the end-diastolic, mid-systolic, and end-systolic stages in the last cardiac cycle. The corresponding PV loop (four cardiac cycles) predictions are shown in Figure 4.16. In terms of the hemodynamic and cardiac function prediction, for the typical case, the EDP is 16.31 (GT) vs 15.89 (PD) $mmHg$, the PSP is 110.47 vs 107.47 $mmHg$, and the EF is 54.87% vs 58.66%; for the intermediate case, the EDP is 8.65 vs 4.29 $mmHg$, PSP is 107.76 vs 115.78 $mmHg$, and EF is 48.51% vs 46.30%; for the atypical case, the EDP is 16.00 vs 15.70 $mmHg$, PSP is 99.48 vs 143.81 $mmHg$, and EF is 44.06% vs 54.15%.

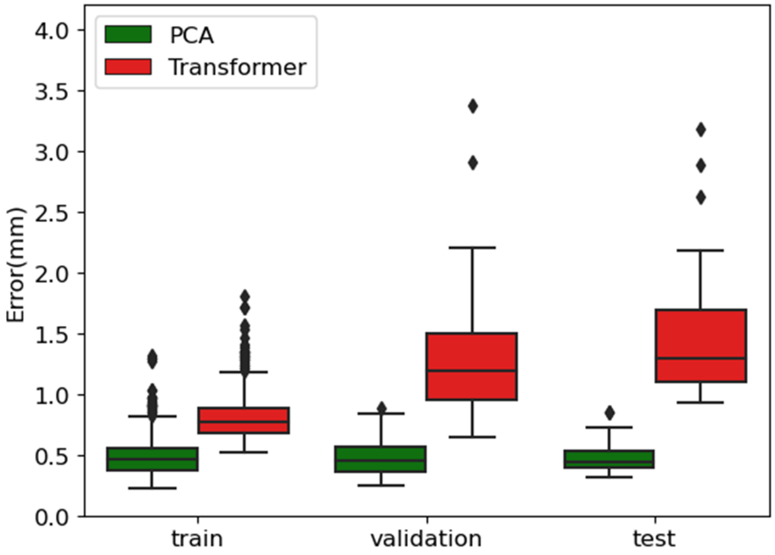

Figure 4.13: Average nodal errors of LV displacement comparing between the FE generated ground truth and the PCA reprojected approximations (red) or the transformer model predictions (blue). The errors are calculated on the training (n=486), validation (n=54), and testing (n=50) sets, showing as mean and standard deviation in the box-plot with outliers indicated by the dots in each column.

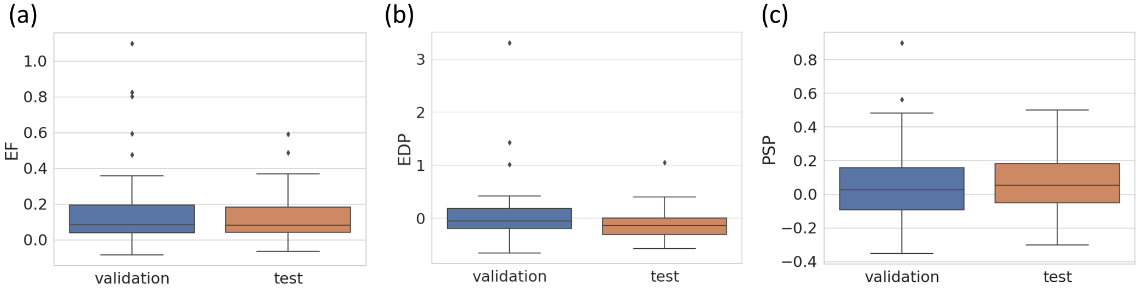

Figure 4.14: Normalized errors of hemodynamics and cardiac functions predicted by the surrogate model on validation and testing sets. (a) Ejection Fraction (EF), (b) End-Diastolic Pressure (EDP), (c) Peak Systolic Pressure (PSP).

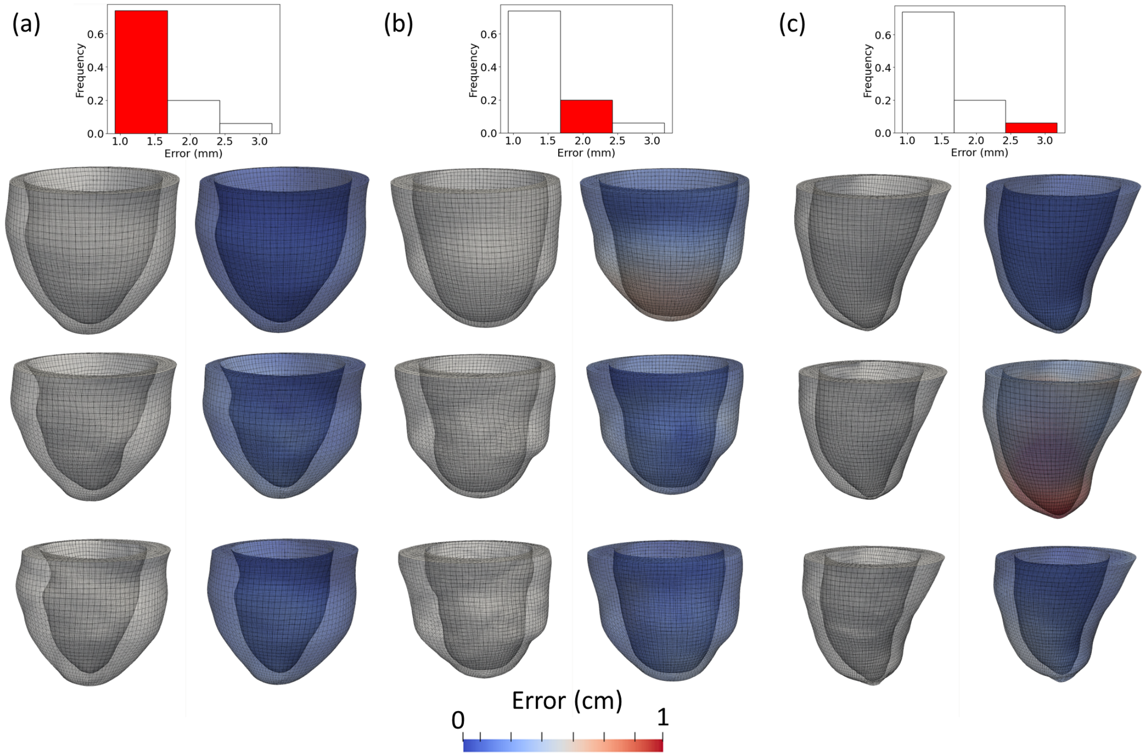

Figure 4.15: Qualitative comparison of the LV motion between the FE generated ground truth (white mesh) and the surrogate model predictions (colored mesh). (a), (b), and (c) represent typical, intermediate and atypical cases, respectively. The red bars in the top histogram plots indicate the proportion of these cases in the entire testing set. The shapes are generated from the last cardiac cycle at the end-diastolic (top row), mid-systolic (middle row), and end-systolic (bottom row) stages.

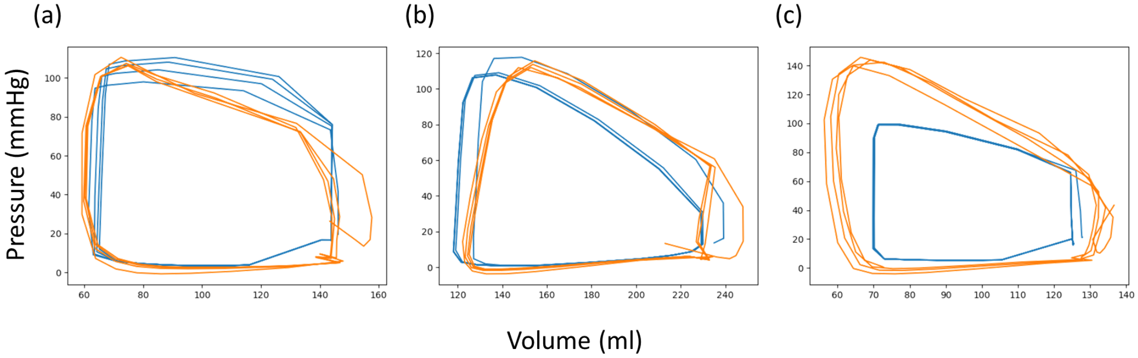

Figure 4.16: Comparisons of PV loops generated by the FE model (blue) and the surrogate model (orange). (a), (b), and (c) are the three cases corresponding to Figure 4.15.

4.4 Discussion and Conclusion

In this study, we took a multi-step approach to develop a data-driven surrogate model that can efficiently generate dynamic LV simulations. First, an automated meshing workflow was implemented to produce topologically consistent LV meshes from a segmented cardiac MRI dataset. These meshes were utilized by a dynamic FE model to produce an LV simulation dataset. The detailed LV shapes and dynamics from these simulations were then projected into lower-dimensional representations through PCA. Building on these advancements, a transformer-based model was trained to effectively predict LV 3D dynamics and global hemodynamics using these shape representation vectors and FE parameters as inputs.

The automated meshing tool exhibited a robust performance, successfully generating registered LV meshes from a diverse cohort of both healthy and diseased subjects [19], with a success rate of 98.6%. The diversity of the LV anatomies can be seen in Figure 4.6. Furthermore, the tool displayed a high degree of anatomical fidelity (DSC=89%), providing a reliable basis for further analysis. The robustness and accuracy of this tool were key for the successful implementation of the PCA models for dimensionality reduction.

The FE model coupling a high fidelity LV model with a LPM representing the cardiovascular circulatory system provides multi-dimensional information of the cardiovascular system as shown in Figure 4.4. The conducted sensitivity analysis proved to be an effective approach in reducing the design space of the FE model. Importantly, it preserved the diversity of the subsequently created LV simulation dataset, ensuring the representation of a wide range of LV hemodynamics as shown in Figure 4.7.

The PCA shape and displacement models demonstrated good representation of the anatomies and dynamics within the LV dataset. Specifically, both models captured well over 95% variation of the dataset with average reconstruction nodal errors of 1.4 mm and 0.6 mm in the shape PCA and displacement PCA, respectively. This illustrates the efficacy of PCA in transforming complex, high-dimensional data into low-dimensional representations while preserving critical aspects of the information. From a qualitative perspective, the shape PCA showed robust performance, as depicted in Figure 4.9, with larger errors usually observed at the large curvature areas such as the base or apex, or at regions of high waviness on the wall surface. Similarly, the displacement PCA model exhibited high accuracy in majority of the LV cases (79%) with nodal errors usually falling below 1 mm throughout the cardiac cycle as displayed in Figure 4.9 (a). However, certain challenges were encountered in a subset of cases (19%), particularly where the end-diastolic surfaces demonstrated substantial curvature and underwent significant twisting during systole, as indicated in Figure 4.9 (b). Furthermore, an outlier was noted in a case involving an extremely hypertrophic LV with large chamber volume and thick myocardium wall, as shown in Figure 4.9 (c). These observations highlight the nuanced performance of the PCA models across different LV regions and conditions.

The transformer-based model demonstrated promising results in predicting the 3D dynamics and global hemodynamics of the LV. For 3D shape predictions, the model achieved average errors of 1.3 mm on the validation set and 1.44 mm on the testing set. In terms of global hemodynamics, the model had a tendency to over-predict EF (16%), PSP (5%), and EDP (13%) in the validation set, with similar performance noted on the test set, except for under-prediction of EDP by 12%. Despite these discrepancies, the model showed a generally consistent performance on both the validation and testing sets, indicating its ability to be generalized to unseen LV anatomies and dynamics. Qualitative assessments showed that the predicted 3D dynamics closely approximated the ground truth on the majority of the test cases (74%) with average nodal errors less then 1.7 *mm*. Other cases with larger local nodal errors up to 10 *mm* usually occurred with out-of-phase predictions. For example, the case in Figure 4.15 (b) predicted a cardiac cycle slightly shorter than the ground truth which results in a noticeable advance of the systolic phase in the last cycle. On the contrary, the predicted cardiac cycle in Figure 4.15 (c) is slightly longer, leading to a delay of the systolic phase. As shown in Figure 4.16, the PV loop performances are in general more forgiving. Despite 3D dynamics of the intermediate case being predicted out of phase, the PV loop prediction is still close to the ground truth. Only the atypical case has significant over-predictions on both EF and ESP. Overall, this level of performance illustrates the potential applicability of the model for simulating LV dynamics and hemodynamics.

Notably, the surrogate model demonstrates substantial efficiency benefits over the original FE model. Whereas the FE model requires approximately 6 hours of processing on a 16-core CPU, the surrogate model performs inference in less than 0.5 seconds on a Nvidia Volta V100 GPU. This is a dramatic increase in speed without sacrificing substantial accuracy. Furthermore, the model showcases scalability, as it can be effectively parallelized with minimal speed reduction (e.g. generating 100 simulations in the same GPU takes less than 12 seconds). This quality is particularly beneficial for inverse studies, where multiple simulations are often needed, thus underscoring the surrogate model's practical utility in time-sensitive applications.

An increasing number of data-driven surrogate models are being developed for LV mechanical simulations, signifying the growing recognition of the value these models provide. Many of these models focus exclusively on the end-diastolic phase [28, 18] or the diastolic filling process [78], given their use in passive myocardium stiffness estimation. There are also efforts to develop surrogate models that learn from electro-mechanical simulations to predict global heart hemodynamics [107]. Our model advances the field by providing estimations of 3D dynamics over the full cardiac cycle, including both diastolic and systolic phases, and global hemodynamics. Compared to other published work [16], our model offers improvements in terms of speed and versatility. It does not require re-training for new LV anatomies, significantly expediting the inference process. Furthermore, our model conditions on a broader parameter space, considering not only contractility but also myocardium stiffness, and other circulatory system parameters. This allows for the characterization of a wider range of patient-specific cardiovascular parameters, enhancing the clinical utility of our surrogate model.

4.4.1 Limitations

The work conducted has certain limitations which also highlight areas for future potential. First, the current meshing workflow is only compatible with segmented MRI data, a relatively rare resource. An avenue for improvement could involve coupling the workflow with automatic segmentation tools such as UNET [109], as adopted by Buoso et al. [16], to generate meshes from unlabeled MRI data, which is far more common. This would enable the creation of a much larger and diverse dataset of LV meshes. Secondly, in order to control computational cost in generating the simulation dataset, the LV model employed is somewhat simplified, lacking aspects such as electrophysiology, pericardial boundary conditions, and mechanical interactions with the right ventricle. In future studies, fully electro-fluid-mechanical coupled whole heart models [113, 129] can be adopted to build a more accurate simulation dataset, thus better representing the heart dynamics. In terms of the surrogate model, this study serves as a proof of concept and did not involve thorough exploration of hyperparameter tuning. While the current number of principal components (PCs) sufficiently represents the dataset, it is conceivable that fewer PCs might be used to reduce training time without significant compromise on accuracy. Additional hyperparameter tuning in the transformer model could further enhance performance. Moreover, while the FE model has other field outputs such as stress, these are currently not predicted by the surrogate model.

By creating another PCA for each specific field output and concatenating those PCA latent vectors to the displacement latent vector, these field outputs could potentially be included in future iterations of the model. Lastly, the surrogate model is not physically bounded, which occasionally results in unrealistic predictions such as negative pressure or myocardium stiffness. Incorporating physical constraints, similar to the approach of Buoso et al. [16], could potentially rectify this issue and make the model more suitable for parameter identification.

4.4.2 Conclusion

In this work, we have introduced a unique surrogate model capable of simulating LV dynamics and hemodynamics. The method is anchored in a combination of an automated meshing workflow, a dynamic FE model, and PCA-driven dimensionality reduction. This framework has enabled us to train a transformer-based model that predicts the dynamics of the entire cardiac cycle and global hemodynamics efficiently, addressing certain limitations in existing studies. Despite its own limitations, such as reliance on segmented MRI data and a simplified LV model, this study offers a strong foundation for future enhancements and broader applications. The demonstrated potential for model parallelization and the rapid inference time suggest valuable implications for clinical applications, particularly in inverse studies. In summary, this study provides a compelling proof of concept for using data-driven surrogate models to facilitate efficient generation of patient-specific LV simulations.

Chapter 5

Conclusion and future work

In this thesis, I described the development of advanced simulation tools to study the biomechanics of cardiac growth and remodeling (G&R). First, I developed a growth characterization workflow to quantify tissue-level growth properties from cardiac MRI. Recognizing two main limitations in the workflow - the simplification of the growth theory and the computationally demanding nature of the finite element model, I addressed them by implementing a multiscale model that enables a detailed microstructure growth analysis, and by developing a data-driven surrogate model that substantially improves efficiency of patient-specific modeling. In this chapter, I will summarize the key contributions and novel insights provided by my doctoral work in Section 5.1, discuss some of the limitations and challenges encountered in Section 5.2, and present an outlook on potential future avenues in Section 5.3.

5.1 Summary and contributions

In **Chapter 1**, I introduced the basic pathophysiology of cardiac growth and remodeling, highlighting the clinical importance of understanding these mechanisms. Furthermore, I summarized the recent experimental and computational efforts towards studying cardiac G&R. Finally, I reviewed the applications of patient-specific simulations in the field of cardiovascular medicine.

In **Chapter 2**, I introduced a simulation workflow that combines *in vivo* cardiac MRI (cMRI), finite element (FE) analysis, and Bayesian optimization (BO) to non-invasively quantify myocardium growth properties. By inputting pre- and post-growth cMRI of the same subject, the workflow can characterize two parameters representing the levels of transverse and longitudinal microstructural growth. The patient-specific simulation, which uses the heart geometry from cMRI and the characterized growth parameters, serves as a growth digital twin of the subject. I employed the workflow to evaluate porcine heart growth due to exercise stimulation. I demonstrated that growth in the longitudinal direction of the cells dominates growth across all subjects, which aligns with our current physiological understanding. This framework establishes a platform for investigating myocardial growth at the tissue level using existing clinical data. It also highlights two bottlenecks in the process: 1) the inability to simulate microstructural remodeling, and 2) the extensive computational resources required for finite element simulations, limiting their immediate applicability in time-sensitive clinical scenarios.

In **Chapter 3**, we addressed the first limitation by using a microstructurally motivated theory, the constrained mixture growth theory, to develop multiscale models of cardiac G&R. We implemented the homogenized constrained mixture growth model as a user material subroutine in Abaqus. I demonstrated the capability of using the model to simulate growth induced by an increase of LV preload on a bi-ventricular model. By using this method, G&R of different components in the myocardium (i.e. myocyte, collagen, and elastin) can be tracked individually, providing an opportunity to validate existing experimental data and connect the findings from cellular to organ levels. I further used the model to simulate reverse remodeling induced by left ventricular assist device (LVAD) intervention. The study showed that reverse remodeling benefits from early intervention which agrees with retrospective findings from a clinical study. Potentially, this multiscale model can be integrated with the inverse workflow in Chapter 2 to achieve a more comprehensive quantification of patient-specific growth properties.

In **Chapter 4**, I focused on overcoming the second bottleneck by building a data-driven surrogate model of the LV. I developed an automated meshing tool to create a diverse dataset of registered LV meshes. These meshes were subsequently used in a robust dynamic FE model to generate a dataset of LV simulations. By conducting principal component analysis (PCA), I transformed the LV anatomies and dynamics in the dataset into low-order representations. I then trained a transformer-based model to predict dynamics within this reduced-dimensional space. The model is capable of predicting motion and pressure of the LV at a speed 4 orders of magnitude faster than the conventional FE model, rendering the surrogate model highly suitable for inverse analyses and significantly enhancing the efficiency of patient-specific simulation frameworks.

5.2 Limitations of this thesis

Despite the successful development of the growth characterization workflow, multiscale growth model, and surrogate modeling method, these tools have not been fully integrated within this thesis. The challenge stems from the limitations in each of these tools as discussed in previous chapters. To provide a comprehensive overview of the limitations hindering the creation of multiscale, patient-specific growth simulations for clinical practice, I will summarize them within three distinct areas: experimental data, image processing, and computational cost.

Experimental Data: We are currently lacking substantial growth data to construct and validate the models. The workflow in Chapter 2 was tested on a small dataset (n=4). Although the results qualitatively align with our current physiological understanding, we lack quantitative data (e.g., myocyte size measured from biopsy) for comparison with the workflow characterization results. The absence of biopsy data to extract microstructural information also restricts validation of the HCMM model described in Chapter 3. Despite attempts to collect *in vivo* biopsy samples, inconsistencies and challenges in maintaining the animal model have hindered the extraction of useful microstructural information. Consequently, improved protocols and imaging methodologies are necessary to acquire microstructural data for model validation.

Image Processing: The MRI data in Chapter 2 was manually segmented and reconstructed to obtain the LV meshes, which extends the time required for the growth characterization process. This approach would not be feasible when dealing with a large volume of imaging data. Although we developed an automated meshing tool in Chapter 4, it requires segmented MRI data as input. To address the needs of future large-scale processing, the incorporation of existing machine learning-based automated segmentation tools [10] into the pipeline could provide a viable solution.

Computational Cost: High computational demand is a shared characteristic of all the FE simulations in this thesis, ranging from 2-3 hours (kinematic growth simulation) to over 14 hours (HCMM bi-ventricular simulation). While the surrogate model developed in Chapter 4 specifically addresses this issue, the computational cost of creating an appropriate training dataset for such a data-driven surrogate model is substantial. For example, the dynamic LV simulation dataset, containing 540 simulations, required 3240 hours of CPU time. This computational cost, scaling with the complexity of the model and the size of the parameter space, makes creating a data-driven surrogate model for HCMM simulations a formidable challenge.

While it is technically possible to integrate all three tools to create a fast, multiscale patient-specific growth model, the challenges outlined above need to be addressed first. Without resolving the issues related to clinical data scarcity, labor-intensive image processing, and high computational costs, the resulting model would lack clinical relevance. The predictions, though potentially feasible from a computational standpoint, would not align with the rigorous demands of clinical practice, limiting their effectiveness for real-world application. Therefore, concerted efforts in overcoming these obstacles are critical for the realization of a truly effective and clinically applicable growth model.

5.3 Future perspectives

In this thesis, I have developed and explored tools and methods for patient-specific simulation, focusing on cardiac growth and left ventricular dynamics. These foundational efforts serve as initial steps towards constructing a cardiac digital twin and offer a launchpad for further advancements in this arena. Despite its promise, this work is still in its early stages, with challenges and limitations discussed above. In the subsequent sections, I will outline potential directions for future research, considering improvements to the current workflow, the broader applications of these techniques, and the exciting prospect of creating digital twins for the heart.

5.3.1 Towards patient-specific simulations of cardiac growth

Building upon the foundational work presented in this thesis, further advancements are necessary to fully realize the potential of patient-specific simulations for cardiac growth. The integration of the growth characterization workflow, multiscale growth model, and surrogate modeling methods holds promise for creating a comprehensive solution. However, the challenges previously identified in data collection, MRI data processing, and computational cost must be systematically addressed. Endomyocardial biopsy remains the gold standard for investigating myocardial microstructure [25]. Having serial biopsy to consistently monitor the microstructure evolution during G&R will provide invaluable data for validating simulations. Promising developments in tissue microstructural imaging, such as diffusion MRI [57] and collagen optical imaging [61], could offer valuable insights to refine the current growth models. Moreover, to accommodate potential large-scale imaging data, integration of existing automated segmentation tools [10], in conjunction with our automated meshing tool, could establish an efficient pipeline for large-scale simulation data generation. Although substantial computational cost in generating simulation datasets is an inherent challenge, judicious utilization of computational resources is possible through strategies like sensitivity analysis to minimize parameter space or utilizing advanced machine learning strategies like transfer learning and few-shot learning. Such adaptations can reduce both training data size and computational effort, speeding up the development of data-driven surrogate models, and thereby contributing to a more realistic and timely integration into clinical practice.

5.3.2 Cardiac digital twin

The tools developed in this thesis, particularly the characterization workflow and the data-driven model, have potential applications that extend beyond their initial scope. One significant application could be the non-invasive estimation of PV loops, currently obtainable only through invasive catheterization. By incorporating the inverse method from Chapter 2 with the surrogate model from Chapter 4, non-invasive PV loop measurements from cine cardiac MRI become a possibility. For accurate PV loop prediction, having a validated dynamic LV model, coupled with a diverse dataset of LV anatomies and dynamics, is essential. Though our model currently includes only the left ventricle, there is growing interest in studying the right heart. From a finite element simulation perspective, adding the right ventricle and even the atria wouldn't be overly complex, as demonstrated by other studies [111, 139, 113]. The challenge lies in reconstructing a 4-chamber geometry from cMRI and morphing all geometries from a single mesh. This would necessitate modifications to the existing meshing tool. Alternatively, we could possibly adopt other surrogate models, such as a Graph Neural Network, which has demonstrated promising performance in recreating structural simulations [97]. Depending on specific cardiovascular diseases (e.g. arrhythmia, thrombosis, or heart failure), simulating electrophysiology and hemodynamics may also be highly relevant. A multi-physics model coupling electrophysiology, structural dynamics, and hemodynamics could faithfully represent a digital twin of the heart. Although a fully electro-mechanical-fluid coupled heart model would be even more computationally demanding [113, 129], this very challenge underscores the value of developing a surrogate model for such complex simulations. Moreover, these methodologies are not confined to the heart but can be extended to create digital twins of other parts of the cardiovascular system and even other organs. As reviewed in Chapter 1, there is a wide range of interest in building patient-specific simulations for various human body parts, opening new avenues for personalized medicine and research.

5.3.3 Safety and trustworthy simulations

The integration of advanced simulation methods with artificial intelligence (AI) components, as seen in this thesis, opens a new frontier in cardiac modeling. However, it also raises crucial considerations regarding the safety and trustworthiness of these simulations. Rigorous methods for AI safety must be implemented to ensure that predictions and decisions derived from these models adhere to accepted medical standards and ethical guidelines. Techniques for uncertainty quantification could be explored to provide confidence intervals or error bounds on the predictions, adding transparency and reliability to the decision-making process. Collaborative work with experts in AI ethics, medical regulations, and clinical practice will be vital in establishing protocols and standards that govern the use of these technologies. Through comprehensive validation, continuous monitoring, and thoughtful integration of ethical principles, these simulations can become a trustworthy and indispensable part of future medical practice. Indeed, the work presented here represents a significant step towards making this vision a reality.

Bibliography

[1] Yasser Aboelkassem, Joseph D. Powers, Kimberly J. McCabe, and Andrew D. McCulloch. Multiscale models of cardiac muscle biophysics and tissue remodeling in hypertrophic cardiomyopathies. *Biomechanics: multiscale modeling mutations*, 416:429–435, 2019.

[2] Alec Radford, Karthik Narasimhan, Tim Salimans, and Ilya Sutskever. Improving language understanding by generative pre-training. Technical report, OpenAI, 2018.

[3] Maaike Alkema, Ernest Spitzer, Osama I I Soliman, and Christian Loewe. Multimodality imaging for left ventricular hypertrophy severity grading: A methodological review, 12 2016.

[4] Inder S Anand, Viorel G Florea, Scott D Solomon, Marvin A Konstam, and James E Udelson. Noninvasive assessment of left ventricular remodeling: concepts, techniques, and implications for clinical trials. *Journal of cardiac failure*, 8(6):452–64, 12 2002.

[5] Setareh Ariafar, Jaume Coll-Font, Dana Brooks, and Jennifer Dy. ADMMBO: Bayesian Optimization with Unknown Constraints using ADMM. *Journal of Machine Learning Research*, 20(123):1–26, 2019.

[6] Maximilian Balandat, Brian Karrer, Daniel R Jiang, Samuel Daulton, Benjamin Letham, Andrew Gordon Wilson, and Eytan Bakshy. BoTorch: A Framework for Efficient Monte-Carlo Bayesian Optimization. In *Advances in Neural Information Processing Systems 33*, 2020.

[7] Aditya Balu, Sahiti Nallagonda, Fei Xu, Adarsh Krishnamurthy, Ming-Chen Hsu, and Soumik Sarkar. A Deep Learning Framework for Design and Analysis of Surgical Bioprosthetic Heart Valves. *Scientific Reports*, 9(1):18560, 12 2019.

[8] Kathrin Bäumler, Vijay Vedula, Anna M. Sailer, Jongmin Seo, Peter Chiu, Gabriel Mistelbauer, Frandics P. Chan, Michael P. Fischbein, Alison L. Marsden, and Dominik Fleischmann. Fluid–structure interaction simulations of patient-specific aortic dissection. *Biomechanics and Modeling in Mechanobiology*, 19(5):1607–1628, 10 2020.

[9] J D Bayer, R C Blake, G Plank, and N A Trayanova. A novel rule-based algorithm for assigning myocardial fiber orientation to computational heart models. *Annals of biomedical engineering*, 40(10):2243–54, 10 2012.

[10] Olivier Bernard, Alain Lalande, Clement Zotti, Frederick Cervenansky, Xin Yang, Pheng Ann Heng, Irem Cetin, Karim Lekadir, Oscar Camara, Miguel Angel Gonzalez Ballester, Gerard Sanroma, Sandy Napel, Steffen Petersen, Georgios Tziritas, Elias Grinias, Mahendra Khened, Varghese Alex Kollerathu, Ganapathy Krishnamurthi, Marc Michel Rohe, Xavier Pennec, Maxime Sermesant, Fabian Isensee, Paul Jager, Klaus H. Maier-Hein, Peter M. Full, Ivo Wolf, Sandy Engelhardt, Christian F. Baumgartner, Lisa M. Koch, Jelmer M. Wolterink, Ivana Isgum, Yeonggul Jang, Yoonmi Hong, Jay Patravali, Shubham Jain, Olivier Humbert, and Pierre Marc Jodoin. Deep Learning Techniques for Automatic MRI Cardiac Multi-Structures Segmentation and Diagnosis: Is the Problem Solved? *IEEE Transactions on Medical Imaging*, 37(11):2514–2525, 11 2018.

[11] Marco Evangelos Biancolini, Katia Capellini, Emiliano Costa, Corrado Groth, and Simona Celi. Fast interactive CFD evaluation of hemodynamics assisted by RBF mesh morphing and reduced order models: the case of aTAA modelling. *International Journal on Interactive Design and Manufacturing*, 14(4):1227–1238, 12 2020.

[12] Stephen Boyd and Lieven Vandenberghe. *Convex Optimization*. Cambridge University Press, 2004.

[13] Patrick M. Boyle, Tarek Zghaib, Sohail Zahid, Rheeda L. Ali, Dongdong Deng, William H. Franceschi, Joe B. Hakim, Michael J. Murphy, Adityo Prakosa, Stefan L. Zimmerman, Hiroshi Ashikaga, Joseph E. Marine, Aravindan Kolandaivelu, Saman Nazarian, David D. Spragg, Hugh Calkins, and Natalia A. Trayanova. Computationally guided personalized targeted ablation of persistent atrial fibrillation. *Nature Biomedical Engineering 2019 3:11*, 3(11):870–879, 8 2019.

[14] Johane H. Bracamonte, Sarah K. Saunders, John S. Wilson, Uyen T. Truong, and Joao S. Soares. Patient-Specific Inverse Modeling of In Vivo Cardiovascular Mechanics with Medical Image-Derived Kinematics as Input Data: Concepts, Methods, and Applications. *Applied Sciences 2022, Vol. 12, Page 3954*, 12(8):3954, 4 2022.

[15] F. A. Braeu, A. Seitz, R. C. Aydin, and C. J. Cyron. Homogenized constrained mixture models for anisotropic volumetric growth and remodeling. *Biomechanics and Modeling in Mechanobiology*, 16(3):889–906, 6 2017.

[16] Stefano Buoso, Thomas Joyce, and Sebastian Kozerke. Personalising left-ventricular biophysical models of the heart using parametric physics-informed neural networks. *Medical Image Analysis*, page 102066, 4 2021.

[17] Daniel Burkhoff, Veli K. Topkara, Gabriel Sayer, and Nir Uriel. Reverse Remodeling With Left Ventricular Assist Devices. *Circulation Research*, 128(10):1594–1612, 5 2021.

[18] Li Cai, Lei Ren, Yongheng Wang, Wenxian Xie, Guangyu Zhu, and Hao Gao. Surrogate models based on machine learning methods for parameter estimation of left ventricular myocardium. *Royal Society Open Science*, 8(1), 1 2021.

[19] Victor M. Campello, Polyxeni Gkontra, Cristian Izquierdo, Carlos Martin-Isla, Alireza Sojoudi, Peter M. Full, Klaus Maier-Hein, Yao Zhang, Zhiqiang He, Jun Ma, Mario Parreno, Alberto Albiol, Fanwei Kong, Shawn C. Shadden, Jorge Corral Acero, Vaanathi Sundaresan, Mina Saber, Mustafa Elattar, Hongwei Li, Bjoern Menze, Firas Khader, Christoph Haarburger, Cian M. Scannell, Mitko Veta, Adam Carscadden, Kumaradevan Punithakumar, Xiao Liu, Sotirios A. Tsaftaris, Xiaoqiong Huang, Xin Yang, Lei Li, Xiahai Zhuang, David Vilades, Martin L. Descalzo, Andrea Guala, Lucia La Mura, Matthias G. Friedrich, Ria Garg, Julie Lebel, Filipe Henriques, Mahir Karakas, Ersin Cavus, Steffen E. Petersen, Sergio Escalera, Santi Segui, Jose F. Rodriguez-Palomares, and Karim Lekadir. Multi-Centre, Multi-Vendor and Multi-Disease Cardiac Segmentation: The MMs Challenge. *IEEE Transactions on Medical Imaging*, 40(12):3543–3554, 12 2021.

[20] Claudio Capelli, Emilie Sauvage, Giuliano Giusti, Giorgia M. Bosi, Hopewell Ntsinjana, Mario Carminati, Graham Derrick, Jan Marek, Sachin Khambadkone, Andrew M. Taylor, and Silvia Schievano. Patient-specific simulations for planning treatment in congenital heart disease. *Interface Focus*, 8(1), 2 2018.

[21] Francesco Castagna, Eric J. Stöhr, Alberto Pinsino, John R. Cockcroft, Joshua Willey, A. Reshad Garan, Veli K. Topkara, Paolo C. Colombo, Melana Yuzefpolskaya, and Barry J. McDonnell. The Unique Blood Pressures and Pulsatility of LVAD Patients: Current Challenges and Future Opportunities. *Current Hypertension Reports*, 19(10), 10 2017.

[22] Duanduan Chen, Matthias Müller-Eschner, Hendrik von Tengg-Kobligk, David Barber, Dittmar Böckler, Rod Hose, and Yiannis Ventikos. A patient-specific study of type-B aortic dissection: Evaluation of true-false lumen blood exchange. *BioMedical Engineering Online*, 12(1):1–16, 7 2013.

[23] Z. Cheng, C. Juli, N. B. Wood, R. G.J. Gibbs, and X. Y. Xu. Predicting flow in aortic dissection: Comparison of computational model with PC-MRI velocity measurements. *Medical Engineering & Physics*, 36(9):1176–1184, 9 2014.

[24] Austin J. Cocciolone, Jie Z. Hawes, Marius C. Staiculescu, Elizabeth O. Johnson, Monzur Murshed, and Jessica E. Wagenseil. Elastin, arterial mechanics, and cardiovascular disease. *American journal of physiology. Heart and circulatory physiology*, 315(2):H189–H205, 8 2018.

[25] K. S. Cunningham, J. P. Veinot, and J. Butany. An approach to endomyocardial biopsy interpretation. *Journal of Clinical Pathology*, 59(2):121, 2 2006.

[26] C. J. Cyron, R. C. Aydin, and J. D. Humphrey. A homogenized constrained mixture (and mechanical analog) model for growth and remodeling of soft tissue. *Biomechanics and modeling in mechanobiology*, 15(6):1389, 12 2016.

[27] Yaghoub Dabiri, Kevin L. Sack, Nuno Rebelo, Peter Wang, Yunjie Wang, Jenny S. Choy, Ghassan S. Kassab, and Julius M. Guccione. Method for calibration of left ventri-

cle material properties using three-dimensional echocardiography endocardial strains. *Journal of Biomechanical Engineering*, 141(9), 9 2019.

[28] David Dalton, Hao Gao, and Dirk Husmeier. Emulation of cardiac mechanics using Graph Neural Networks. *Computer Methods in Applied Mechanics and Engineering*, 401:115645, 11 2022.

[29] David Dalton, Alan Lazarus, Arash Rabbani, Hao Gao, and Dirk Husmeier. Graph Neural Network Emulation of Cardiac Mechanics. In *3rd International Conference on Statistics: Theory and Applications*, 8 2021.

[30] Shusil Dangi, Cristian A. Linte, and Ziv Yaniv. Cine Cardiac MRI Slice Misalignment Correction Towards Full 3D Left Ventricle Segmentation. *Proceedings of SPIE–the International Society for Optical Engineering*, 10576:6, 3 2018.

[31] Dassault Systèmes. ABAQUS 2018 Documentation, 2018.

[32] Edwin D. de Jong. Incremental Sequence Learning. Technical report, Utrecht University, 11 2016.

[33] Lee R Dice. Measures of the Amount of Ecologic Association Between Species. *Ecology*, 26(3):297–302, 7 1945.

[34] Barry J. Doyle, Nikhilesh Bappoo, Maaz B.J. Syed, Rachael O. Forsythe, Janet T. Powell, Noel Conlisk, Peter R. Hoskins, Olivia M.B. McBride, Anoop S.V. Shah, Paul E. Norman, and David E. Newby. Biomechanical Assessment Predicts Aneurysm Related Events in Patients with Abdominal Aortic Aneurysm. *European Journal of Vascular and Endovascular Surgery*, 60(3):365–373, 9 2020.

[35] Yiling Fan, Jaume Coll-Font, Maaike van den Boomen, Joan H. Kim, Shi Chen, Robert Alan Eder, Ellen T. Roche, and Christopher T. Nguyen. Characterization of Exercise-Induced Myocardium Growth Using Finite Element Modeling and Bayesian Optimization. *Frontiers in Physiology*, 12, 8 2021.

[36] T Fernandes, U P R Soci, and E M Oliveira. Eccentric and concentric cardiac hypertrophy induced by exercise training: microRNAs and molecular determinants. *Braz J Med Biol Res*, 44(9):836–847, 2011.

[37] Mark F. Fillinger, Steven P. Marra, M. L. Raghavan, and Francis E. Kennedy. Prediction of rupture risk in abdominal aortic aneurysm during observation: Wall stress versus diameter. *Journal of Vascular Surgery*, 37(4):724–732, 4 2003.

[38] Henrik Finsberg, Gabriel Balaban, Stian Ross, Trine F. Håland, Hans Henrik Odland, Joakim Sundnes, and Samuel Wall. Estimating cardiac contraction through high resolution data assimilation of a personalized mechanical model. *Journal of Computational Science*, 24:85–90, 1 2018.

[39] Petter Frieberg, Nicolas Aristokleous, Pia Sjöberg, Johannes Töger, Petru Liuba, and Marcus Carlsson. Computational Fluid Dynamics Support for Fontan Planning in Minutes, Not Hours: The Next Step in Clinical Pre-Interventional Simulations. *Journal of Cardiovascular Translational Research*, 15(4):708–720, 8 2022.

[40] Thomas Fritz, Christian Wieners, Gunnar Seemann, Henning Steen, and Olaf Dössel. Simulation of the contraction of the ventricles in a human heart model including atria and pericardium: Finite element analysis of a frictionless contact problem. *Biomechanics and Modeling in Mechanobiology*, 13(3):627–641, 8 2014.

[41] Louis Garber, Seyedvahid Khodaei, and Zahra Keshavarz-Motamed. The Critical Role of Lumped Parameter Models in Patient-Specific Cardiovascular Simulations. *Archives of Computational Methods in Engineering 2021 29:5*, 29(5):2977–3000, 12 2021.

[42] Amadeus M. Gebauer, Martin R. Pfaller, Fabian A. Braeu, Christian J. Cyron, and Wolfgang A. Wall. A homogenized constrained mixture model of cardiac growth and remodeling: Analyzing mechanobiological stability and reversal. *Biomechanics and Modeling in Mechanobiology 2023*, pages 1–20, 3 2022.

[43] M. W. Gee, Ch Förster, and W. A. Wall. A computational strategy for prestressing patient-specific biomechanical problems under finite deformation. *International Journal for Numerical Methods in Biomedical Engineering*, 26(1):52–72, 1 2010.

[44] M. Genet, L. C. Lee, B. Baillargeon, J. M. Guccione, and E. Kuhl. Modeling Pathologies of Diastolic and Systolic Heart Failure. *Annals of Biomedical Engineering*, 44(1):112–127, 2016.

[45] A. Martin Gerdes. Cardiac myocyte remodeling in hypertrophy and progression to failure. *Journal of Cardiac Failure*, 8(6):S264–S268, 12 2002.

[46] Mojgan Ghodrati, Alexander Maurer, Thomas Schlöglhofer, Thananya Khienwad, Daniel Zimpfer, Dietrich Beitzke, Francesco Zonta, Francesco Moscato, Heinrich Schima, and Philipp Aigner. The influence of left ventricular assist device inflow cannula position on thrombosis risk. *Artificial Organs*, 44(9):939–946, 9 2020.

[47] Serdar Göktepe, Oscar John Abilez, Kevin Kit Parker, and Ellen Kuhl. A multiscale model for eccentric and concentric cardiac growth through sarcomerogenesis. *Journal of Theoretical Biology*, 265(3):433–442, 8 2010.

[48] Debao Guan, Xin Zhuan, Xiaoyu Luo, and Hao Gao. An updated Lagrangian constrained mixture model of pathological cardiac growth and remodelling. *Acta Biomaterialia*, 166:375–399, 8 2023.

[49] J M Guccione and A D McCulloch. Mechanics of active contraction in cardiac muscle: Part I–Constitutive relations for fiber stress that describe deactivation. *Journal of biomechanical engineering*, 115(1):72–81, 2 1993.

[50] Xu Han, Han Gao, Tobias Pfaff, Jian-Xun Wang, and Li-Ping Liu. Predicting Physics in Mesh-reduced Space with Temporal Attention. In *International Conference on Learning Representations (ICLR)*, 1 2022.

[51] Einar Heiberg, Jane Sjögren, Martin Ugander, Marcus Carlsson, Henrik Engblom, and Håkan Arheden. Design and validation of Segment-freely available software for cardiovascular image analysis. *BMC Medical Imaging*, 10(1), 2010.

[52] José Miguel Hernández-Lobato, Michael A Gelbart, Matthew W Hoffman, Ryan P Adams, and Zoubin Ghahramani. Predictive Entropy Search for Bayesian Optimization with Unknown Constraints. Technical report, Harvard University, 2 2015.

[53] Matthew Hoffman, Eric Brochu, and Nando De Freitas. Portfolio Allocation for Bayesian Optimization. *Conference on Uncertainty in Artificial Intelligence*, pages 327–336, 2011.

[54] Yu Hohri, Keiichi Itatani, Sachiko Yamazaki, and Hitoshi Yaku. Computerized virtual surgery based on computational fluid dynamics simulation for planning coronary revascularization with aortic root replacement in adult congenital heart disease: a case report. *General Thoracic and Cardiovascular Surgery*, 69(4):722–726, 4 2021.

[55] Gerhard A. Holzapfel and Ray W. Ogden. Constitutive modelling of passive myocardium: A structurally based framework for material characterization. *Philosophical Transactions of the Royal Society A: Mathematical, Physical and Engineering Sciences*, 367(1902):3445–3475, 2009.

[56] Katherine M. Holzem, Joseph T. Marmerstein, Eli J. Madden, and Igor R. Efimov. Diet-induced obesity promotes altered remodeling and exacerbated cardiac hypertrophy following pressure overload. *Physiological Reports*, 3(8), 2015.

[57] Shuning Huang and David E. Sosnovik. Molecular and Microstructural Imaging of the Myocardium. *Current cardiovascular imaging reports*, 3(1):26, 2010.

[58] J. D. Humphrey. Stress, strain, and mechanotransduction in cells. *Journal of biomechanical engineering*, 123(6):638–641, 2001.

[59] J. D. Humphrey and K. R. Rajagopal. A CONSTRAINED MIXTURE MODEL FOR GROWTH AND REMODELING OF SOFT TISSUES. *https://doi.org/10.1142/S0218202502001714*, 12(3):407–430, 11 2002.

[60] Frank Hutter, Holger H Hoos, and Kevin Leyton-Brown. Sequential Model-Based Optimization for General Algorithm Configuration. In *Lecture Notes in Computer Science (including subseries Lecture Notes in Artificial Intelligence and Lecture Notes in Bioinformatics)*, volume 6683 LNCS, pages 507–523, 2011.

[61] Leanne E. Iannucci, Charles S. Dranoff, Michael A. David, and Spencer P. Lake. Optical Imaging of Dynamic Collagen Processes in Health and Disease. *Frontiers in Mechanical Engineering*, 8:855271, 3 2022.

[62] Teruhiko Imamura, Valluvan Jeevanandam, Gene Kim, Jayant Raikhelkar, Nitasha Sarswat, Sara Kalantari, Bryan Smith, Daniel Rodgers, Stephanie Besser, Ben Chung, Ann Nguyen, Nikhil Narang, Takeyoshi Ota, Tae Song, Colleen Juricek, Mandeep Mehra, Maria Rosa Costanzo, Ulrich P. Jorde, Daniel Burkhoff, Gabriel Sayer, and Nir Uriel. Optimal Hemodynamics during Left Ventricular Assist Device Support Are Associated with Reduced Readmission Rates. *Circulation: Heart Failure*, 12(2), 2 2019.

[63] Suo Jin, Yan Yang, John Oshinski, Allen Tannenbaum, James Gruden, and Don Giddens. Flow patterns and wall shear stress distributions at atherosclerotic-prone sites in a human left coronary artery - An exploration using combined methods of CT and computational fluid dynamics. *Annual International Conference of the IEEE Engineering in Medicine and Biology - Proceedings*, 26 V:3789–3791, 2004.

[64] Donald R Jones, Matthias Schonlau, and William J Welch. Efficient Global Optimization of Expensive Black-Box Functions. *Journal of Global Optimization*, 13(4):455–492, 1998.

[65] Maria Rolstad Jordal, Sverre Gullikstad Johnsen, Sigrid Kaarstad Dahl, and Bernhard Müller. Patient specific numerical simulation of flow in the human upper airways for assessing the effect of nasal surgery. In *12th International Conference on CFD in Oil & Gas, Metallurgical and Process Industries*, 6 2017.

[66] Izhak Kehat and Jeffery D. Molkentin. Molecular Pathways Underlying Cardiac Remodeling During Pathophysiological Stimulation. *Circulation*, 122(25):2727–2735, 12 2010.

[67] H J Kushner. A new method of locating the maximum point of an arbitrary multipeak curve in the presence of noise. *Journal of Fluids Engineering, Transactions of the ASME*, 86(1):97–106, 3 1964.

[68] John F. LaDisa, Charles A. Taylor, and Jeffrey A. Feinstein. Aortic coarctation: Recent developments in experimental and computational methods to assess treatments for this simple condition. *Progress in Pediatric Cardiology*, 30(1-2):45–49, 12 2010.

[69] Hamid Ladjal, Michael Beuve, Philippe Giraud, and Behzad Shariat. Towards Non-Invasive Lung Tumor Tracking Based on Patient Specific Model of Respiratory System. *IEEE Transactions on Biomedical Engineering*, 68(9):2730–2740, 9 2021.

[70] Ian J. LeGrice, Adèle J. Pope, Gregory B. Sands, Gillian Whalley, Robert N. Doughty, and Bruce H. Smaill. Progression of myocardial remodeling and mechanical dysfunction in the spontaneously hypertensive rat. *American Journal of Physiology - Heart and Circulatory Physiology*, 303(11):H1353–H1365, 12 2012.

[71] James H. Leung, Andrew R. Wright, Nick Cheshire, Jeremy Crane, Simon A. Thom, Alun D. Hughes, and Yun Xu. Fluid structure interaction of patient specific abdominal aortic aneurisms: A comparison with solid stress models. *BioMedical Engineering Online*, 5(1):1–15, 5 2006.

[72] Shujuan Li, Ngoc Uyen Nhi Nguyen, Feng Xiao, Ivan Menendez-Montes, Yuji Nakada, Wilson Lek Wen Tan, Chukwuemeka George Anene-Nzelu, Roger S. Foo, Suwannee Thet, Alisson Campos Cardoso, Ping Wang, Waleed M. Elhelaly, Nicholas T. Lam, Ana Helena Mac Edo Pereira, Joseph A. Hill, and Hesham A. Sadek. Mechanism of Eccentric Cardiomyocyte Hypertrophy Secondary to Severe Mitral Regurgitation. *Circulation*, 141(22):1787–1799, 6 2020.

[73] Shengmao Lin, Praveen Akula, and Linxia Gu. Mechanical Performance of Bovine Pericardial Bioprosthetic Valves. Technical report, University of Nebraska, Lincoln, 2013.

[74] Haytham Mansour, Pieter P De Tombe, Allen M Samarel, and Brenda Russell. Restoration of Resting Sarcomere Length After Uniaxial Static Strain Is Regulated by Protein Kinase C and Focal Adhesion Kinase. *Circulation Research*, 2004.

[75] Martin S. Maron, Barry J. Maron, Caitlin Harrigan, Jacki Buros, C. Michael Gibson, Iacopo Olivotto, Leah Biller, John R. Lesser, James E. Udelson, Warren J. Manning, and Evan Appelbaum. Hypertrophic Cardiomyopathy Phenotype Revisited After 50 Years With Cardiovascular Magnetic Resonance. *Journal of the American College of Cardiology*, 54(3):220–228, 7 2009.

[76] Alison L. Marsden, Adam J. Bernstein, V. Mohan Reddy, Shawn C. Shadden, Ryan L. Spilker, Frandics P. Chan, Charles A. Taylor, and Jeffrey A. Feinstein. Evaluation of a novel Y-shaped extracardiac Fontan baffle using computational fluid dynamics. *The Journal of Thoracic and Cardiovascular Surgery*, 137(2):394–403, 2 2009.

[77] Per Gunnar Martinsson, Vladimir Rokhlin, and Mark Tygert. A randomized algorithm for the decomposition of matrices. *Applied and Computational Harmonic Analysis*, 30(1):47–68, 1 2011.

[78] Gonzalo D. Maso Talou, Thiranja P. Babarenda Gamage, Mark Sagar, and Martyn P. Nash. Deep Learning Over Reduced Intrinsic Domains for Efficient Mechanics of the Left Ventricle. *Frontiers in Physics*, 8:508377, 2 2020.

[79] Michael McElroy, Antonios Xenakis, and Amir Keshmiri. Impact of heart failure severity on ventricular assist device haemodynamics: a computational study. *Research on Biomedical Engineering*, 36(4):489–500, 12 2020.

[80] Julie R. McMullen and Garry L. Jennings. Differences between pathological and physiological cardiac hypertrophy: Novel therapeutic strategies to treat heart failure. *Clinical and Experimental Pharmacology and Physiology*, 34(4):255–262, 2007.

[81] C. Mihl, W. R.M. Dassen, and H. Kuipers. Cardiac remodelling: Concentric versus eccentric hypertrophy in strength and endurance athletes, 2008.

[82] Chihiro Miyagi, Takuma Miyamoto, Taiyo Kuroda, Jamshid H. Karimov, Randall C. Starling, and Kiyotaka Fukamachi. Large animal models of heart failure with preserved ejection fraction. *Heart failure reviews*, 27(2):595–608, 3 2022.

[83] S. Jamaleddin Mousavi and Stéphane Avril. Patient-specific stress analyses in the ascending thoracic aorta using a finite-element implementation of the constrained mixture theory. *Biomechanics and Modeling in Mechanobiology*, 16(5):1765–1777, 10 2017.

[84] Andriy Myronenko and Xubo Song. Point-Set Registration: Coherent Point Drift. *IEEE Transactions on Pattern Analysis and Machine Intelligence*, 32(12):2262–2275, 5 2009.

[85] Ken Nakayama, Yukio Oshiro, Ryoichi Miyamoto, Keisuke Kohno, Kiyoshi Fukunaga, and Nobuhiro Ohkohchi. The Effect of Three-Dimensional Preoperative Simulation on Liver Surgery. *World Journal of Surgery*, 41(7):1840–1847, 7 2017.

[86] J A Nelder and R Mead. A Simplex Method for Function Minimization. *Comput. J.*, 7:308–313, 1965.

[87] Steven A. Niederer, Joost Lumens, and Natalia A. Trayanova. Computational models in cardiology. *Nature Reviews Cardiology 2018 16:2*, 16(2):100–111, 10 2018.

[88] Justyna A. Niestrawska, Christoph M. Augustin, and Gernot Plank. Computational modeling of cardiac growth and remodeling in pressure overloaded hearts—Linking microstructure to organ phenotype, 4 2020.

[89] Jorge Nocedal and Stephen J Wright. *Numerical Optimization*. Springer, Ithaca, NY, 2nd edition, 2000.

[90] T. Dylan Olver, Jenna C. Edwards, Thomas J. Jurrissen, Adam B. Veteto, John L. Jones, Chen Gao, Christoph Rau, Chad M. Warren, Paula J. Klutho, Linda Alex, Stephanie C. Ferreira-Nichols, Jan R. Ivey, Pamela K. Thorne, Kerry S. McDonald, Maike Krenz, Christopher P. Baines, R. John Solaro, Yibin Wang, David A. Ford, Timothy L. Domeier, Jaume Padilla, R. Scott Rector, and Craig A. Emter. Western Diet-Fed, Aortic-Banded Ossabaw Swine: A Preclinical Model of Cardio-Metabolic Heart Failure. *JACC: Basic to Translational Science*, 4(3):404–421, 6 2019.

[91] Michael A Osborne, Roman Garnett, and Stephen J Roberts. Gaussian processes for global optimization. In *3rd international conference on learning and intelligent optimization ({LION3})*, pages 1–15, 2009.

[92] Caglar Ozturk, Luca Rosalia, and Ellen T. Roche. A Multi-Domain Simulation Study of a Pulsatile-Flow Pump Device for Heart Failure With Preserved Ejection Fraction. *Frontiers in Physiology*, 13:815787, 1 2022.

[93] Arnab Palit, Sunil K. Bhudia, Theodoros N. Arvanitis, Glen A. Turley, and Mark A. Williams. In vivo estimation of passive biomechanical properties of human myocardium. *Medical and Biological Engineering and Computing*, 56(9):1615–1631, 9 2018.

[94] Charles R. Pedlar, Marcel G. Brown, Robert E. Shave, James M. Otto, Aimee Drane, Jennifer Michaud-Finch, Miranda Contursi, Meagan M. Wasfy, Adolph Hutter,

Michael H. Picard, Gregory D. Lewis, and Aaron L. Baggish. Cardiovascular response to prescribed detraining among recreational athletes. *Journal of Applied Physiology*, 124(4):813–820, 4 2018.

[95] M Peirlinck, · F Sahli Costabal, · K L Sack, · J S Choy, · G S Kassab, · J M Guccione, · M De Beule, · P Segers, and · E Kuhl. Using machine learning to characterize heart failure across the scales. *Biomechanics and Modeling in Mechanobiology*, 18:1987–2001, 2019.

[96] Ana Rubina Perestrelo, Ana Catarina Silva, Jorge Oliver-De La Cruz, Fabiana Martino, Vladimír Horváth, Guido Caluori, Ondřej Polanský, Vladimír Vinarský, Giulia Azzato, Giuseppe De Marco, Víta Žampachová, Petr Skládal, Stefania Pagliari, Alberto Rainer, Perpétua Pinto-Do-Ó, Alessio Caravella, Kamila Koci, Diana S. Nascimento, and Giancarlo Forte. Multiscale Analysis of Extracellular Matrix Remodeling in the Failing Heart. *Circulation Research*, 128(1):24–38, 1 2021.

[97] Tobias Pfaff, Meire Fortunato, Alvaro Sanchez-Gonzalez, and Peter W. Battaglia. Learning Mesh-Based Simulation with Graph Networks. *ICLR 2021 - 9th International Conference on Learning Representations*, 10 2020.

[98] Martin R Pfaller, Julia M Hörmann, Martina Weigl, Andreas Nagler, Radomir Chabiniok, Cristóbal Bertoglio, and Wolfgang A Wall. The importance of the pericardium for cardiac biomechanics: from physiology to computational modeling. *Biomechanics and Modeling in Mechanobiology*, 18(2):503–529, 2019.

[99] Patrick M. Pilz, Jennifer E. Ward, Wei Ting Chang, Attila Kiss, Edward Bateh, Alokkumar Jha, Sudeshna Fisch, Bruno K. Podesser, and Ronglih Liao. Large and Small Animal Models of Heart Failure With Reduced Ejection Fraction. *Circulation Research*, 130(12):1888–1905, 6 2022.

[100] Mjd Powell. The BOBYQA algorithm for bound constrained optimization without derivatives. *NA Report NA2009/06*, page 39, 2009.

[101] A Prakosa, P Malamas, S Zhang, F Pashakhanloo, H Arevalo, D A Herzka, A Lardo, H Halperin, E McVeigh, N Trayanova, and F Vadakkumpadan. Methodology for image-based reconstruction of ventricular geometry for patient-specific modeling of cardiac electrophysiology. *Progress in Biophysics and Molecular Biology*, 115(2-3):226–234, 8 2014.

[102] Adityo Prakosa, Hermenegild J. Arevalo, Dongdong Deng, Patrick M. Boyle, Plamen P. Nikolov, Hiroshi Ashikaga, Joshua J.E. Blauer, Elyar Ghafoori, Carolyn J. Park, Robert C. Blake, Frederick T. Han, Rob S. MacLeod, Henry R. Halperin, David J. Callans, Ravi Ranjan, Jonathan Chrispin, Saman Nazarian, and Natalia A. Trayanova. Personalized virtual-heart technology for guiding the ablation of infarct-related ventricular tachycardia. *Nature Biomedical Engineering*, 2(10):732–740, 10 2018.

[103] A. G. Radaelli, L. Augsburger, J. R. Cebral, M. Ohta, D. A. Rüfenacht, R. Balossino, G. Benndorf, D. R. Hose, A. Marzo, R. Metcalfe, P. Mortier, F. Mut, P. Reymond,

L. Socci, B. Verhegghe, and A. F. Frangi. Reproducibility of haemodynamical simulations in a subject-specific stented aneurysm model—A report on the Virtual Intracranial Stenting Challenge 2007. *Journal of Biomechanics*, 41(10):2069–2081, 7 2008.

[104] Carl E Rasmussen and Christopher K I Williams. *Gaussian Processes for Machine Learning.* MIT Press, Cambridge, MA, 2006.

[105] M K Rausch, · A Dam, · S Göktepe, · O J Abilez, · E Kuhl, S Göktepe, O J Abilez, and E Kuhl. Computational modeling of growth: systemic and pulmonary hypertension in the heart. *Biomech Model Mechanobiol*, 10:799–811, 2011.

[106] Manuel K. Rausch, Martin Genet, and Jay D. Humphrey. An augmented iterative method for identifying a stress-free reference configuration in image-based biomechanical modeling. *Journal of Biomechanics*, 58:227–231, 6 2017.

[107] F. Regazzoni, M. Salvador, L. Dede, and A. Quarteroni. A machine learning method for real-time numerical simulations of cardiac electromechanics. *Computer Methods in Applied Mechanics and Engineering*, 393:114825, 4 2022.

[108] Edward K. Rodriguez, Anne Hoger, and Andrew D. McCulloch. Stress-dependent finite growth in soft elastic tissues. *Journal of Biomechanics*, 27(4):455–467, 4 1994.

[109] Olaf Ronneberger, Philipp Fischer, and Thomas Brox. U-net: Convolutional networks for biomedical image segmentation. *Lecture Notes in Computer Science (including subseries Lecture Notes in Artificial Intelligence and Lecture Notes in Bioinformatics)*, 9351:234–241, 2015.

[110] Kevin L. Sack, Eric Aliotta, Daniel B. Ennis, Jenny S. Choy, Ghassan S. Kassab, Julius M. Guccione, and Thomas Franz. Construction and Validation of Subject-Specific Biventricular Finite-Element Models of Healthy and Failing Swine Hearts From High-Resolution DT-MRI. *Frontiers in Physiology*, 9:539, 5 2018.

[111] Kevin L. Sack, Brian Baillargeon, Gabriel Acevedo-Bolton, Martin Genet, Nuno Rebelo, Ellen Kuhl, Liviu Klein, Georg M. Weiselthaler, Daniel Burkhoff, Thomas Franz, and Julius M. Guccione. Partial LVAD restores ventricular outputs and normalizes LV but not RV stress distributions in the acutely failing heart in silico. *International Journal of Artificial Organs*, 2016.

[112] F. Sahli Costabal, J. S. Choy, K. L. Sack, J. M. Guccione, G. S. Kassab, and E. Kuhl. Multiscale characterization of heart failure. *Acta Biomaterialia*, 86:66–76, 3 2019.

[113] Alfonso Santiago, Jazmín Aguado-Sierra, Miguel Zavala-Aké, Ruben Doste-Beltran, Samuel Gómez, Ruth Arís, Juan C. Cajas, Eva Casoni, and Mariano Vázquez. Fully coupled fluid-electro-mechanical model of the human heart for supercomputers. *International Journal for Numerical Methods in Biomedical Engineering*, 34(12):e3140, 12 2018.

[114] Marie Schafstedde, Pavlo Yevtushenko, Sarah Nordmeyer, Peter Kramer, Anastasia Schleiger, Natalia Solowjowa, Felix Berger, Joachim Photiadis, Yaroslav Mykychak, Mi Young Cho, Stanislav Ovroutski, Titus Kuehne, and Jan Brüning. Virtual treatment planning in three patients with univentricular physiology using computational fluid dynamics—Pitfalls and strategies. *Frontiers in Cardiovascular Medicine*, 9:898701, 8 2022.

[115] Polina A Segalova, Guanglei Xiong, K T Rao, Christopher K Zarins, Charles A Taylor, Jinming Sun, and Philip A Voglewede. Evaluating Design of Abdominal Aortic Aneurysm Endografts in a Patient-Specific Model Using Computational Fluid Dynamics. *Journal of Medical Devices*, 5(2):27505–27506, 6 2011.

[116] M. Sermesant, R. Chabiniok, P. Chinchapatnam, T. Mansi, F. Billet, P. Moireau, J. M. Peyrat, K. Wong, J. Relan, K. Rhode, M. Ginks, P. Lambiase, H. Delingette, M. Sorine, C. A. Rinaldi, D. Chapelle, R. Razavi, and N. Ayache. Patient-specific electromechanical models of the heart for the prediction of pacing acute effects in CRT: A preliminary clinical validation. *Medical Image Analysis*, 16(1):201–215, 1 2012.

[117] Palak Shah, Mitchell Psotka, Iosif Taleb, Rami Alharethi, Mortada A. Shams, Omar Wever-Pinzon, Michael Yin, Federica Latta, Josef Stehlik, James C. Fang, Guoqing Diao, Ramesh Singh, Naila Ijaz, Christos P. Kyriakopoulos, Wei Zhu, Christopher W. May, Lauren B. Cooper, Shashank S. Desai, Craig H. Selzman, Abdallah G. Kfoury, and Stavros G. Drakos. Framework to Classify Reverse Cardiac Remodeling with Mechanical Circulatory Support: The Utah-Inova Stages. *Circulation: Heart Failure*, pages 553–563, 2021.

[118] Hossein Sharifi, Charles K. Mann, Alexus L. Rockward, Mohammad Mehri, Joy Mojumder, Lik Chuan Lee, Kenneth S. Campbell, and Jonathan F. Wenk. Multiscale simulations of left ventricular growth and remodeling. *Biophysical Reviews 2021 13:5*, 13(5):729–746, 8 2021.

[119] Petri Sipola, Jarkko Magga, Minna Husso, Pertti Jääskeläinen, Keijo Peuhkurinen, and Johanna Kuusisto. Cardiac MRI assessed left ventricular hypertrophy in differentiating hypertensive heart disease from hypertrophic cardiomyopathy attributable to a sarcomeric gene mutation. *European Radiology*, 21(7):1383–1389, 7 2011.

[120] Niranjan Srinivas, Andreas Krause, Sham M Kakade, and Matthias Seeger. Gaussian Process Optimization in the Bandit Setting: No Regret and Experimental Design. *Proceedings of the 27th International Conference on Machine Learning (ICML 2010)*, pages 1015–1022, 2010.

[121] Jess D. Tate, Nejib Zemzemi, Wilson W. Good, Peter Van Dam, Dana H. Brooks, and Rob S. MacLeod. Shape Analysis of Segmentation Variability. In *Computing in Cardiology*, volume 2020-September. IEEE Computer Society, 9 2020.

[122] M. Thrinayan, Shubhanvit Mishra, Ch Murali Naga Mahesh, and P. Muthu. Patient Specific Coronary Stent Designing and its Computational Analysis using Ansys. *Journal of Physics: Conference Series*, 1362(1):012052, 11 2019.

[123] Juan Torrado, Gurukripa N. Kowlgi, Rafael J. Ramirez, Jaime Balderas-Villalobos, Daniel Jovin, Chandler Parker, Evani Om, Sergei Airapetov, Karoly Kaszala, Alex Y. Tan, Kenneth A. Ellenbogen, and Jose F. Huizar. Eccentric hypertrophy in an animal model of mid- and long-term premature ventricular contraction–induced cardiomyopathy. *Heart Rhythm O2*, 2(1):80–88, 2 2021.

[124] William M. Torres, Shayne C. Barlow, Amber Moore, Lisa A. Freeburg, Abigail Hoenes, Heather Doviak, Michael R. Zile, Tarek Shazly, and Francis G. Spinale. Changes in Myocardial Microstructure and Mechanics With Progressive Left Ventricular Pressure Overload. *JACC: Basic to Translational Science*, 5(5):463–480, 5 2020.

[125] Giuseppe Emmanuele Umana, Gianluca Scalia, Kaan Yagmurlu, Rosalia Mineo, Simone Di Bella, Matteo Giunta, Angelo Spitaleri, Rosario Maugeri, Francesca Graziano, Marco Fricia, Giovanni Federico Nicoletti, Santino Ottavio Tomasi, Giuseppe Raudino, Bipin Chaurasia, Gianluca Bellocchi, Maurizio Salvati, Domenico Gerardo Iacopino, Salvatore Cicero, Massimiliano Visocchi, and Lidia Strigari. Multimodal Simulation of a Novel Device for a Safe and Effective External Ventricular Drain Placement. *Frontiers in Neuroscience*, 15, 6 2021.

[126] Jonathan P. Vande Geest, Michael S. Sacks, and David A. Vorp. Age Dependency of the Biaxial Biomechanical Behavior of Human Abdominal Aorta. *Journal of Biomechanical Engineering*, 126(6):815–822, 12 2004.

[127] Rick B. Vega, John P. Konhilas, Daniel P. Kelly, and Leslie A. Leinwand. Molecular Mechanisms Underlying Cardiac Adaptation to Exercise, 5 2017.

[128] A. K. Venkatasubramaniam, M. J. Fagan, T. Mehta, K. J. Mylankal, B. Ray, G. Kuhan, I. C. Chetter, and P. T. McCollum. A Comparative Study of Aortic Wall Stress Using Finite Element Analysis for Ruptured and Non-ruptured Abdominal Aortic Aneurysms. *European Journal of Vascular and Endovascular Surgery*, 28(2):168–176, 8 2004.

[129] Francesco Viola, Giulio Del Corso, Ruggero De Paulis, and Roberto Verzicco. GPU accelerated digital twins of the human heart open new routes for cardiovascular research. *Scientific Reports 2023 13:1*, 13(1):1–18, 5 2023.

[130] Y. Wang, U. Wisloff, and O. J. Kemi. Animal models in the study of exercise-induced cardiac hypertrophy. *Physiological Research*, 59(5):633–644, 2010.

[131] Zhinuo J. Wang, Vicky Y. Wang, Thiranja P. Babarenda Gamage, Vijayaraghavan Rajagopal, J. Jane Cao, Poul M.F. Nielsen, Chris P. Bradley, Alistair A. Young, and Martyn P. Nash. Efficient estimation of load-free left ventricular geometry and passive myocardial properties using principal component analysis. *International Journal for Numerical Methods in Biomedical Engineering*, 36(3):e3313, 3 2020.

[132] Zhinuo J. Wang, Vicky Y. Wang, Chris P. Bradley, Martyn P. Nash, Alistair A. Young, and J. Jane Cao. Left Ventricular Diastolic Myocardial Stiffness and End-Diastolic

Myofibre Stress in Human Heart Failure Using Personalised Biomechanical Analysis. *Journal of Cardiovascular Translational Research*, 11(4):346–356, 2018.

[133] Zhinuo Jenny Wang, Vicky Y. Wang, Chris P. Bradley, Martyn P. Nash, Alistair Young, and Jie J. Cao. Quantifying passive myocardial stiffness and wall stress in heart failure patients using personalized ventricular mechanics. *Journal of Cardiovascular Magnetic Resonance*, 18(1):1–2, 1 2016.

[134] Alexander J. Wilson, Vicky Y. Wang, Gregory B. Sands, Alistair A. Young, Martyn P. Nash, and Ian J. LeGrice. Increased cardiac work provides a link between systemic hypertension and heart failure. *Physiological Reports*, 5(1), 1 2017.

[135] J. S. Wilson, S. Baek, and J. D. Humphrey. Importance of initial aortic properties on the evolving regional anisotropy, stiffness and wall thickness of human abdominal aortic aneurysms. *Journal of the Royal Society Interface*, 9(74):2047, 9 2012.

[136] Colleen M. Witzenburg and Jeffrey W. Holmes. A Comparison of Phenomenologic Growth Laws for Myocardial Hypertrophy. *Journal of Elasticity*, 129(1-2):257–281, 12 2017.

[137] Ce Xi, Ghassan S. Kassab, and Lik Chuan Lee. Microstructure-based finite element model of left ventricle passive inflation. *Acta Biomaterialia*, 90:241–253, 5 2019.

[138] Huaxiao Yang, Lucas P. Schmidt, Zhonghai Wang, Xiaoqi Yang, Yonghong Shao, Thomas K. Borg, Roger Markwald, Raymond Runyan, and Bruce Z. Gao. Dynamic Myofibrillar Remodeling in Live Cardiomyocytes under Static Stretch. *Scientific Reports*, 6(1):1–12, 2 2016.

[139] Jiang Yao, Shawn Chen, and Julius M. Guccione. A Computationally Efficient Approach to Simulate Heart Rate Effects Using a Whole Human Heart Model. *Bioengineering*, 9(8):334, 7 2022.

[140] Kyoko Yoshida and Jeffrey W. Holmes. Computational models of cardiac hypertrophy. *Progress in Biophysics and Molecular Biology*, 7 2020.

[141] Xiaoyan Zhang, Zhan Qiu Liu, Kenneth S. Campbell, and Jonathan F. Wenk. Evaluation of a novel finite element model of active contraction in the heart. *Frontiers in Physiology*, 9(APR):425, 4 2018.